AUBURN UNIVERSITY
Samuel Ginn College of Engineering

Research Report

UNMANNED AERIAL SYSTEMS FOR DETERMINING VEGETATIVE ESTABLISHMENT ON ALDOT CONSTRUCTION SITES

Submitted to

The Alabama Department of Transportation

Prepared by

Puranjit Singh
Dr. Yin Bao
Dr. Michael A. Perez
Dr. Wesley N. Donald

JUNE 2, 2025

Highway Research Center
Harbert Engineering Center
Auburn, Alabama 36849

1. Report No.	2. Government Accession No.	3. Recipient Catalog No.
4. Title and Subtitle Unmanned Aerial Systems for Determining Vegetative Establishment on ALDOT Construction Sites		5. Report Date June 2, 2025 6. Performing Organization Code
7. Author(s) P. Singh, Y. Bao, M.A. Perez, and W.N. Donald		8. Performing Organization Report No.
9. Performing Organization Name and Address Highway Research Center Department of Civil Engineering 238 Harbert Engineering Center Auburn, AL 36849		10. Work Unit No. (TRAIS) 11. Contract or Grant No.
12. Sponsoring Agency Name and Address Highway Research Center Department of Civil Engineering 238 Harbert Engineering Center Auburn, AL 36849		13. Type of Report and Period Covered Final Report 14. Sponsoring Agency Code
15. Supplementary Notes		

16. Abstract

Roadside vegetation composition assessment is essential to maintain ecological stability, control invasive species, and to ensure the adoption of environmental regulations around construction zones. Traditional monitoring methods involving visual inspections are time-consuming, labor-intensive, and not scalable. Remote sensing offers a valuable alternative in automating large-scale vegetation assessment tasks efficiently. Our study compares the performance of proximal RGB imagery processed using deep learning (DL) techniques against the Vegetation Indices (VIs) extracted at higher altitudes, establishing a foundation to use the prior in performing vegetation analysis using unmanned aerial vehicles (UAVs) for a broader scalability. A pixel-wise annotated dataset for eight roadside vegetation species was curated to evaluate the performance of multiple semantic segmentation models in this context. The best-performing MAnet DL achieved a mean intersection over union of 0.90, highlighting models' capability in composition assessment tasks. Additionally, in predicting the vegetation cover – the DL model achieved a R2 of 0.99, RMSE of 1.761 and outperformed the top VI method of SAVI which achieved a R2 of 0.49, RMSE of 23.473. The strong performance of DL models on proximal RGB imagery under-scores the potential of UAV-mounted high resolution RGB sensors for automated roadside vegetation monitoring and management tasks at construction sites. The NDVI ortho mosaic image of the Prattville construction site.

17. Key Words		18. Distribution Statement	
19. Security Classification (of this report) Unclassified	20. Security Classification (of this page) Unclassified	21. No. of Pages	22. Price None.

Research Report

UNMANNED AERIAL SYSTEMS FOR DETERMINING VEGETATIVE ESTABLISHMENT ON ALDOT CONSTRUCTION SITES

Submitted to

The Alabama Department of Transportation

Prepared by

Puranjit Singh
Dr. Yin Bao
Dr. Michael A. Perez
Dr. Wesley N. Donald

JUNE 2, 2025

DISCLAIMER

The contents of this report reflect the views of the authors who are responsible for the facts and accuracy of the data presented herein. The contents do not necessarily reflect the official views or policies of Alabama DOT, Auburn University, or the Highway Research Center. This report does not constitute a standard, specification, or regulation. Comments contained in this paper related to specific testing equipment and materials should not be considered an endorsement of any commercial product or service; no such endorsement is intended or implied.

NOT INTENDED FOR CONSTRUCTION, BIDDING, OR PERMIT PURPOSES

Puranjit Singh
Dr. Yin Bao
Dr. Michael A. Perez
Dr. Wesley N. Donald

ACKNOWLEDGEMENTS

The authors for this project would like to thank Kamand Bagherian, Spencer Overton, Preston Langston, Katherine Bandholz for supporting the project with ground data collection and data annotation process. The funding for this research was supported by the Alabama Department of Transportation project number: ALDOT 931-074.

ABSTRACT

Roadside vegetation composition assessment is essential to maintain ecological stability, control invasive species, and to ensure the adoption of environmental regulations around construction zones. Traditional monitoring methods involving visual inspections are time-consuming, labor-intensive, and not scalable. Remote sensing offers a valuable alternative in automating large-scale vegetation assessment tasks efficiently. Our study compares the performance of proximal RGB imagery processed using deep learning (DL) techniques against the Vegetation Indices (VIs) extracted at higher altitudes, establishing a foundation to use the prior in performing vegetation analysis using unmanned aerial vehicles (UAVs) for a broader scalability. A pixel-wise annotated dataset for eight roadside vegetation species was curated to evaluate the performance of multiple semantic segmentation models in this context. The best-performing MAnet DL achieved a mean intersection over union of 0.90, highlighting models' capability in composition assessment tasks. Additionally, in predicting the vegetation cover – the DL model achieved a R^2 of 0.99, *RMSE* of 1.761 and outperformed the top VI method of SAVI which achieved a R^2 of 0.49, *RMSE* of 23.473. The strong performance of DL models on proximal RGB imagery underscores the potential of UAV-mounted high resolution RGB sensors for automated roadside vegetation monitoring and management tasks at construction sites. The NDVI ortho mosaic image of the Prattville construction site.

Table of Contents

1 Chapter 1 INTRODUCTION 11
2 Chapter 2 METHODOLOGY 14
2.1 Data collection and sources 14
2.1.1 Image annotations 16
2.1.2 Image pre-processing 17
2.2 Deep learning model training 19
2.3 Vegetation Detection using Vegetation Indices-based methods 22
2.4 Summary: Key takeaways 23
2.4.1 Data Collection and Processing 23
2.4.2 DL Model Training 24
2.4.3 Vegetation Indices Methods 24
2.4.4 Evaluation Framework 24
3 Chapter 3 RESULTS 26
3.1 Deep learning model performance 26
3.2 Vegetation detection using vegetation indices methods 30
3.2.1 Vegetation detection at Prattville construction site 30
3.2.2 Vegetation detection at Tuscaloosa construction site 37
3.2.3 Vegetation detection at Linden construction site 43
3.2.4 Opelika-Stormwater research center facility 49
3.2.5 Determining optimal thresholds for vegetation detection using vegetation indices methods 54
3.3 Performance Assessment: Comparison of Vegetation Detection Using Vegetation Indices and Deep Learning Approaches 57
3.4 Summary: Key takeaways 59
3.4.1 Deep Learning Model Performance 59
3.4.2 Vegetation Indices Analysis 59
3.4.3 Comparative Performance Assessment 59
4 Chapter 4 DISCUSSION 61
4.1 Limitations 63
4.2 Future work 63
4.3 Technological Advancements Required for Effective Vegetation Identification by ALDOT 64
5 Chapter 5 CONCLUSION 66
6 REFERENCES 67

7 APPENDIX 70
A.1 Fine Tuning Annotations 70
A.2 Confusion Matrices for Deep Learning Models 72
A.3 Performance of best-performing MAnet DL model 75

LIST OF TABLES

Table 2-1: Data collection summary. 14
Table 2-2: Hyperparameters for training DL models 20-21
Table 3-1: Evaluation metric scores of DL models on validation dataset. 25
Table 3-2: Zonal statistics on selected patches at the Prattville construction site..... 32-33
Table 3-3: Zonal statistics on selected patches at the Tuscaloosa construction site.. ... 38-39
Table 3-5: Zonal statistics on selected patches at the Linden construction site. 44-45
Table 3-6: Zonal statistics on selected patches at the Opelika-Stormwater research center facility 49

LIST OF FIGURES

Figure 2-1: (Left) Mainland USA map highlighting the state of Alabama; (Right) Data collection sites in the state of Alabama 15
Figure 2-2: (Left) Skydio 2 UAV used to collect RGB images, (Center) Canon EOS Rebel SL1 DSLR camera used to collected RGB images, (Right) DJI Matrice 600 pro UAV mounted with Sentera 6x multispectral sensor used to collect images in multiple bands . 16
Figure 2-3: (Top-left) Original ground-based image and (Top-right) Ground-based image annotation in coco annotator. (Bottom-left) Original Skydio image and (Bottom-right) Skydio image an-notation in coco annotator 17
Figure 2-4: Fine-tuning annotation approach: (1) Original image, (2) Original annotation, (3) ExGI-based plant segmentation, (4) Fine-tuned annotation 18
Figure 2-5: Pixel percentage share of different grass species in the training dataset after fine-tuning the annotation masks 19
Figure 2-6: Workflow for vegetation cover analysis using multispectral imagery and vegetation indices 23
Figure 3-1: Confusion matrix for MAnet model with mit_b4 architecture backbone. 27
Figure 3-2: Prediction of trained DL models on images from testing dataset. Left to Right: (a) Original RGB image, (b) Ground truth annotation, (c) Predicted masks using trained MAnet model with mit_b4 backbone, (d) Predicted masks using trained DeepLabV3+ model with Res-Net101 backbone (e) Predicted masks using trained PSPNet model with mit_b5 backbone, (f) Predicted masks using trained Unet++ model with ResNet50 backbone..... 28
Figure 3-3: Misclassifications in composition assessment by the DL model 29
Figure 3-4: The RGB ortho mosaic image of the Prattville construction site. 30
Figure 3-5: The NDVI ortho mosaic image of the Prattville construction site 30
Figure 3-6: The NDRE ortho mosaic image of the Prattville construction site 30
Figure 3-7: The SAVI ortho mosaic image of the Prattville construction site 31
Figure 3-8: Zoomed snippet of a similar area from RGB image (above) and NDVI map (below) from Prattville construction site 32
Figure 3-9: Scatterplot for NDVI-based VI method to predict the vegetation cover at Prattville construction site 34

Figure 3-10: Scatterplot for NDRE-based VI method to predict the vegetation cover at Prattville construction site 34
Figure 3-11: Scatterplot for SAVI-based VI method to predict the vegetation cover at Prattville construction site 35
Figure 3-12: Scatterplot for Deep Learning model to predict the vegetation cover at Prattville construction site 35
Figure 3-13: The RGB ortho mosaic image of the Tuscaloosa construction site. 36
Figure 3-14: The NDVI ortho mosaic image of the Tuscaloosa construction site 37
Figure 3-15: The NDRE ortho mosaic image of the Tuscaloosa construction site. 37
Figure 3-16: The SAVI ortho mosaic image of the Tuscaloosa construction site. 38
Figure 3-17: Scatterplot for NDVI-based VI method to predict the vegetation cover at Tuscaloosa construction site 39
Figure 3-18: Scatterplot for NDRE-based VI method to predict the vegetation cover at Tuscaloosa construction site 40
Figure 3-19: Scatterplot for SAVI-based VI method to predict the vegetation cover at Tuscaloosa construction site 40
Figure 3-20 Scatterplot for Deep Learning model to predict the vegetation cover at Tuscaloosa construction sites 41
Figure 3-21: The RGB ortho mosaic image of the Linden construction site. 42
Figure 3-22: The NDVI ortho mosaic image of the Linden construction site. 43
Figure 3-23: The NDRE ortho mosaic image of the Linden construction site. 43
Figure 3-24: The SAVI ortho mosaic image of the Linden construction site. 44
Figure 3-25: Scatterplot for NDVI-based VI method to predict the vegetation cover at Linden construction site. 45
Figure 3-26: Scatterplot for NDRE-based VI method to predict the vegetation cover at Linden construction site 46
Figure 3-27: Scatterplot for SAVI-based VI method to predict the vegetation cover at Linden construction site. 46
Figure 3-28: Scatterplot for DL-based VI method to predict the vegetation cover at Linden construction site. 47
Figure 3-29: The RGB ortho mosaic image of the Opelika-Stormwater Research Center Facility. 47
Figure 3-30: The NDVI ortho mosaic image of the Opelika-Stormwater Research Center Facility 48
Figure 3-31: The NDRE ortho mosaic image of the Opelika-Stormwater Research Center Facility 48
Figure 3-32: The SAVI ortho mosaic image of the Opelika-Stormwater Research Center Facility. 48
Figure 3-33: Scatterplot for NDVI-based VI method to predict the vegetation cover at Opelika – Stormwater Research Facility 50
Figure 3-34: Scatterplot for NDRE-based VI method to predict the vegetation cover at Opelika – Stormwater Research Facility. 50
Figure 3-35: Scatterplot for SAVI-based VI method to predict the vegetation cover at Opelika – Stormwater Research Facility. 51
Figure 3-36: Scatterplot for DL-based VI method to predict the vegetation cover at Opelika – Stormwater Research Facility. 51
Figure 3-37: Scatterplot for predicted vs actual vegetation cover using best performing DL model. 52
Figure 3-38: Scatterplot for predicted vs actual vegetation cover using best performing NDVI threshold of 50% 53
Figure 3-39: Scatterplot for predicted vs actual vegetation cover using best performing NDRE threshold of 25%.. 54

Figure 3-40: Scatterplot for predicted vs actual vegetation cover using best performing SAVI threshold of 40%.... 55
Figure 3-41: (Left) B-A analysis on predicted vegetation cover using best performing VI method of SAVI against actual vegetation cover and (Right) scatterplot for predicted vegetation cover using best performing VI method vs actual vegetation cover 56
Figure 3-42: (Left) B-A analysis on predicted vegetation cover using best performing DL model against actual vegetation cover and (Right) scatterplot for predicted vegetation cover using best performing VI method vs actual vegetation cover..... 56
Figure 4-1: (Top-Left) Aerial imagery captured at Linden construction site, (Top-Right and Bottom-Left) High resolution proximal imagery of quadrats 8 laid at the site during data collection, (Bottom-Right) Classification result generated by DL model on the RGB imagery 62
Figure A-1: Pixel percentage share of different grass before (Top) and after (Bottom) fine-tuning the annotation masks. 68
Figure A-2: Confusion matrix for UNet++ model with ResNet50 architecture backbone. 69
Figure A-3: Confusion matrix for PSPNet model with mit_b5 architecture backbone 70
Figure A-4: Confusion matrix for DeepLabV3+ model with ResNet101 architecture backbone. 71
Figure A-5: Visualization of the deep learning model's performance in detecting various vegetation species along with legend showing colors used to display different vegetation specie. 72-73
Figure A-6: Visualization of the deep learning model's performance in detecting various vegetation species along with legend showing colors used to display different vegetation species. 74-75
Figure A-7: Methods to process and generate Vegetation indices-based threshold maps in QGIS. 76

Chapter 1
INTRODUCTION

Vegetation monitoring serves as a vital tool across multiple disciplines, from forest decline and carbon sequestration to climate impact assessment on plant communities [1]. Systematic observation helps detect early signs of ecological shifts, assess biodiversity fluctuations, and guide conservation efforts, particularly as human activities and climate change continue to threaten natural habitats [2]. In transportation infrastructure, monitoring roadside vegetation is essential for ensuring road safety, maintaining environmental stability, and preserving infrastructure integrity [3]. Moreover, vegetation monitoring is critical for construction site stabilization. Regulatory frameworks, such as the Construction General Permit (CGP), require that disturbed sites establish a permanent stand of vegetation at a prescribed density to prevent soil erosion and sediment runoff before project closure. Failure to meet these vegetation standards can delay permit termination, increase project costs, and jeopardize compliance with environmental regulations. Effective roadside vegetation management relies on accurate species identification, which supports strategic maintenance and targeted control efforts [4]. Managing vegetation along transportation corridors is challenging, as species introduced through construction materials, erosion control methods, or nearby land use often lack natural controls, resulting in a rapid growth [5]. The unrestrained growth can obstruct visibility, elevate fire risks, and jeopardize roadway safety, leading to increased maintenance expenses and reducing the ecological benefits of managed vegetation [6]. Furthermore, transportation corridors frequently harbor invasive plant species that tend to overwhelm and replace native vegetation. When left unmanaged, these invasive vegetation species can diminish ecosystem diversity, modify wildfire patterns through accumulated dry plant material, decay soil quality by interfering with nutrient cycling and compromising erosion protection [7]. Conventional vegetation assessment methods rely on resource-intensive field surveys involving subjective visual evaluation, requiring substantial personnel and introducing observer variability [8]. To overcome these limitations, modern approaches are needed to replace tradition-al methods with advanced techniques that offer greater speed, accuracy, and reliability.

Remote sensing has emerged as a key tool for vegetation monitoring, offering essential data on plant health, land cover changes, and ecosystem patterns [9]. The use of advanced sensors on satellites and unmanned aerial vehicles (UAV) allows for early problem detection, quantitative assessment, and species identification, enabling proactive vegetation management. These approaches assist organizations in maximizing their resource allocation, adhering to statutory requirements, and advancing ecological objectives [10]. Advancements and improvements in in spatial, spectral, and temporal resolution have boosted the ability to monitor

plant growth patterns for multiple practical purposes [11]. Low-altitude drone imagery provides high-resolution data for detailed local monitoring, avoiding problems like cloud cover that affect satellites, while satellite imagery remains valuable for regional and global vegetation tracking [12, 13]. With the availability of advanced digital sensors capable of capturing high-resolution spectral and spatial information, new opportunities have emerged for tackling complex tasks such as detailed vegetation detection and classification. However, a research gap remains in systematically evaluating whether high-resolution imagery can effectively perform vegetation composition analysis.

Multispectral imaging plays a pivotal role in vegetation monitoring by capturing reflectance across various spectral bands, including near infrared (NIR), red, green, blue, and red-edge. This enables the generation of vegetation indices (VIs) to assess plant health, chlorophyll content, and vegetation density, supporting applications such as species detection, land cover classification, and precision agriculture [14]. [15] used multispectral data to distinguish shrubs and grasses in desert areas, applying ML models like SVM and maximum likelihood. [16] introduced the squared Red-Blue NDVI to improve vegetation detection in urban settings and reduce misclassification from non-vegetative surfaces. [17] evaluated UAVs for turfgrass monitoring using image processing and ML techniques, proposing a green pixel detection method based on HSV color space. [18] compared classification algorithms to estimate green vegetation cover in Mongolian grasslands, high-lighting vegetation variability over time. While multispectral imagery has been widely applied in areas such as crop health monitoring, weed detection, irrigation management, nutrient deficiency identification, and yield estimation, it often faces limitations in accurately distinguishing between vegetation species that exhibit similar spectral reflectance characteristics.

Deep learning (DL) has emerged as a powerful tool in vegetation detection, enabling accurate classification, segmentation, and analysis of plant species, crop health, and vegetation cover [19]. [20] combined drone and satellite imagery to generate a high-resolution grassland canopy cover map across China, addressing challenges of limited field data and scale mismatches. DL models such as CNNs, RNNs, and transformers have been widely applied to vegetation mapping by learning complex spatial and spectral patterns from high-resolution imagery [21]. [22] applied watershed segmentation to estimate clover-grass cover, aiding in nitrogen and feed management. In agriculture, DL supports tasks like crop yield prediction, disease detection, weed identification, and irrigation management [23]. [24] developed a grid cell-based approach for weed detection and localization to support precision herbicide applications. Semantic segmentation (SS) models, which classify each pixel in an image, are especially effective for species-level vegetation detection due to their fine-grained output. These models often use encoder-decoder architectures to reconstruct high-resolution predictions from compressed representations [25]. [8] evaluated thirty DL model combinations to estimate clover-

grass ratios for dairy feed optimization. [1] used NIR and RGB data to train the DeepLabV3+ model for vegetation detection. [26] introduced AerialSegNet, an improved SegNet-based model that out-performed existing SS models. [27] showed multispectral UAV imagery outperformed RGB for classifying vegetation, bare soil, and dead matter in landslide areas. [28] reported that UAVs often underestimated vegetation cover in post-burn Mediterranean shrublands, especially in areas with high species richness.

While current remote sensing and DL techniques have shown promise in vegetation detection and mapping, several gaps remain that warrant further investigation. Most existing studies have concentrated on binary classification [29, 30, 31] or the detection of a limited number of vegetation classes [8, 24, 32], leaving the field of multi-class vegetation detection, particularly involving diverse roadside grass species—relatively underexplored. Accurately detecting and monitoring non-native, fast-spreading grasses is essential for ecosystem management and biodiversity conservation, yet remains a complex challenge. This study aims to bridge these gaps by developing and evaluating SS models designed specifically for roadside vegetation composition assessment. The research objectives include curating an annotated proximal RGB image dataset representing diverse vegetation species, training and comparing multiple DL-based SS models for species-wise classification, and comparing their performance against VI-based methods in terms of prediction accuracy and generalizability. The outcomes of this research will enhance our under-standing of vegetation dynamics, support targeted ecological interventions, and contribute to sustainable roadside management strategies.

Chapter 2
METHODOLOGY

2.1 DATA COLLECTION AND SOURCES

To develop a comprehensive vegetation analysis framework, a diverse dataset was curated through systematic data collection across multiple construction sites in Alabama between July 2022 and 2023. Our multi-tiered approach employed standardized 0.6 m × 0.6 m PVC frames as reference quadrats, strategically positioned throughout the sites to ensure consistent sampling areas. These frames served as fixed boundaries for vegetation assessment and provided reference areas for both aerial and ground-based imagery. The data collection strategy incorporated multiple sensing platforms for collecting proximal RGB images included in our dataset. Skydio 2 (Skydio, San Mateo, California, USA), equipped with a 12.3 MP camera capable of capturing 4,056 × 3,040-pixel images, was used for low-altitude flights at approximately 1.83 m above ground level (AGL). In addition, a DSLR camera (Canon EOS Rebel SL1 DSLR, Canon, Tokyo, Japan), with an 18.5 MP sensor producing images at 5,288 × 3,506 pixels, was used at a similar altitude for ground-based RGB image collection. The ground sampling distance (GSD) of Skydio drone and DSLR camera was 0.0138 cm/pixel and 0.0139 cm/pixel, respectively. This close-range proximal imagery was instrumental in training DL models for vegetation detection and composition assessment, providing detailed visuals necessary to differentiate between multiple roadside vegetation species. A total of 18 UAV flights, along with ground-based data collection were conducted over a 13-month period during the data collection phase. The dataset comprises eight different roadside grass species, which were collected during data collection across several construction sites in Alabama. The dataset covers eight grass species including Annual ryegrass (Lolium multiflorum), Bahia (Paspalam notatum), Bermuda (Cynodon dactylon), Crabgrass (Digitaria sanguinalis), Browntop millet (Urochloa ramosa), Lespedeza (Lespedeza striata), Johnson grass (Sorghum halepense), and Fescue (Festuca arundinacea). Table 2-1 and Figure 2-1 provide a com-prehensive overview of the UAV flight operations and the specific site locations where data was collected.

Table 2-1: Data collection summary.

Location	Date	Vegetation species	Image acquisition: Images collected
Lee county: Auburn	03/10/2023	Annual ryegrass	Skydio: 10
	03/16/2023	Annual ryegrass and Lespedeza	Skydio: 39
	03/23/2023	Annual ryegrass, Bermuda, Lespedeza	Canon: 25
	07/08/2022	Bermuda, Crabgrass, Johnson grass, Lespedeza	Canon: 38. Skydio: 40

Lee county: Opelika	07/15/2022	Bermuda, Browntop millet, Crabgrass, Johnson grass, Lespedeza	Canon: 40. Skydio: 40
	07/22/2022	Bahia, Bermuda, Browntop millet, Crabgrass, Johnson grass, Lespedeza	Canon: 40. Skydio: 39
	07/29/2022	Bahia, Bermuda, Browntop millet, Lespedeza	Canon: 15
	08/03/2022	Browntop millet, Crabgrass, Johnson grass, Lespedeza	Canon: 40, Skydio: 33
	08/11/2022	Browntop millet, Crabgrass, Johnson grass, Lespedeza	Canon: 40
	08/18/2022	Browntop millet, Crabgrass, Johnson grass, Lespedeza	Skydio: 42
	09/02/2022	Crabgrass, Lespedeza	Skydio: 30
	05/26/2023	Bermuda	Canon: 10
	06/02/2023	Bermuda	Canon: 20
	07/18/2023	Bahia, Lespedeza	Canon: 20
Linden	07/28/2023	Bahia, Browntop millet, Crabgrass Johnson grass, Lespedeza	Canon: 16
Montgomery	06/09/2023	Annual ryegrass, Johnson grass, Lespedeza	Canon: 20
Prattville	07/27/2023	Bermuda, Crabgrass, Johnson grass, Lespedeza	Canon: 20
Tuscaloosa	07/28/2023	Crabgrass, Lespedeza	Canon: 18

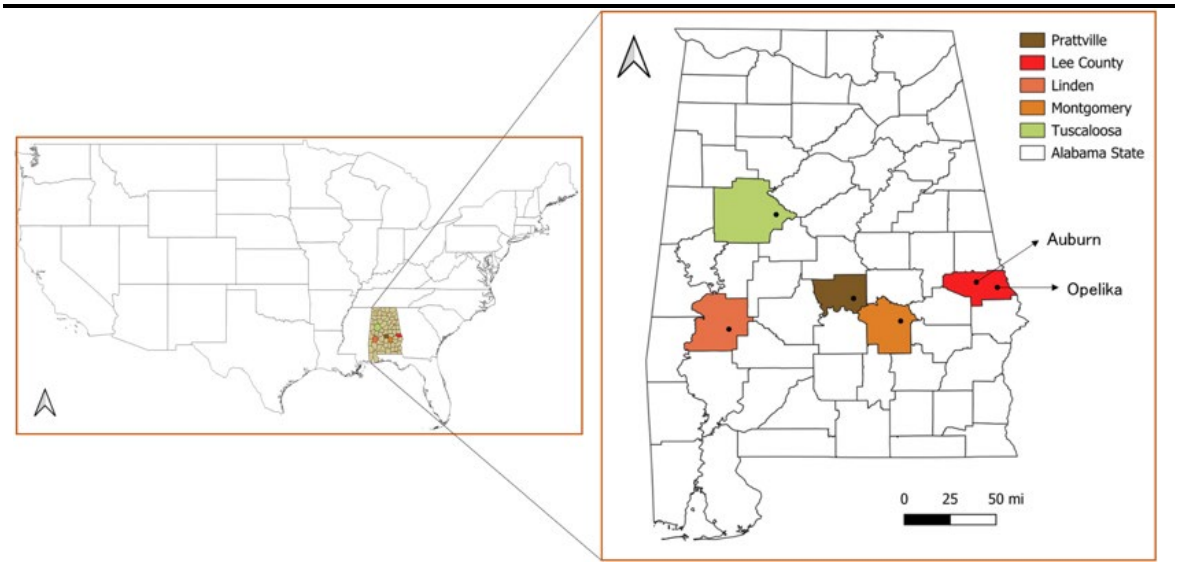

Figure 2-1. (Left) Mainland USA map highlighting the state of Alabama; (Right) Data collection sites in the state of Alabama.

In addition, multispectral data was collected using a DJI Matrice 600 pro (DJI Technology Inc., Shenzhen, China) UAV equipped with a Sentera 6X sensor (Sentera, St. Paul, Minnesota, USA), which was flown at an altitude of 30 meters AGL. The multispectral sensor collected imagery across six different bands of Red, Green, Blue, Near-Infrared (NIR), Red Edge, and RGB respectively. This information was utilized to evaluate the effectiveness of individual spectral bands for determining vegetation cover density by deriving various VIs. The multispectral bands, excluding the RGB channel, had a spatial resolution of 3.2 MP, generating images with dimensions of 2,048 × 1,536 pixels and a GSD of 1.3 cm/pixel. Figure 2-2 presents images of the different cameras and drones used for data collection. To analyze vegetation cover using

multispectral data, several UAV flights were conducted at multiple construction sites in Alabama, including Prattville, Tuscaloosa, Linden, and Opelika-Stormwater research center facility.

Figure 2-2: (Left) Skydio 2 UAV used to collect RGB images, (Center) Canon EOS Rebel SL1 DSLR camera used to collected RGB images, (Right) DJI Matrice 600 pro UAV mounted with Sentera 6x multispectral sensor used to collect images in multiple bands.

2.1.1 Image annotations

The SS-based DL models were trained using the RGB images alone. Training these models requires a pixel-wise annotated dataset where each and every pixel is labeled to represent a specific class category. All the RGB images in the dataset were annotated using the 'COCO Annotator' tool [33] which provides a straightforward interface for creating de-tailed, pixel-level annotations. A '. json' file was generated after completing the annotations, containing the metadata needed to link each pixel to a specific vegetation class. Image annotation was restricted to vegetation species located within the established PVC frame boundaries, for focused data annotation and analysis. These predefined sampling areas created a structured framework for assessing DL model accuracy in vegetation species identification and classification. The frame-based annotation strategy ensured precise evaluation of model performance within clearly defined spatial boundaries.

During the annotation process, it was observed that a significant portion of the im-ages contained areas outside the region of interest or PVC frame boundaries as shown in Figure 2-3. To ensure optimal model training, a python script was employed to extract only the regions within the frame from both the original images and the corresponding annotated masks. This process resulted in a refined dataset of 635 images, each focused solely on the relevant frame area. Isolating the frame areas also led to a reduction in image dimensions, with ground-based images reducing to 3,072 × 2,560 pixels and Skydio UAV images reduced to 768 × 768 pixels respectively. All 635 original images were divided into smaller 256 × 256-pixel tiles, which were

subsequently utilized for SS-based DL model training. Following this tiling process, the final training dataset comprised of 44,793 images.

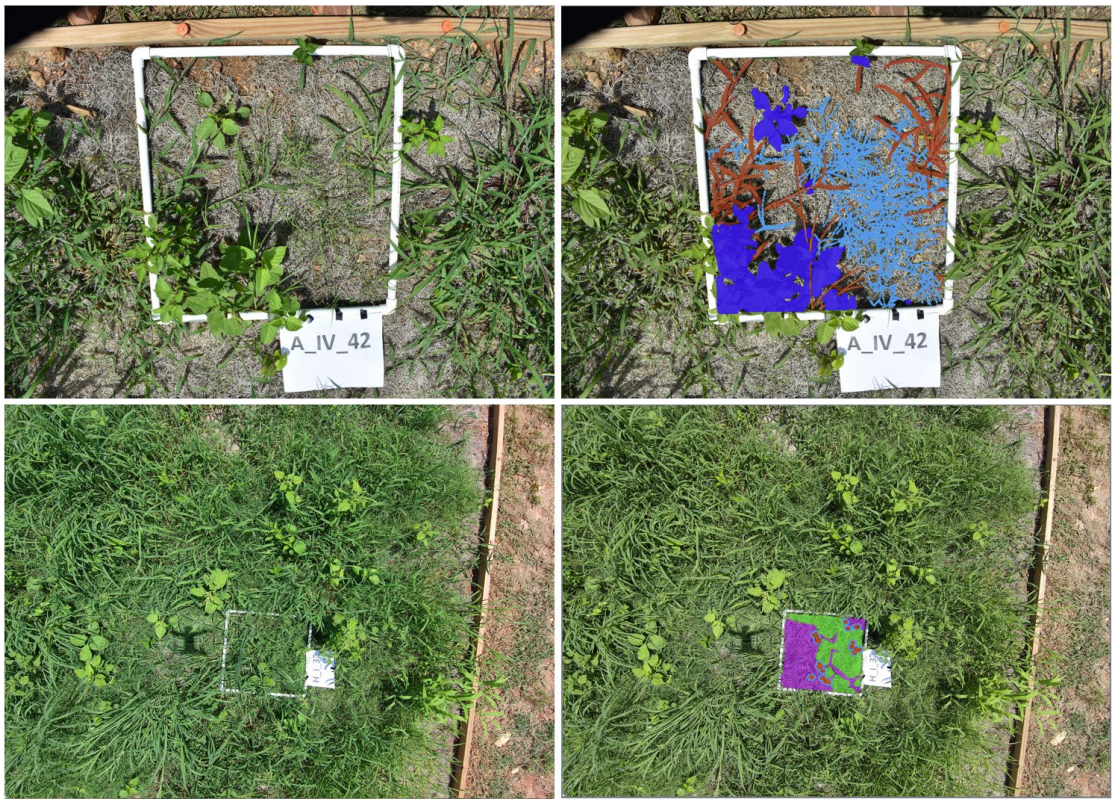

Figure 2-3: (Top-left) Original ground-based image and (Top-right) Ground-based image annotation in coco annotator. (Bottom-left) Original Skydio image and (Bottom-right) Skydio image an-notation in coco annotator.

2.1.2 Image pre-processing

Following the reduction of image dimensions and the extraction of frame regions, it was observed that the annotations lacked precision, with numerous background pixels mistakenly labeled as vegetation species. Accurate and high-quality annotations are essential for training effective SS models, as they enable the model to learn meaningful features and enhance classification accuracy during evaluation. Conversely, poor annotation quality can severely hinder model performance and compromise its ability to generalize well to unseen datasets. To address this issue, a strategy was implemented to refine the annotations. The refinement strategy involved a two-step approach – The OpenCV library [34] was used to isolate the green pixels from the original image, and the green-pixel im-age was then compared with the original annotated mask, and any pixels that were not identified as green but were labeled as a vegetation class were reclassified as background class. This adjustment resulted in cleaner and more accurate

annotations, focusing solely on true vegetation pixels. As shown in Figure 2-4, this refinement process helped to improve annotation quality, resulting in fine-tuned annotations that were better suited for training the DL models.

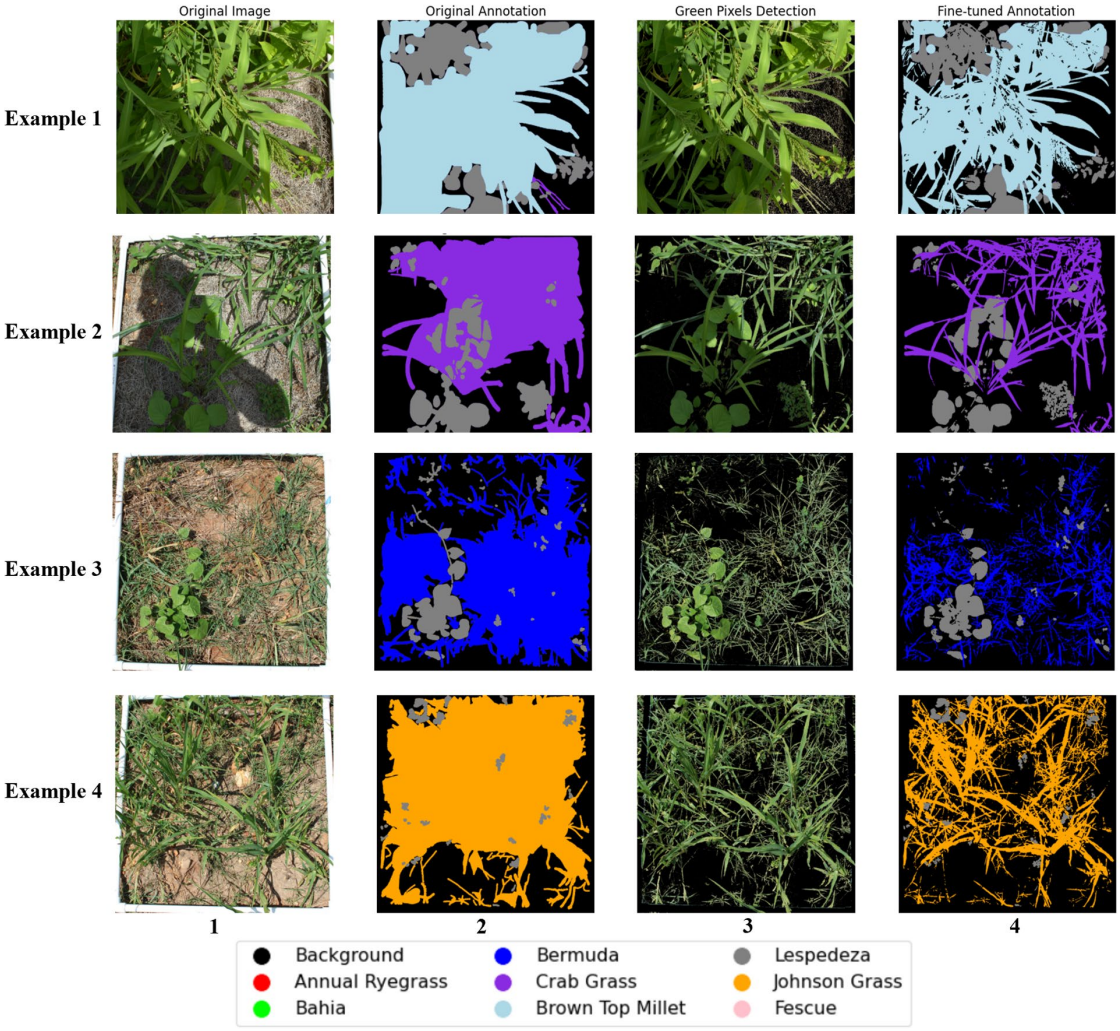

Figure 2-4: Fine-tuning annotation approach: (1) Original image, (2) Original annotation, (3) ExGI-based plant segmentation, (4) Fine-tuned annotation.

The pie chart in Figure 2-5 Illustrates the pixel percentage distribution of various grass species used for training the SS-based DL model. The majority of the dataset consists of background pixels, accounting for 59% of the total, followed by Bermuda grass at 10%. Other grass species, including Johnson grass (7%), Browntop millet (7%), Lespedeza (5%), Crabgrass (5%), and Fescue (2%), are represented in smaller proportions. Annual ryegrass and Bahia have the smallest shares, contributing 4% and 1%, respectively. This distribution reflects the diverse composition of the dataset and highlights the class imbalance that the model needs to address during training. The pie charts depicting pixel percentage share before and after fine tuning the annotations are presented and discussed with details in section Appendix A.1. of the appendix.

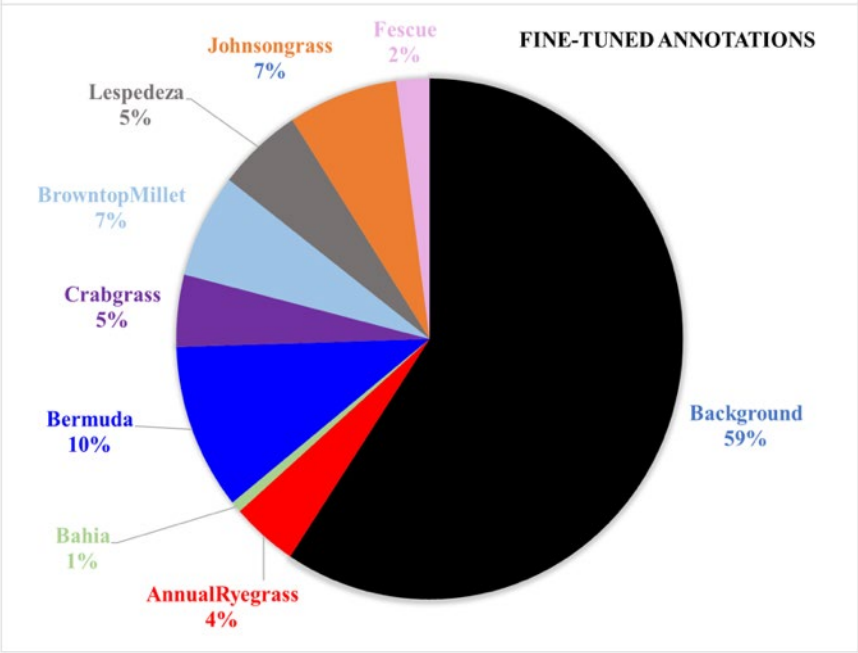

Figure 2-5. Pixel percentage share of different grass species in the training dataset after fine-tuning the annotation masks.

The DL model was trained on an annotated dataset of 44,793 images, each sized 256 × 256 pixels. The dataset was split into three parts: training, validation, and testing sets, with a ratio of 70%, 15%, and 15%, respectively. This division resulted in 31,357 images for training, 6,718 images for validation, and testing datasets. The training set was used to optimize the model's parameters, while the validation set provided feedback on model performance during training, helping to prevent overfitting. The testing set, containing unseen data, was reserved for final evaluation to assess the model's ability to generalize to new images. This structured data division enabled a robust evaluation framework, ensuring that the model's performance could be accurately measured.

2.2 DEEP LEARNING MODEL TRAINING

In this study, the encoder-decoder based SS models of UNet++, PSPnet, MAnet, and DeepLabV3+ to perform the task of vegetation detection and check their performance in performing composition assessments.

The U-Net++ model enhances the original U-Net architecture by introducing nested and dense skip connections, which improve segmentation accuracy by refining feature maps at multiple scales [35]. This architecture is particularly effective for tasks requiring precise boundary delineation, such as medical and vegetation segmentation. PSPNet uses pyramid pooling to capture global and local contextual information, which helps improve segmentation accuracy in complex scenes. It is widely used in applications that benefit from understanding spatial

hierarchies, such as urban and natural landscape segmentation [36]. MAnet integrates multi-scale attention mechanisms with U-Net, enabling the model to focus on different parts of the image at varying scales. This improves its ability to detect fine details and capture spatial context, making it suitable for tasks with intricate object boundaries [37]. DeepLabv3+ combines atrous spatial pyramid pooling with a de-coder module, allowing it to capture contextual information while preserving high spatial resolution. It has been successfully applied in tasks requiring both fine detail and global context, such as satellite and vegetation segmentation [38].

As illustrated in Figure 2-5, the original dataset exhibited substantial class imbalance in pixel distribution across different vegetation species. The initial distribution showed Background (34%), Johnson grass (16%), and Browntop Millet (15%) as dominant classes, while several important grass species such as Bermuda grass (3%), Bahia (3%), and Fes-cue (2%) were significantly under-represented. This imbalance posed a critical challenge for model training, potentially biasing the model towards majority classes and compromising its ability to accurately detect and classify minority species. Also, after fine-tuning the annotations a higher-class imbalance issue still exists where the underrepresented grass categories of Bahia and Fescue had only 1%- and 2%-pixel percentage share in the dataset used for training. To overcome this class imbalance challenge, focal loss function was implemented during model training. Focal loss, introduced by [39], effectively handles class imbalance by dynamically adjusting the weight of each class based on classification difficulty. This loss function reduces the relative loss contribution from well-classified examples and focuses training on hard-to-classify cases, particularly benefiting the under-represented grass species. The adaptive nature of focal loss helps prevent the model from being dominated by prevalent classes while maintaining learning efficiency for minority classes.

Model training was conducted on a laptop Dell Precision 5680 laptop (Dell, Round Rock, Texas, USA) running Windows 11 Enterprise (Windows, Redmond, California, USA). The system specifications included an Intel Core i9-12900H processor, 32 GB LPDDR5 RAM, 1 TB NVMe SSD storage, and an Nvidia GeForce RTX 4090 GPU with 16 GB GDDR6 memory. The SS models utilized various architecture backbones implemented through ‘PyTorch’, optimized with Nvidia CUDA 11.8 and OpenCV 4.8.0 for GPU-accelerated training. The dataset consisted of 44,793 images, each sized at 256 × 256 pixels. The specific hyperparameters employed for each model variant are detailed in Table 2-2.

Table 2-2: Hyperparameters for training DL models.

Hyperparameters	Values
Optimizer	Adam
Learning rate	2e-4
Loss function	Focal loss (γ = 3.0)

Learning rate scheduler	CosineAnnealingLR
Epochs	50
Augmentations	Random Crop, Horizontal/Vertical flip, ShiftScaleRotate
Batch size	32
Image size	256 × 256
Evaluation metrics	Loss, Precision, Recall, IoU
Weight initialization	Fine-tuning pretrained weights on Imagenet
Architecture backbones used	mit_b5, mit_b4, ResNet101, ResNet50, Xception
Dropout rate	0.2

The SS models were evaluated using three fundamental metrics: Precision, Recall, and intersection over union (IoU) on the validation datasets during training. Precision quantifies prediction accuracy by measuring the ratio of correct positive predictions to total positive predictions, while Recall assesses detection completeness by calculating the proportion of actual positive cases correctly identified. The IoU score, calculated as the intersection area divided by the union area between predicted and ground truth segmentation masks, serves as the primary evaluation metric for SS tasks. IoU significance stems from its ability to simultaneously assess both localization accuracy and segmentation quality, making it particularly valuable for pixel-wise classification tasks. Mathematically, these metrics can be represented as follows:

$$Precision = \frac{TP}{TP\ +\ FP}, \tag{1}$$

$$Recall = \frac{TP}{TP\ +\ FN}, \tag{2}$$

$$IOU = \frac{TP}{TP\ +FN\ +\ FP} \tag{3}$$

where TP refers to True Positive, FP refers to False Positive, FN refers to False Negative, TN refers to True Negative. These equations provide quantitative measures of the DL model's performance in terms of accuracy in SS tasks.

The trained DL model's generalization capability was evaluated on an independent test set of 6,615 sub-images, with performance assessed through IoU-based confusion matrices. This confusion matrix provided a detailed view of the model’s accuracy in pixel-wise classification across different classes, offering insights into its effectiveness in handling new images. The confusion matrix plays a crucial role in assessing the trained model’s ability to understand and accurately classify each pixel, allowing for a judgment of the model’s pixel-wise performance after training. This evaluation helps identify how well the model has learned to distinguish between various classes at a granular level. Additionally, the model's accuracy in predicting vegetation

cover was assessed by comparing the predicted percentage of vegetation cover in the masks with the actual vegetation cover in the annotated masks. This comparison involved calculating the percentage of pixels predicted as foreground (vegetation) in the test images versus the actual foreground pixels in the annotations. This method provided a direct assessment of the model's capability to accurately estimate vegetation cover, which is essential for applications in environmental monitoring and vegetation analysis.

2.3 VEGETATION DETECTION USING VEGETATION INDICES-BASED METHODS

The NIR band was particularly valuable, as it provides insights into chlorophyll content, a key indicator of plant health and vitality. The multispectral data enabled the generation of several VI, which are crucial for accurately estimating vegetation cover in the study areas.

Three different VIs were derived and explored in this research work: Normalized difference vegetation index (NDVI) is a widely used indicator that leverages the NIR and red bands to estimate vegetation health and chlorophyll content, making it suitable for general vegetation density assessment. Normalized difference red edge (NDRE) index utilizes the red-edge band instead of the red band, offering increased sensitivity to chlorophyll con-centration and better performance in areas with dense or mature vegetation, and soil adjusted vegetation index (SAVI) incorporates a soil brightness correction factor, which makes it more effective in areas with sparse vegetation or exposed soil, by reducing the in-fluence of background soil reflectance. Each of these indices offers unique advantages for vegetation analysis:

$$NDVI = \frac{NIR - RED}{NIR + RED}, \tag{4}$$

$$NDRE = \frac{NIR - RedEdge}{NIR + RedEdge}, \tag{5}$$

$$SAVI = \frac{(NIR - RED) \times (1 + L)}{(NIR + RED + L)}, L = 0.25 \tag{6}$$

Steps followed to processing multispectral Images for the task of vegetation detection as depicted in Figure 2-6. The raw multispectral images were first calibrated to ensure ac-curate reflectance values, and then orthomosaics were generated for the key spectral bands using Agisoft software (Agisoft Metashape ProfessionalTM, St. Petersburg, Russia). Next, VIs such as NDVI, NDRE, and SAVI were calculated for each orthomosaic using the ‘Raster Calculator’ feature in QGIS (QGIS Desktop 3.40.3, QGIS Documentation tool, 2024). The orthomosaics were then imported into QGIS, where the frames placed during data collection were segmented, allowing for focused analysis within the designated boundaries. To determine vegetation cover within the frames, various thresholds were applied to the generated VI, with NDVI thresholds ranging from 25% to 60%, NDRE from 20% to 45%, and SAVI from 20% to 55%. Finally, the

zonal statistics tool in QGIS was used to calculate the mean statistic for each frame, enabling an accurate assessment of vegetation density and cover at a granular level. This methodical approach to vegetation analysis, utilizing multispectral data and Vis, enabled precise detection and assessment of vegetation cover, facilitating better understanding and management of vegetation at the study sites.

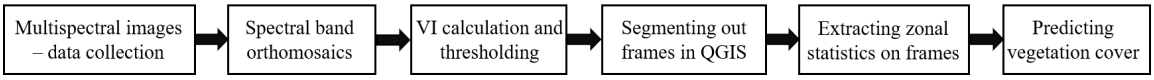

Figure 2-6: Workflow for vegetation cover analysis using multispectral imagery and vegetation indices.

The evaluation framework for comparing VI-based approaches and the optimal DL model incorporated multiple quantitative metrics on the test dataset: mean absolute error (*MAE*), root mean squared error (*RMSE*), mean absolute percentage error (*MAPE*), and co-efficient of determination (R^2). Statistical validation of the prediction accuracy utilized bland-altman (B-A) analysis [40] to assess agreement between predicted and actual vegetation coverage values. The B-A methodology quantifies prediction reliability through two key parameters: bias (mean difference between actual and predicted values) and limits of agreement (LoA, defined as bias ± 1.96 standard deviations). This analysis provides critical insights into model performance, where minimal bias and narrow LoA ranges indicate strong predictive accuracy. The B-A plots offer visual representation of measurement differences against means, facilitating identification of systematic biases and agreement boundaries essential for model validation. The *MAE*, *RMSE*, *MAPE*, and R^2 were evaluated using the following equations:

$$MAE = \frac{1}{N}\left(\sum_{i=0}^{N-1} y_i - y_i^{pred}\right), \tag{7}$$

$$RMSE = \sqrt{\frac{1}{N}\sum_{i=0}^{N-1}\left(y_i - y_i^{pred}\right)^2}, \tag{8}$$

$$MAPE = \frac{1}{N}\left(\sum_{i=0}^{N-1}\frac{\left|y_i - y_i^{pred}\right|}{y_i} \times 100\right), \tag{9}$$

$$R^2 = 1 - \frac{\sum_{i=0}^{N-1}\left(y_i - y_i^{pred}\right)^2}{\sum_{i=0}^{N-1}(y_i - y_{mean})^2} \tag{10}$$

2.4 SUMMARY: KEY TAKEAWAYS

2.4.1 Data Collection and Processing

- A comprehensive vegetation dataset was collected across multiple Alabama construction sites over 13 months, using standardized 0.6m × 0.6m PVC frames for consistent testing.

- Multiple imaging platforms were employed: a Skydio 2 drone, a Canon DSLR were used to collect proximal RGB imagery, and a DJI Matrice 600 with Sentera 6X multispectral sensor was used to collect imagery in different spectral bands of Red, Green, Blue, NIR, RedEdge, and RGB.
- The dataset captured eight roadside grass species (Annual ryegrass, Bahia, Bermuda, Crabgrass, Browntop millet, Lespedeza, Johnson grass, and Fescue).
- Images were annotated using COCO Annotator tool, with regions of interest extracted from original images and divided into 256 × 256-pixel tiles, yielding 44,793 training images.
- Annotation quality was improved through a two-step refinement process that isolated green pixels and removed non-vegetation pixels incorrectly labeled as vegetation.

2.4.2 DL Model Training

- Four SS models were evaluated: UNet++, PSPnet, MAnet, and DeepLabV3+, with various architecture backbones.
- Focal loss function was implemented to address significance class imbalance in the dataset.
- Models were evaluated using Precision, Recall, and IoU evaluation metrics on the validation datasets.

2.4.3 Vegetation Indices Methods

Multiple vegetation indices were derived from multispectral data: NDVI (NIR and red bands), NDRE (NIR and red-edge bands), and SAVI (NIR, red bands with soil adjustment). Orthomosaics were generated for each spectral band and indices were calculated using QGIS. Multiple thresholds were tested for each vegetation index to determine optimal values for vegetation detection.

2.4.4 Evaluation Framework

- Model performance was assessed through comprehensive statistical analysis: Mean Absolute Error (MAE), Root Mean Squared Error (RMSE), Mean Absolute Percentage Error (MAPE), and Coefficient of Determination (R^2).
- Bland-Altman analysis was employed to assess agreement between predicted and actual vegetation coverage values.

Importance: The methodological approach demonstrates a systematic integration of drone-based imagery, advanced DL techniques, and conventional Vi-based methods. The data collection strategy and annotation refinement process highlight the importance of high-quality training data for effective model performance. The combination of multiple evaluation metrics provides a

comprehensive assessment framework essential for validating model reliability in practical applications.

Chapter 3
RESULTS

3.1 DEEP LEARNING MODEL PERFORMANCE

The performance evaluation of different SS models revealed varying capabilities in vegetation detection tasks. Four distinct architectures were assessed: UNet++, PSPnet, DeepLabV3+, and MAnet, each utilizing different backbone networks in their encoder sections. The evaluation metric scores for various DL models evaluated on the validation dataset, are summarized in Table 3-1. Each model was assessed based on key metrics: loss, precision, recall, and IoU score. These metrics collectively provide insights into the models' accuracy, reliability, and ability to generalize to new data.

Table 3-1: Evaluation metric scores of DL models on validation dataset.

DL model	Encoder section	val_loss	val_precision	val_recall	val_iou score	Trainable parameters
UNet++	ResNet50	0.074	0.851	0.859	0.825	48.98 M
PSPnet	mit_b5	0.069	0.874	0.879	0.836	81.63 M
DeepLabV3+	ResNet101	0.066	0.894	0.896	0.844	45.67 M
MAnet	mit_b4	0.066	0.901	0.906	0.869	54.84 M

The encoder section of each model plays a crucial role in feature extraction. It utilizes different backbone architectures to capture intricate details from input images, significantly influencing the model's overall performance. The MAnet model, which utilized the mit_b4 (Mix Vision Transformer) architecture as its encoder backbone, achieved the best results on the validation dataset. MiT are well-suited for handling complex image seg-mentation tasks, as they leverage transformer blocks to capture long-range dependencies and richer contextual information across the image. The MAnet model's mix vision transformer backbone allowed it to excel in terms of precision (0.681), recall (0.737), and IoU score (0.791), showcasing its effectiveness in accurately segmenting vegetation classes. The PSPNet model with a mit_b5 backbone also performed well, yielding a high IoU score of 0.751 and maintaining good precision and recall values. The Mix Vision Transformer architecture in PSPNet further enhanced its ability to capture spatial hierarchies and con-text within the images, although it was slightly outperformed by MAnet in this study. The DeepLabV3+ model, equipped with a ResNet101 backbone, achieved an IoU score of 0.779. ResNet101, known for its deep residual layers, aids in

capturing complex patterns, but it may not be as adept as transformer-based architectures for capturing long-range dependencies in dense segmentation tasks. Lastly, the Unet++ model with a ResNet50 backbone performed adequately but had the lowest IoU score (0.688) among the models tested. While ResNet50 is efficient and can handle segmentation tasks reasonably well, its shallower depth compared to ResNet101 and its lack of transformer-based components may have limited its performance in this specific application.

The transformer-based backbones (mit_b4 and mit_b5) demonstrated better performance in segmentation tasks, particularly with the MAnet model, which achieved the highest accuracy and segmentation quality on the validation dataset. These results high-light the potential of transformer-based architectures in enhancing the performance of SS models in applications involving vegetation detection and classification. Following the validation phase, DL model testing was undertaken to evaluate the real-world applicability and generalization capabilities of the models. Confusion matrices for all the trained DL models were generated on the testing dataset to provide a thorough comparison in per-forming the classification accuracy.

The Unet++ model (Figure A2 in Supplementary Material) with a ResNet50 backbone achieves a mean IoU score of 0.771 for pixel-wise vegetation classification. High true positive rates are observed for Crabgrass (0.83) and Lespedeza (0.80), reflecting strong performance in these classes. The background class also shows good accuracy (0.89), demonstrating its ability to separate vegetation from non-vegetation. However, lower accuracy for Browntop millet (0.70) suggests challenges in distinguishing similar classes. The PSPNet model (Figure A3 in Supplementary Material) with the mit_b5 backbone achieves a mean IoU of 0.878, with high true positive rates for Bermuda (0.96) and Annual ryegrass (0.93). The background class also performs well (0.95), ensuring accurate separation of vegetation from non-vegetation areas. However, lower accuracy in classes like Lespedeza (0.85) and Crabgrass (0.75) indicates some misclassification. The DeepLabv3+ model (Figure A4 in Supplementary Material) with a ResNet101 backbone achieves a mean IoU of 0.894, with strong performance for Bermuda (0.96) and Bahia (0.94). The background class also scores highly (0.95), reinforcing its ability to distinguish vegetation. However, slightly lower accuracy in Crabgrass (0.75) and Johnson grass (0.87) indicates areas for improvement. Overall, the model shows reliable generalization across most vegetation classes.

The confusion matrix for the MAnet model (Figure 3-1) with the mit_b4 backbone demonstrates high accuracy in pixel-wise classification across various vegetation classes achieving a mean IoU score of 0.900. Figure 3-1 displays a column-normalized confusion matrix, enabling visualization of precision percentages across each class classification category. This model shows strong performance, with notable true positive rates for Annual ryegrass (0.97) and Bahia (0.96), indicating effective detection and classification of these categories. The background class also achieved a high ac-curacy of 0.96, essential for distinguishing vegetation from non-

vegetation areas. Classes like Bermuda (0.95) and Browntop millet (0.90) also show high accuracy, reflecting the model's robustness in handling diverse vegetation types. However, there are some minor misclassifications for classes like Lespedeza (0.84) and Crabgrass (0.75), where slight overlaps in classification are observed.

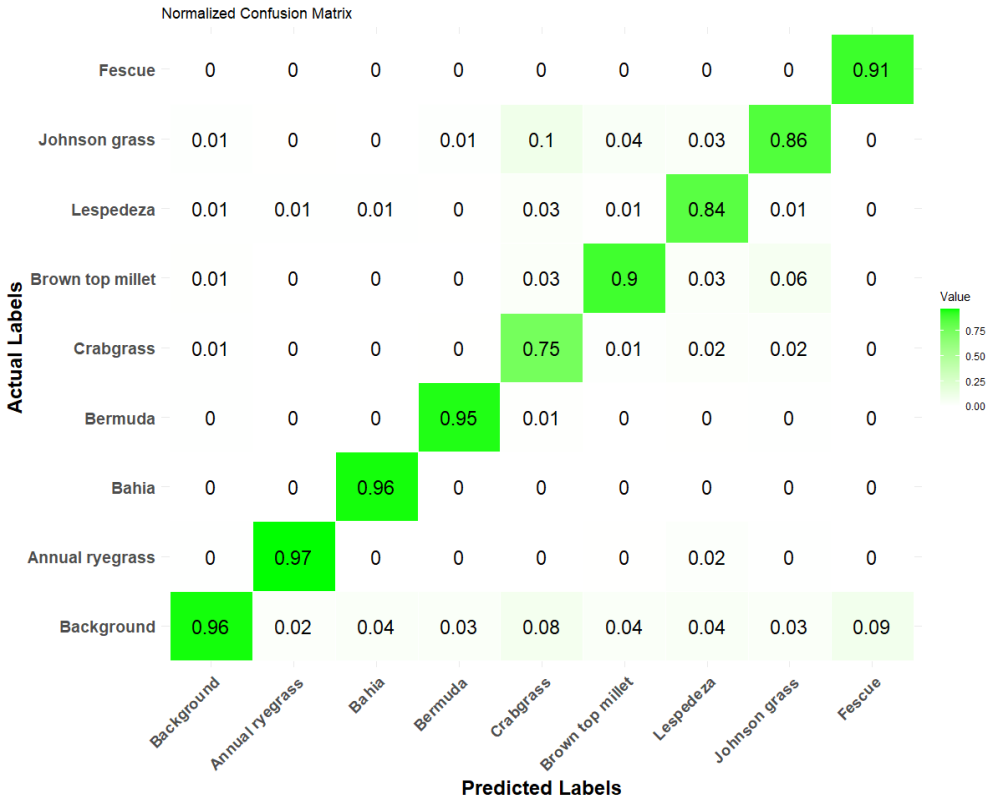

Figure 3-1: Confusion matrix for MAnet model with mit_b4 architecture backbone.

This model achieved the highest overall IoU score among all models tested, with a mean IoU of 0.90 along the diagonal values of the confusion matrix, confirming the best performance in accurately identifying each vegetation class on the testing dataset amongst other SS models explored in this study. This high IoU score indicates that the MAnet model with the mit_b4 backbone generalizes well and is particularly effective for this multi-class SS task.

Figure 3-2. presents a visual comparison of the predictions made by different DL models on a set of test images, highlighting their performance in vegetation classification. Among the models, the MAnet model with mit_b4 backbone demonstrates better predictions, particularly in capturing fine details and distinguishing between different vegetation classes. This is evident in its ability to accurately segment smaller patches and com-plex boundaries in mixed vegetation areas, compared to the other models.

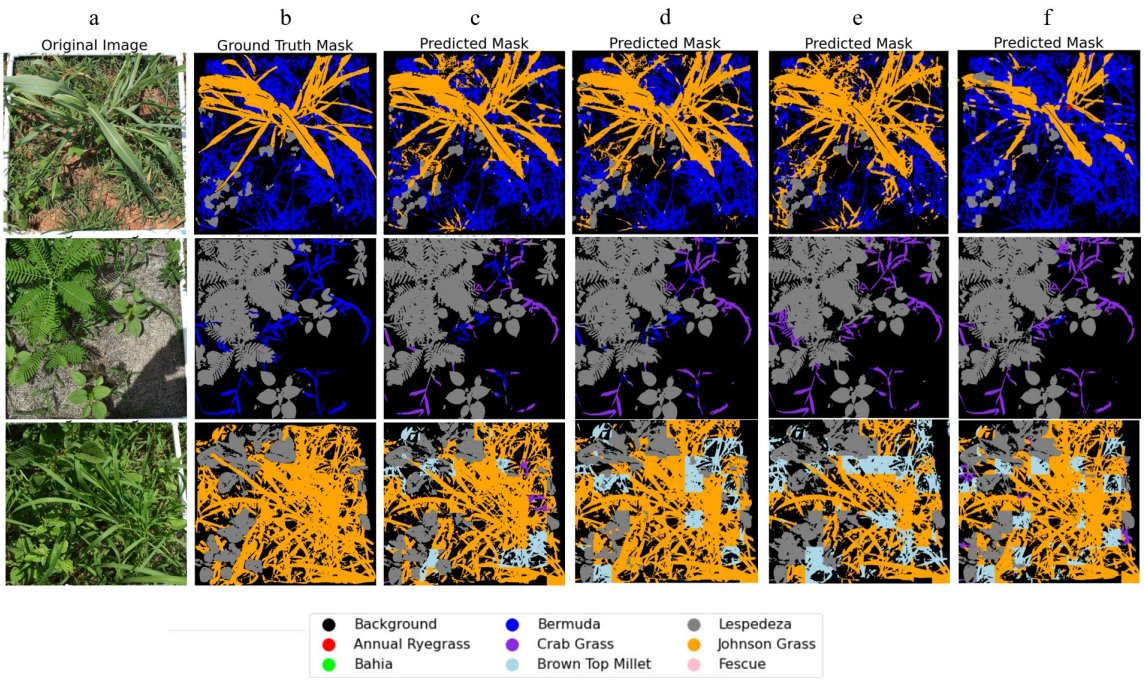

Figure 3-2: Prediction of trained DL models on images from testing dataset. Left to Right: (a) Original RGB image, (b) Ground truth annotation, (c) Predicted masks using trained MAnet model with mit_b4 backbone, (d) Predicted masks using trained DeepLabV3+ model with Res-Net101 backbone (e) Predicted masks using trained PSPNet model with mit_b5 backbone, (f) Predicted masks using trained Unet++ model with ResNet50 backbone.

The DL model exhibited certain limitations in accurately distinguishing between specific vegetation species, particularly among morphologically similar grass types. As illustrated in Figure 3-3, notable confusion occurred between Johnson grass, Crabgrass, and Browntop millet, where the model occasionally misclassified these species as one another. This performance limitation can be primarily attributed to the high degree of visual similarity among these grass species, which share comparable physical characteristics in terms of blade structure, color, and growth patterns. In contrast, the model demonstrated superior performance in detecting and classifying grass species with more distinctive morphological features, such as Lespedeza, Bahia, Bermuda, and Fescue, as shown in Figure 3-1. These species possess unique visual characteristics that enable more reliable differentiation, resulting in more accurate classification outcomes. This observation high-lights the model's strength in distinguishing vegetation species with distinct features while acknowledging its current limitations in differentiating between visually similar grass types, suggesting potential areas for future model refinement and enhancement.

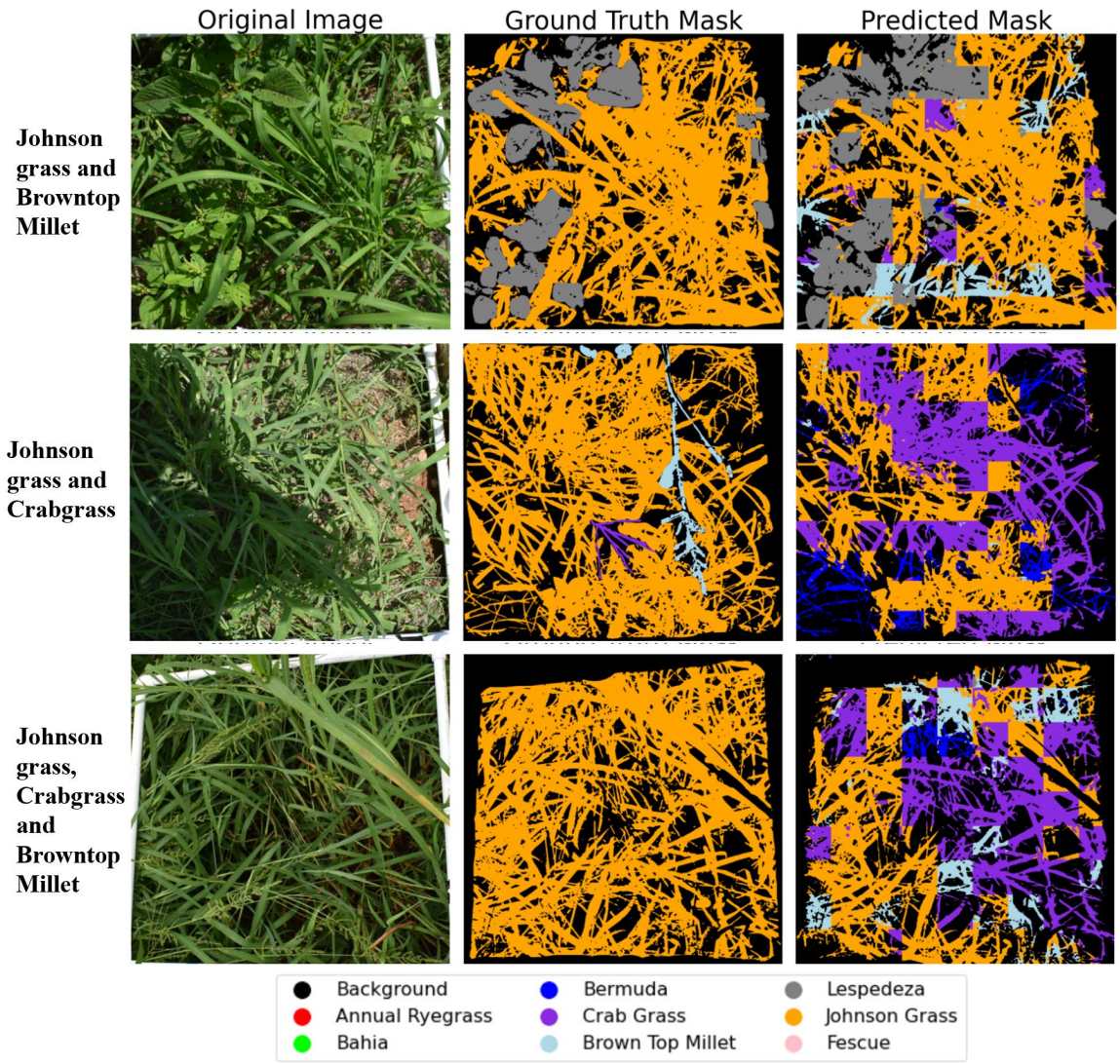

Figure 3-3: Misclassifications in composition assessment by the DL model.

3.2 VEGETATION DETECTION USING VEGETATION INDICES METHODS

3.2.1 Vegetation detection at Prattville construction site

The VI maps help measure the chlorophyll content, which were then used to assess vegetation coverage at construction sites. VI maps were generated in QGIS software for this purpose. NDVI maps (Figure 3-5) were created using NIR and Red orthomosaics from the Prattville construction site to analyze vegetation health and density. Similarly, NDRE maps (Figure 3-6) were generated using NIR and red edge orthomosaics, while SAVI maps (Figure 3-7) were developed using NIR and red orthomosaics, all processed within QGIS software.

Figure 3-4: RGB ortho mosaic image of the Tuscaloosa construction site.

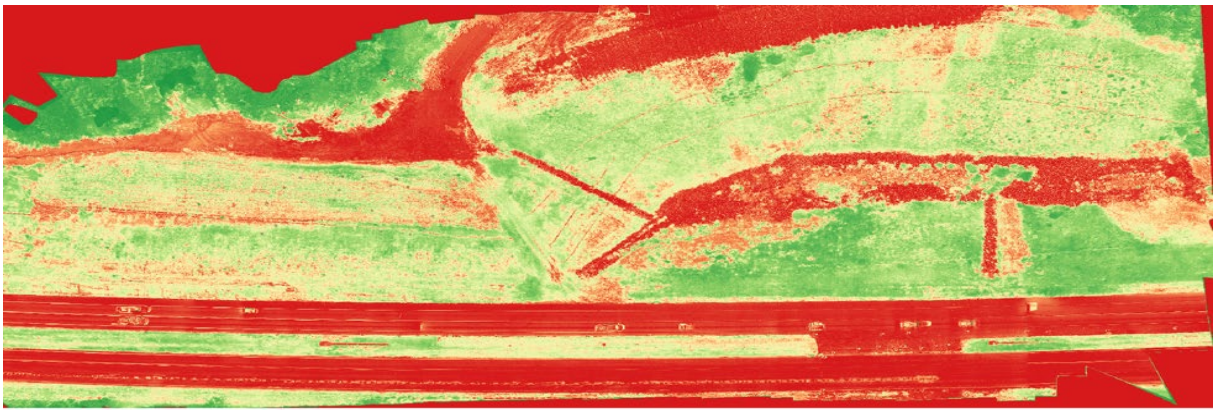

Figure 3-5: NDVI ortho mosaic image of the Prattville construction site.

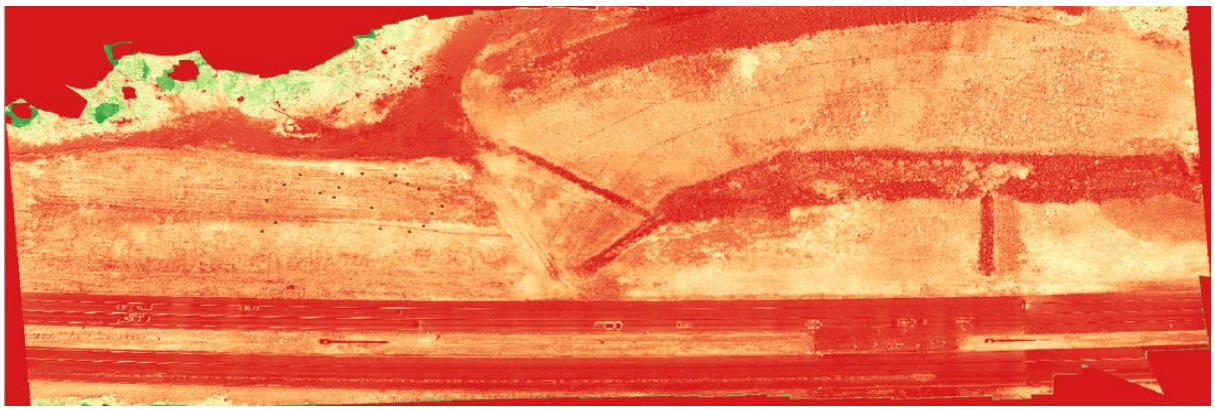

Figure 3-6: NDRE ortho mosaic image of the Prattville construction site.

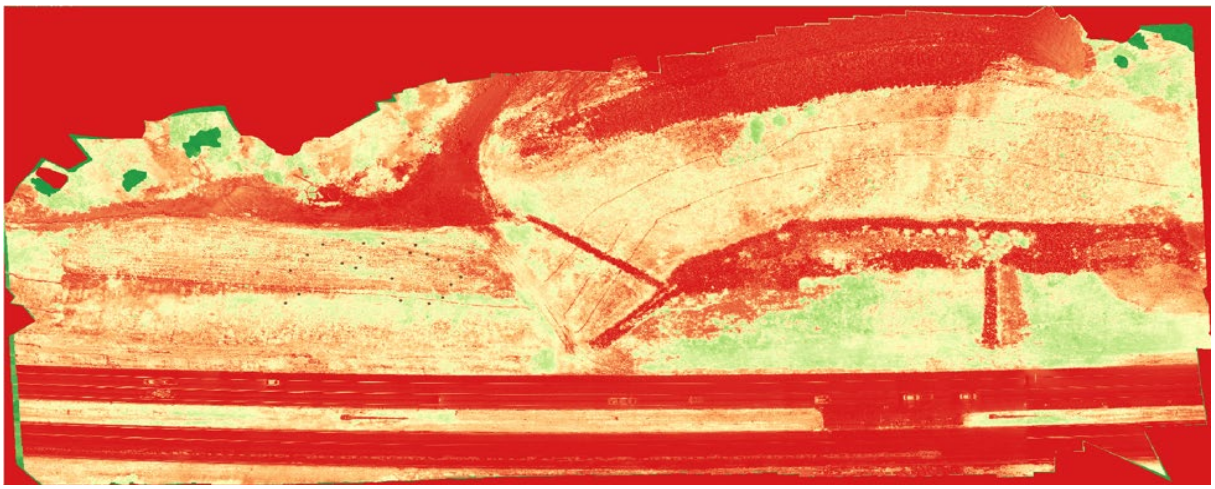

Figure 3-7: The SAVI ortho mosaic image of the Prattville construction site.

PVC frames measuring 0.6 m × 0.6 m were manually placed at selected sites to facilitate vegetation cover and grass species analysis. This focused approach allowed for more precise and efficient assessments compared to evaluating the entire area. Figure 3-8 illustrates magnified sections of an RGB image (above) and its corresponding NDVI map (below), with each frame assigned a unique serial number.

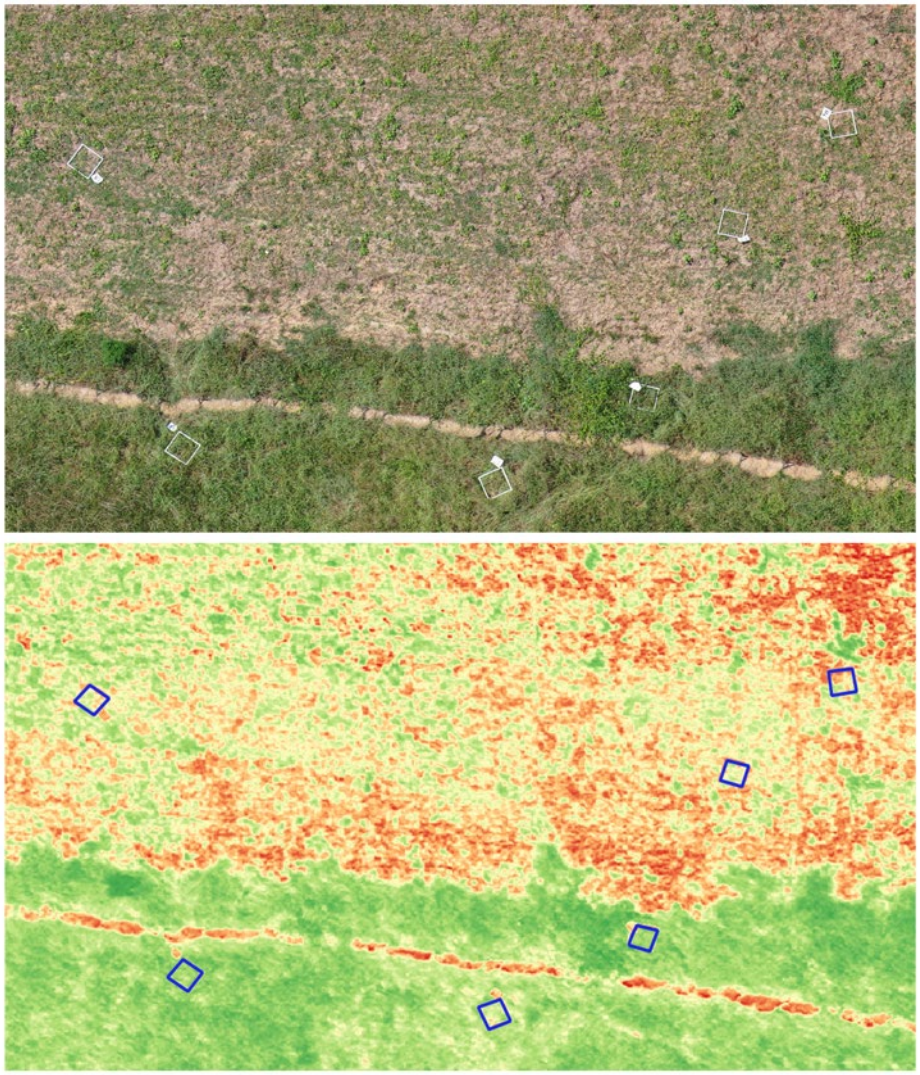

Figure 3-8: Zoomed snippet of a similar area from RGB image (above) and NDVI map (below) from Prattville construction site.

The zonal statistics for the optimal thresholds of various VI used to estimate vegetation cover for Prattville construction site are presented in Table 3-2

Table 3-2: Zonal statistics on selected patches at the Prattville construction site.

Frame id	Actual vegetation cover	Predicted vegetation cover: Deep Learning	Predicted vegetation cover: NDVI – 0.5	Predicted vegetation cover: NDRE – 0.25	Predicted vegetation cover: SAVI – 0.40
1	0.357	0.345 *(Testing)*	0.667	0.713	0.646
2	0.242	0.239 (Training)	0.480	0.480	0.423
3	0.009	0.008 (Training)	0.008	0.104	0.008
4	0.257	0.264 (Training)	0.545	0.500	0.519
5	0.229	0.220 *(Testing)*	0.423	0.531	0.379
6	0.495	0.500 (Training)	0.930	0.885	0.886
7	0.332	0.331 (Training)	0.891	0.798	0.813
8	0.398	0.391 (Training)	0.952	0.871	0.949
9	0.357	0.363 (Training)	0.768	0.685	0.711
10	0.136	0.134 *(Testing)*	0.286	0.472	0.196
11	0.186	0.192 (Training)	0.478	0.450	0.282
12	0.291	0.290 (Training)	0.767	0.710	0.694
13	0.354	0.355 (Training)	0.766	0.743	0.715
14	0.338	0.335 (Training)	0.753	0.711	0.695
15	0.261	0.278 *(Testing)*	0.533	0.582	0.417
16	0.413	0.392 (Training)	0.870	0.878	0.870
17	0.251	0.235 (Training)	0.698	0.616	0.654
18	0.368	0.354 (Training)	0.928	0.880	0.925
19	0.304	0.307 (Training)	0.595	0.639	0.505
20	0.218	0.217 *(Testing)*	0.286	0.296	0.269

To identify optimal thresholds for VI's that best matched actual vegetation cover at the construction site, various ranges were tested. For NDVI (range: 0.25–0.60), a threshold of 0.50 yielded the highest R^2 and lowest *MAE,RMSE*. NDRE performed best at 0.25 (range: 0.20–0.45), while SAVI achieved optimal results at 0.40 (range: 0.20–0.55), all providing accurate vegetation representation.

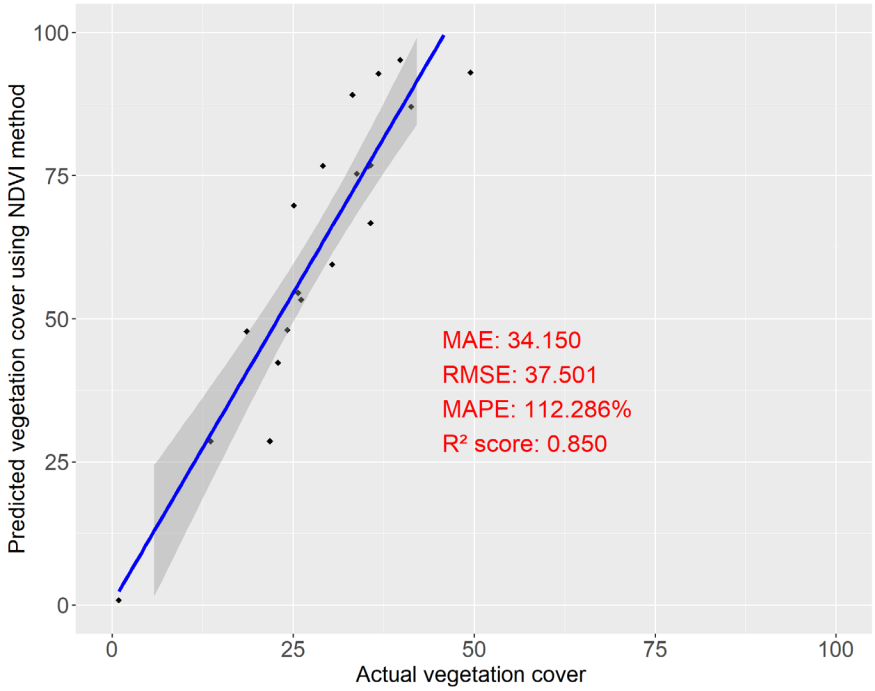

Figure 3-9: Scatterplot for NDVI-based VI method to predict the vegetation cover at Prattville construction sites.

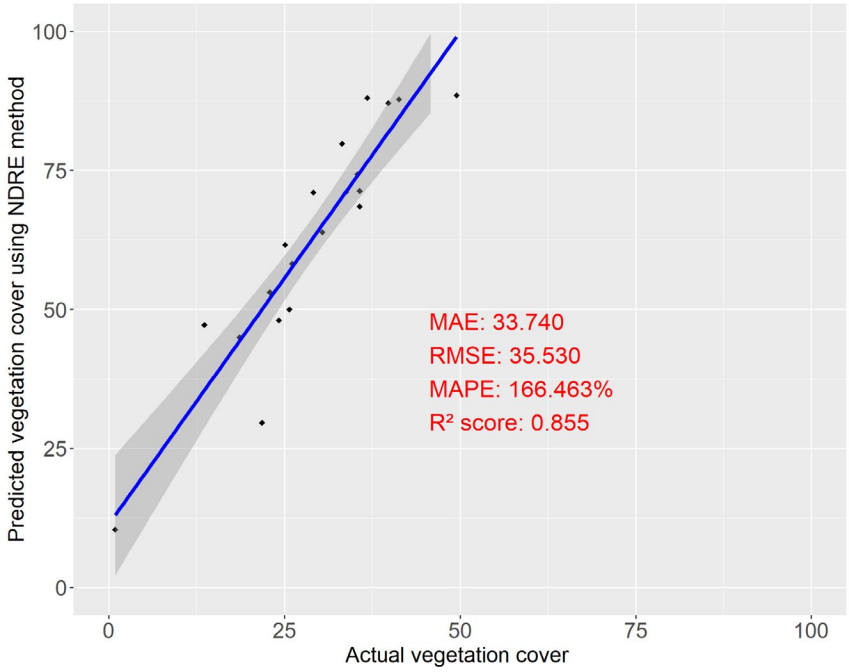

Figure 3-10: Scatterplot for NDRE-based VI method to predict the vegetation cover at Prattville construction sites.

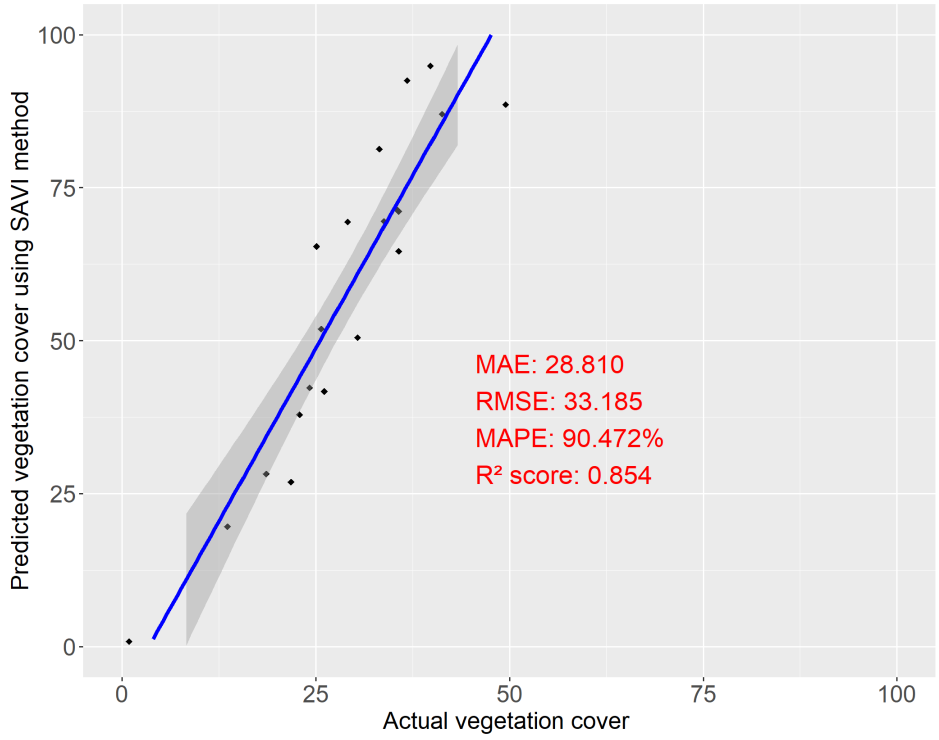

Figure 3-11: Scatterplot for SAVI-based VI method to predict the vegetation cover at Prattville construction sites.

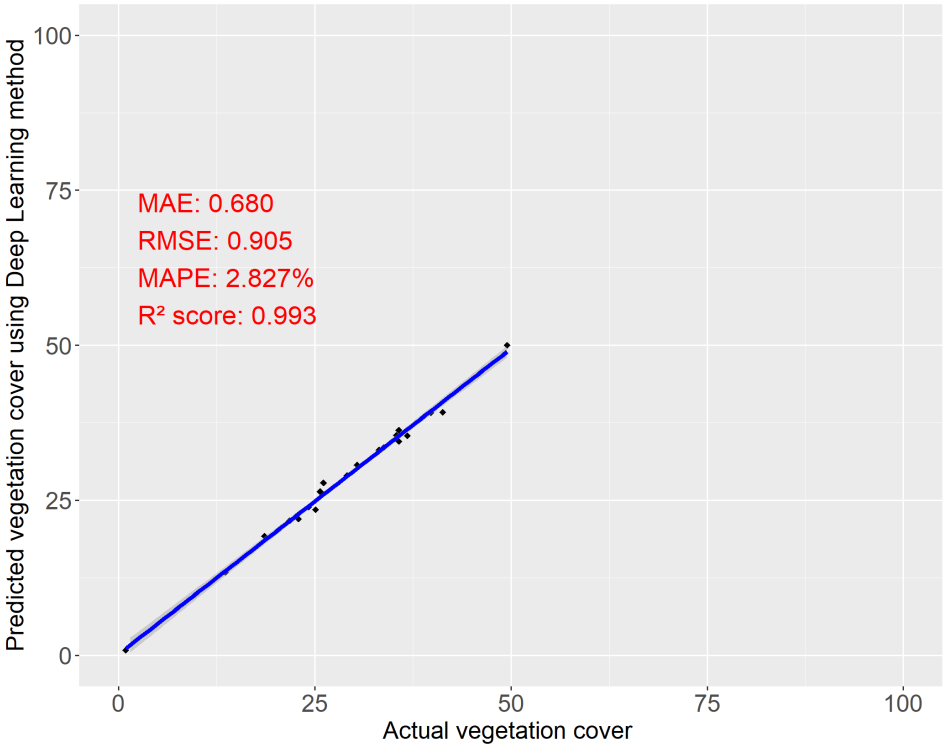

Figure 3-12: Scatterplot for Deep Learning model to predict the vegetation cover at Prattville construction sites.

The DL model outperformed the VI-based methods in predicting the ground truth vegetation cover, achieving the highest R^2 score, lowest *MAE* and *RMSE*. This indicates that the DL model provided the most accurate and reliable representation of vegetation cover compared to NDVI, NDRE, and SAVI methods

3.2.2 Vegetation detection at Tuscaloosa construction site

Figure 3-13: The RGB ortho mosaic image of the Tuscaloosa construction site.

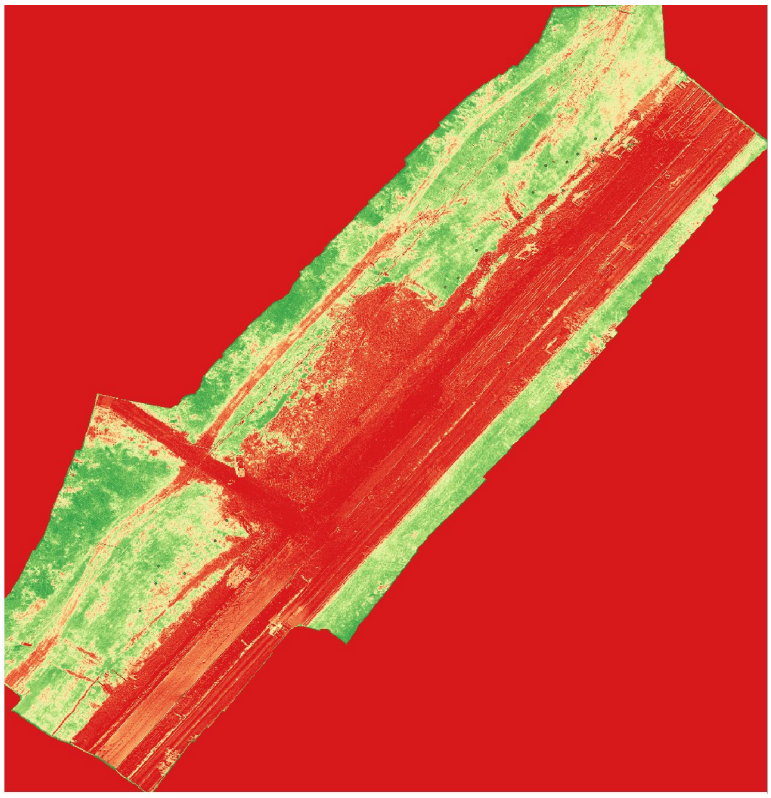

Figure 3-14: The NDVI ortho mosaic image of the Tuscaloosa construction site.

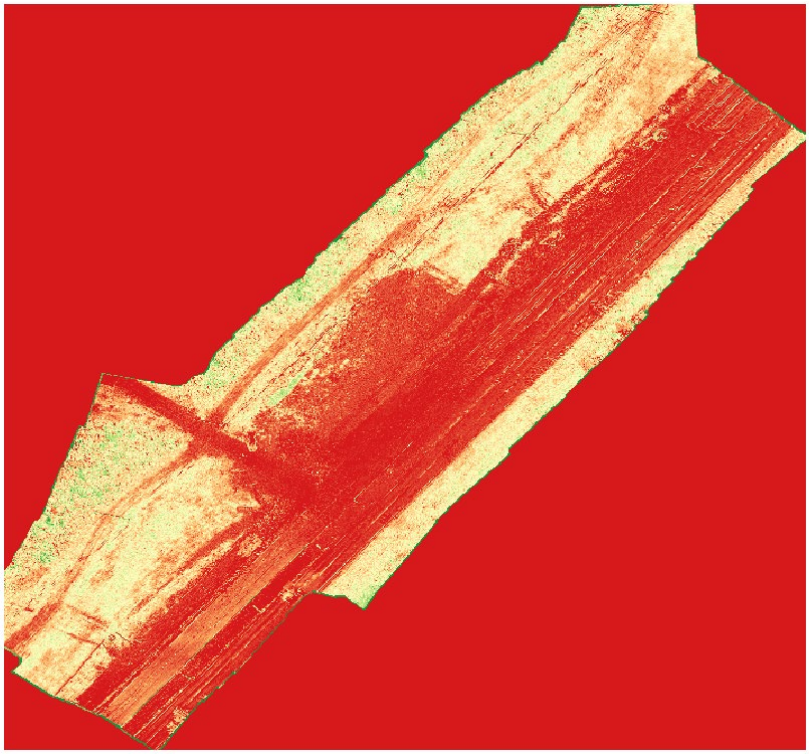

Figure 3-15: The NDRE ortho mosaic image of the Tuscaloosa construction site.

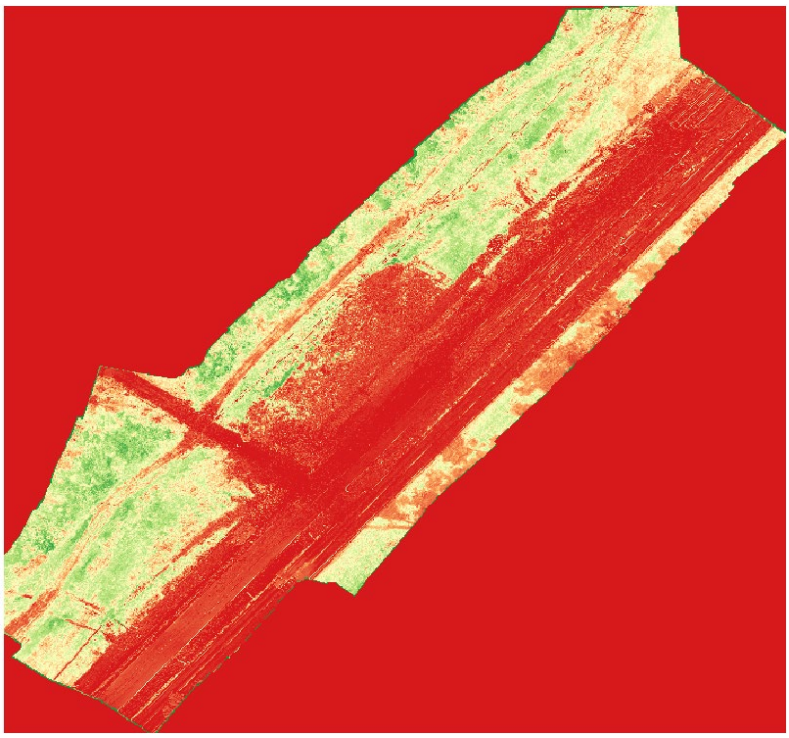

Figure 3-16. The SAVI ortho mosaic image of the Tuscaloosa construction site.

A total of 18 frames were laid at the Tuscaloosa location, and the vegetation cover within these patches was determined. The 'Zonal Statistics' feature in QGIS was used to extract the following metrics for the segmented frames: 'Count', representing the total number of pixel values in each frame; 'Vegetation', indicating the count of pixels corresponding to healthy vegetation; and 'Percentage Cover', which reflects the proportion of healthy vegetation pixels within each frame. The values obtained through the zonal statistics feature in QGIS are presented in Table 3-3.

Table 3-3: Zonal statistics on selected patches at the Tuscaloosa construction site.

Frame id	Actual vegetation cover	Predicted vegetation cover: Deep Learning	Predicted vegetation cover: NDVI – 0.5	Predicted vegetation cover: NDRE – 0.25	Predicted vegetation cover: SAVI – 0.40
1	0.348	0.359 *(Testing)*	0.728	0.693	0.634
2	0.026	0.038 (Training)	0.000	0.060	0.000
3	0.049	0.056 (Training)	0.091	0.091	0.100
4	0.529	0.538 (Training)	0.893	0.881	0.875
5	0.394	0.412 (Training)	0.790	0.717	0.767
6	0.479	0.485 *(Testing)*	0.929	0.919	0.931
7	0.595	0.590 (Training)	0.909	0.924	0.922
8	0.187	0.176 (Training)	0.275	0.127	0.252
9	0.621	0.636 *(Testing)*	0.925	0.945	0.931
10	0.353	0.366 (Training)	0.546	0.509	0.540
11	0.36	0.415 (Training)	0.817	0.738	0.798
12	0.551	0.566 (Training)	0.834	0.850	0.841
13	0.352	0.365 *(Testing)*	0.556	0.542	0.568
14	0.491	0.504 (Training)	0.732	0.717	0.715
15	0.397	0.406 (Training)	0.728	0.706	0.717
16	0.119	0.135 (Training)	0.232	0.097	0.206
17	0.294	0.299 *(Testing)*	0.438	0.381	0.422
18	0.149	0.109 (Training)	0.312	0.212	0.242

Thresholds for vegetation cover were optimized by testing different ranges for each vegetation index. For NDVI (0.25–0.60), a threshold of 0.50 gave the best results with the highest R^2 and lowest *MAE, RMSE*. NDRE performed best at a threshold of 0.25 (range: 0.20–0.45), and SAVI at 0.40 (range: 0.20–0.55), both yielding the most accurate vegetation representation.

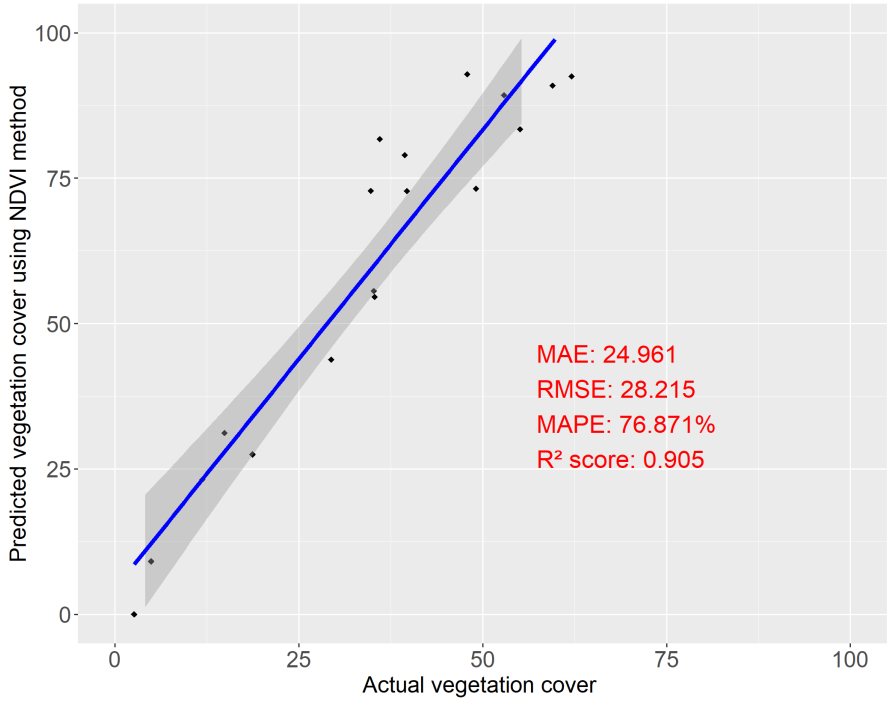

Figure 3-17: Scatterplot for NDVI-based VI method to predict the vegetation cover at Tuscaloosa construction sites.

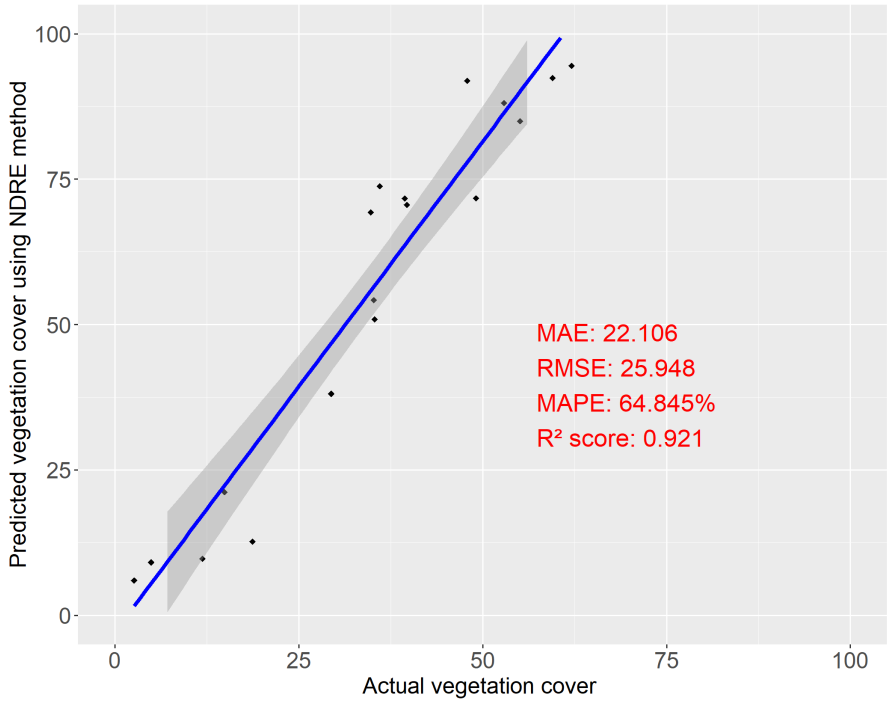

Figure 3-18: Scatterplot for NDRE-based VI method to predict the vegetation cover at Tuscaloosa construction sites.

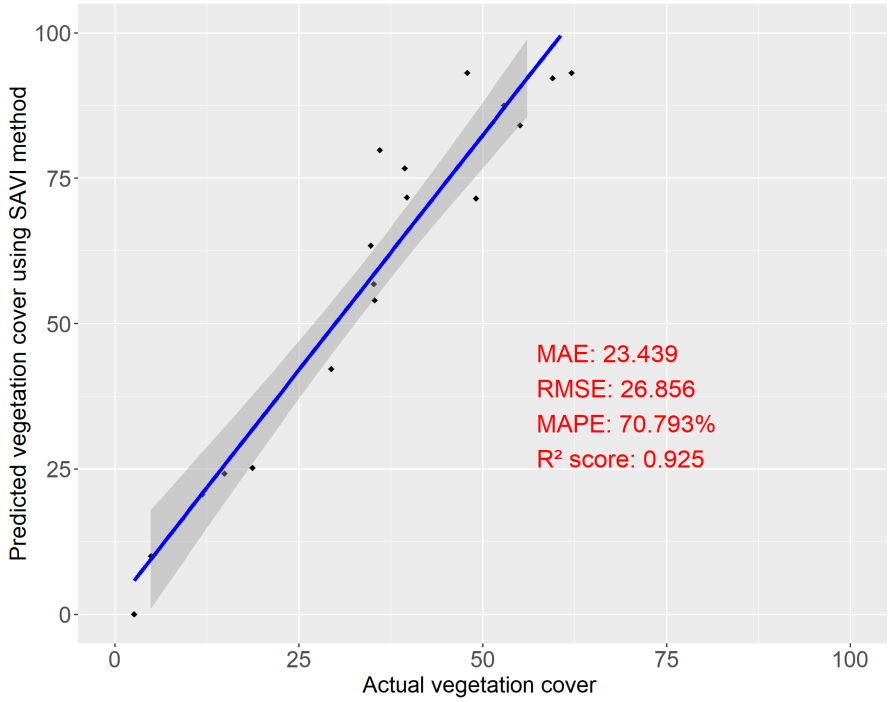

Figure 3-19: Scatterplot for SAVI-based VI method to predict the vegetation cover at Tuscaloosa construction sites.

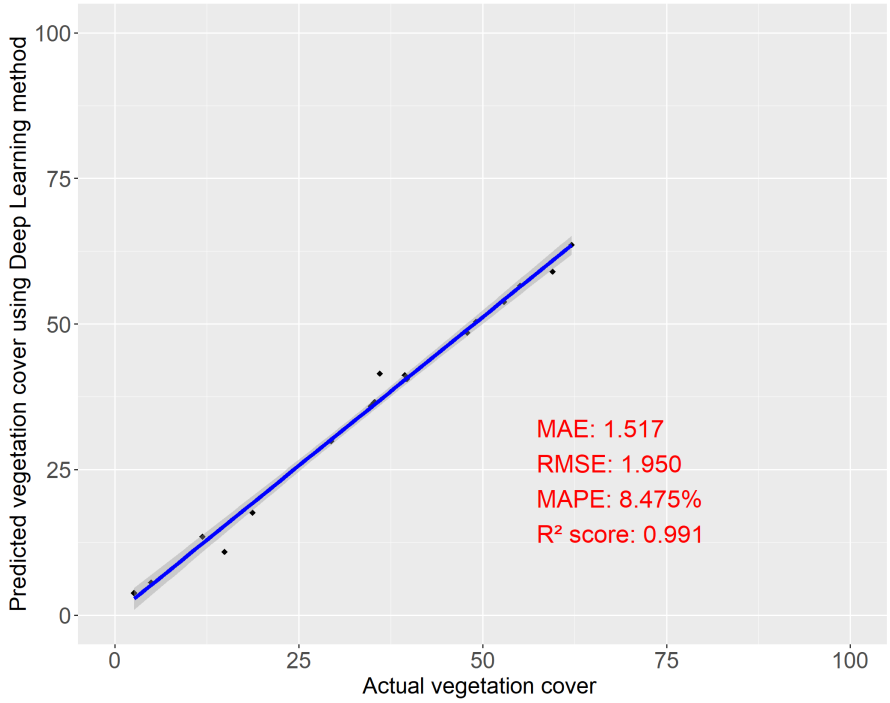

Figure 3-20: Scatterplot for Deep Learning model to predict the vegetation cover at Tuscaloosa construction sites.

The DL model outperformed the vegetation index-based methods in predicting the ground truth vegetation cover, achieving the highest R^2 score, lowest *MAE* and *RMSE*. This

indicates that the DL model provided the most accurate and reliable representation of vegetation cover compared to NDVI, NDRE, and SAVI methods.

3.2.3 Vegetation detection at Linden construction site

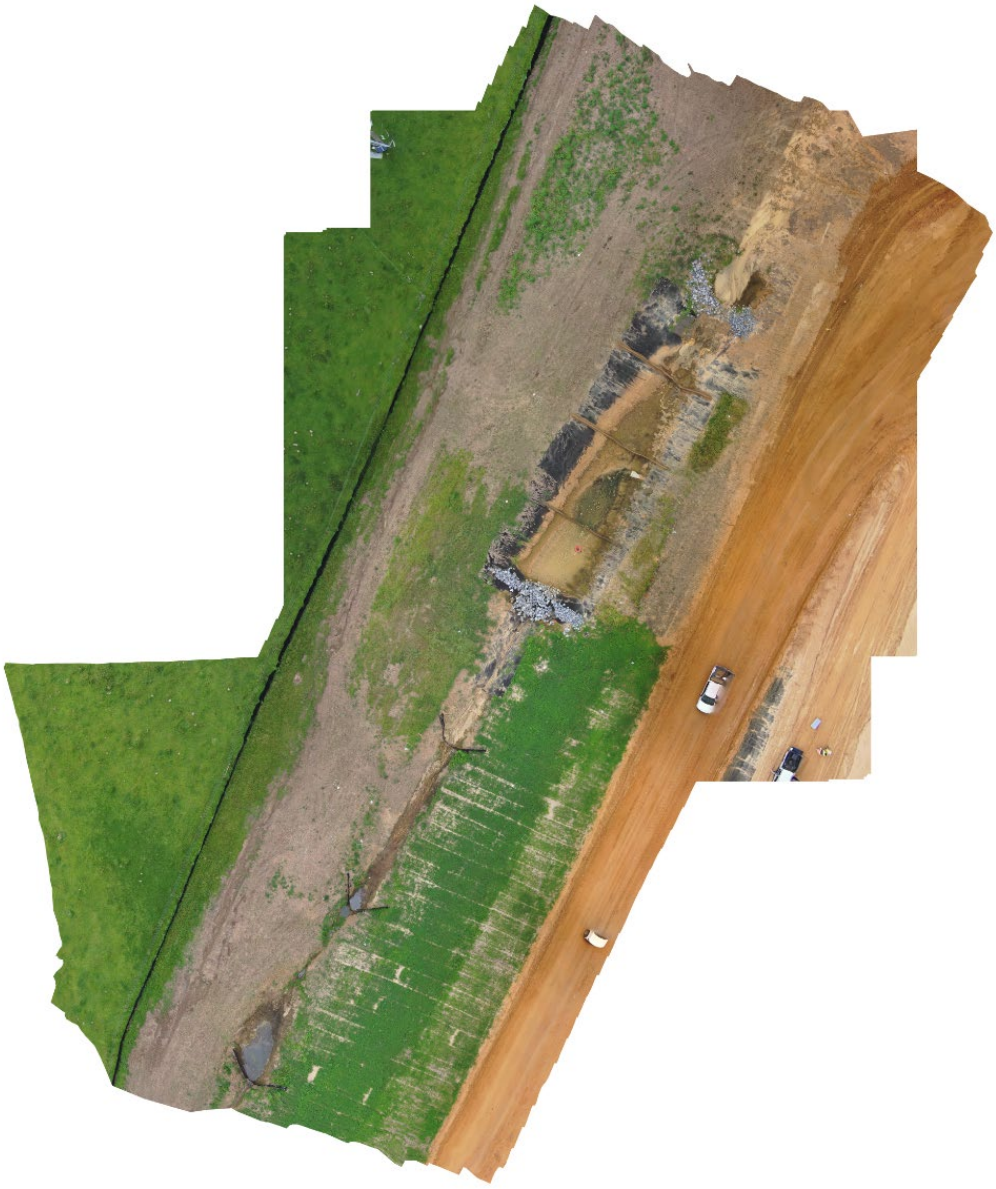

Figure 3-21: The RGB ortho mosaic image of the Linden construction site.

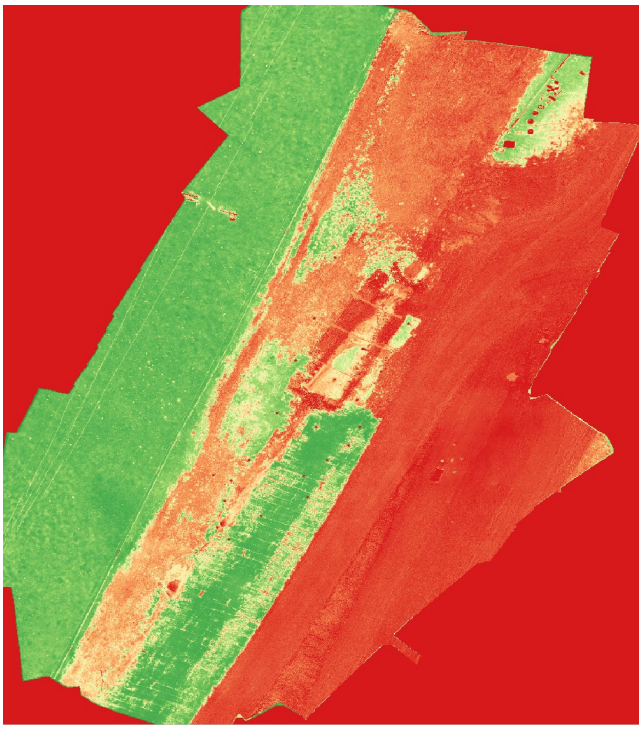

Figure 3-22: The NDVI ortho mosaic image of the Linden construction site.

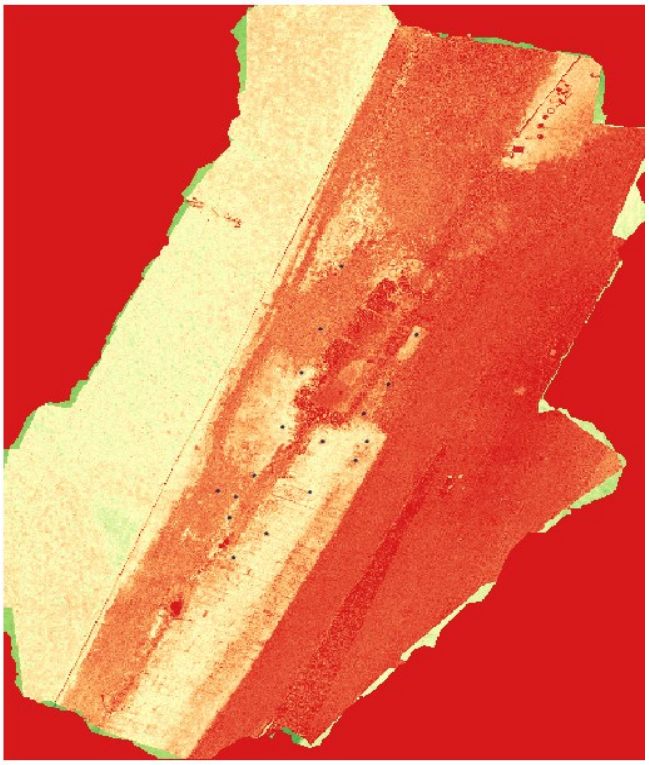

Figure 3-23: The NDRE ortho mosaic image of the Linden construction site.

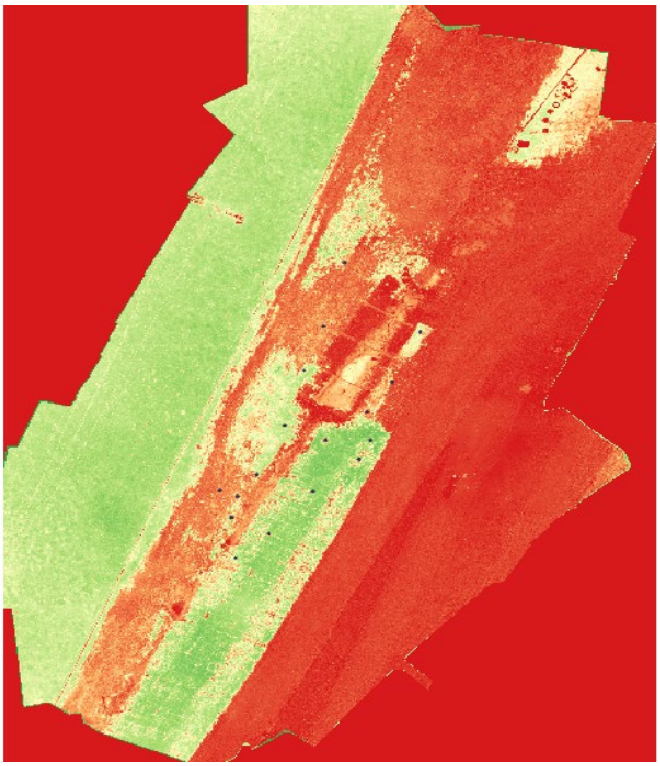

Figure 3-24: The SAVI ortho mosaic image of the Linden construction site.

A total of 17 frames were laid at the Linden location, and the vegetation cover within these patches was determined. The 'Zonal Statistics' feature in QGIS was used to extract the following metrics for the segmented frames: 'Count', representing the total number of pixel values in each frame; 'Vegetation', indicating the count of pixels corresponding to healthy vegetation; and 'Percentage Cover', which reflects the proportion of healthy vegetation pixels within each frame. The values obtained through the zonal statistics feature in QGIS are presented in Table 3-4.

Table 3-4: Zonal statistics on selected patches at the Linden construction site.

Frame id	Actual vegetation cover	Predicted vegetation cover: Deep Learning	Predicted vegetation cover: NDVI – 0.5	Predicted vegetation cover: NDRE – 0.25	Predicted vegetation cover: SAVI – 0.40
1	0.256	0.257 *(Testing)*	0.093	0.244	0.038
2	0.757	0.765 (Training)	0.988	0.960	0.983
3	0.524	0.511 (Training)	0.801	0.809	0.647
4	0.117	0.113 (Training)	0.000	0.007	0.000
5	0.607	0.594 *(Testing)*	0.854	0.845	0.836
6	0.739	0.756 (Training)	0.878	0.979	0.915
7	0.707	0.693 (Training)	0.879	0.965	0.866
8	0.508	0.500 (Training)	0.613	1.000	0.632
9	0.101	0.101 *(Testing)*	0.025	0.691	0.007
10	0.445	0.458 (Training)	0.601	0.167	0.632
11	0.379	0.379 (Training)	0.439	0.800	0.488
12	0.639	0.621 (Training)	0.957	0.769	0.942
13	0.130	0.137 *(Testing)*	0.000	1.000	0.000
14	0.511	0.518 (Training)	0.706	0.055	0.672
15	0.448	0.454 (Training)	0.439	0.573	0.448
16	0.700	0.707 *(Testing)*	0.968	0.684	0.977

To determine the most accurate vegetation cover using VI's, different threshold ranges were tested. NDVI performed best at a threshold of 0.50 (range: 0.25–0.60), NDRE at 0.25 (range: 0.20–0.45), and SAVI at 0.40 (range: 0.20–0.55), each yielding the highest R^2 and the lowest *MAE* and *RMSE* values.

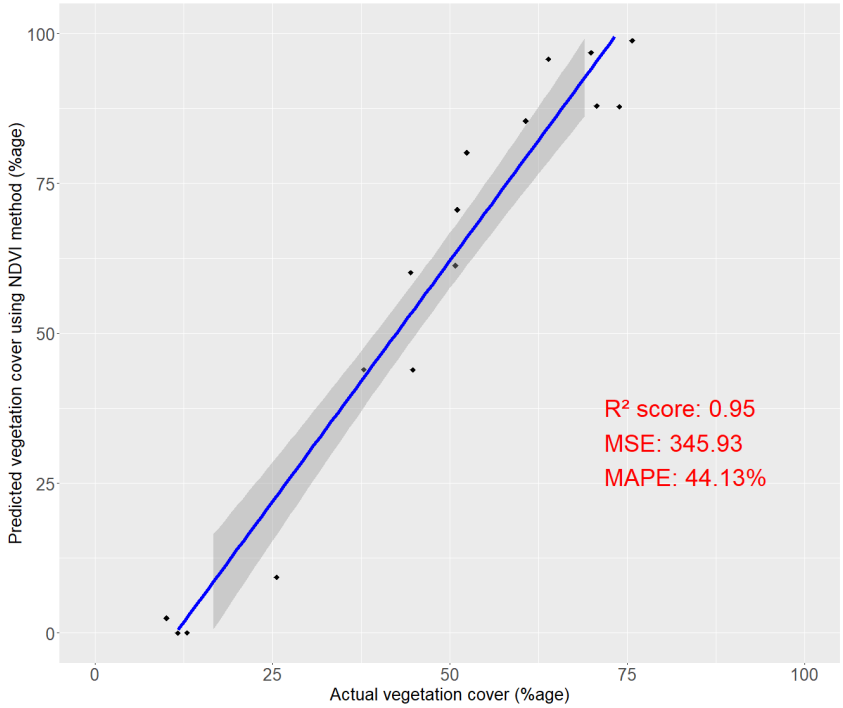

Figure 3-25: Scatterplot for NDVI-based VI method to predict the vegetation cover at Linden construction sites.

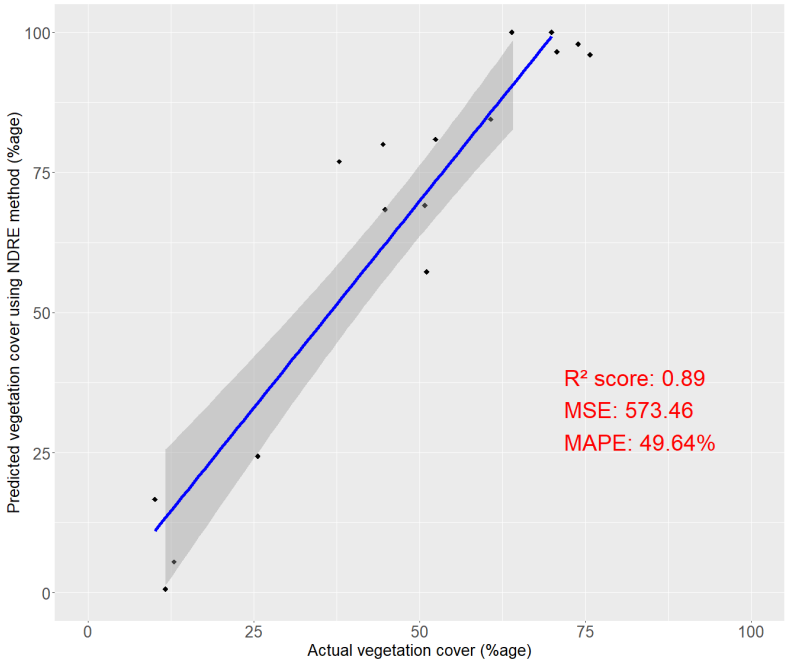

Figure 3-26: Scatterplot for NDRE-based VI method to predict the vegetation cover at Linden construction sites.

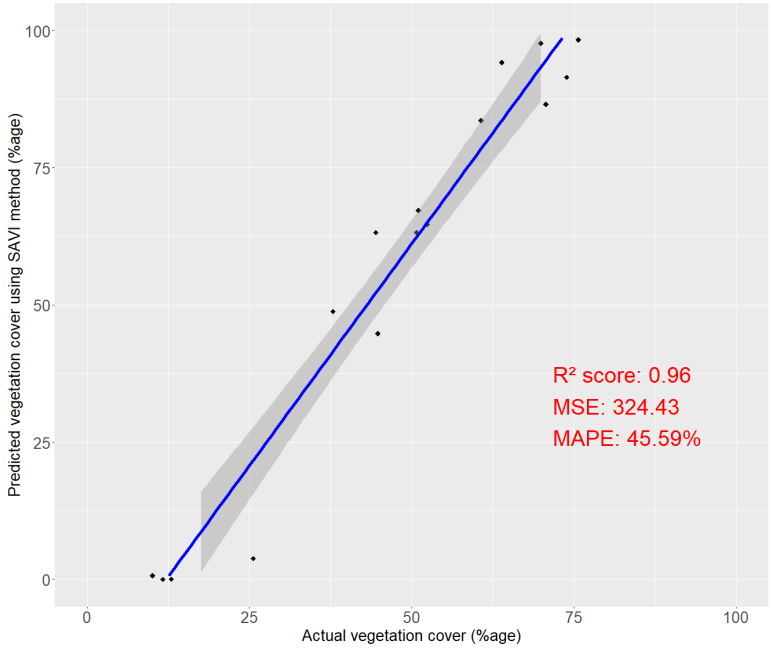

Figure 3-27: Scatterplot for NDRE-based VI method to predict the vegetation cover at Linden construction sites.

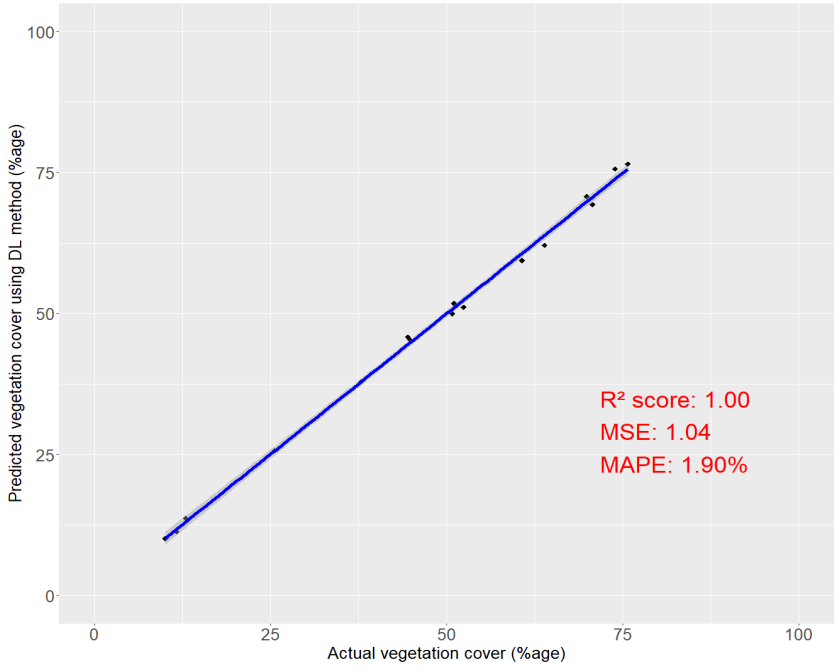

Figure 3-28: Scatterplot for Deep Learning model to predict the vegetation cover at Linden construction sites.

The DL model outperformed the vegetation index-based methods in predicting the ground truth vegetation cover, achieving the highest R^2 score, lowest *MAE* and *RMSE*. This indicates that the DL model provided the most accurate and reliable representation of vegetation cover compared to NDVI, NDRE, and SAVI methods.

3.2.4 Opelika-Stormwater research center facility

Figure 3-29: The RGB ortho mosaic image of the Opelika-Stormwater Research Center Facility.

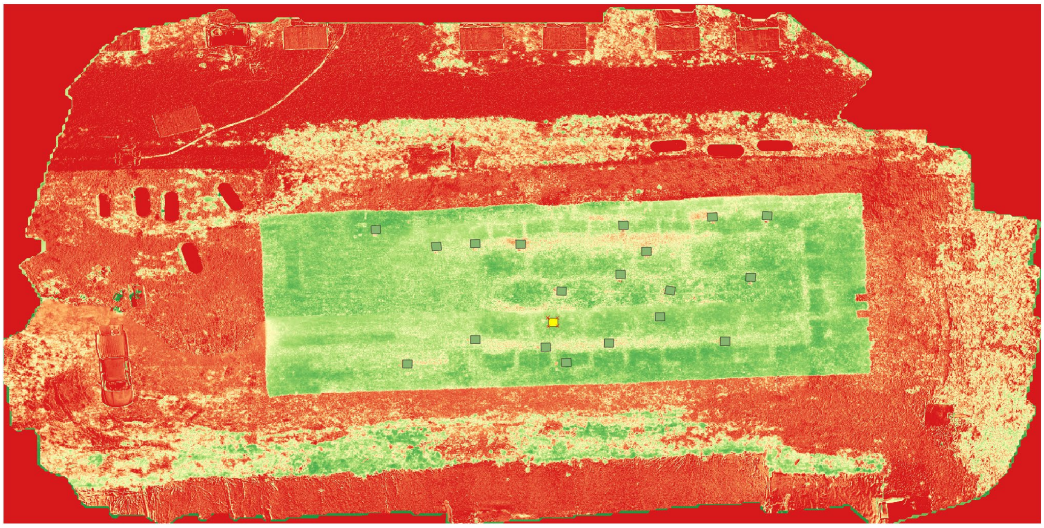

Figure 3-30: The NDVI ortho mosaic image of the Opelika-Stormwater Research Center Facility.

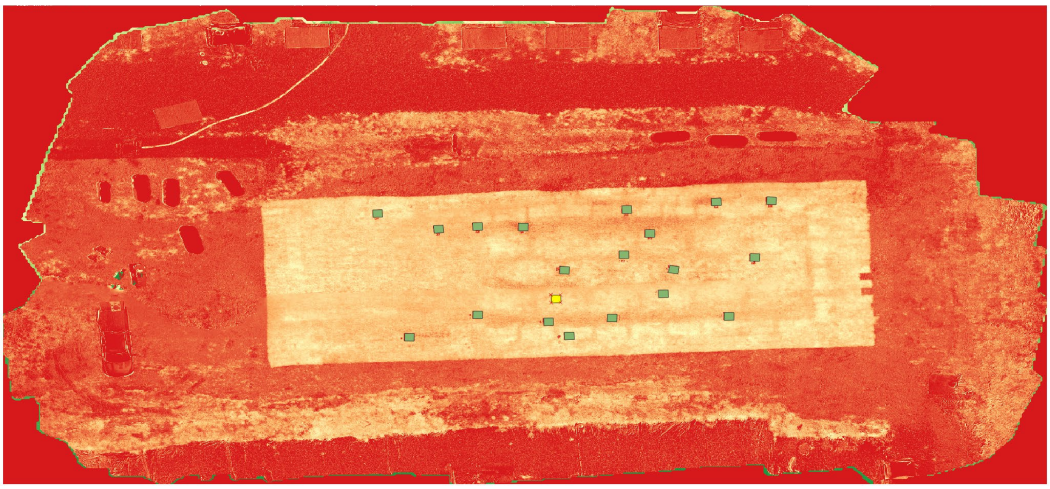

Figure 3-31: The NDRE ortho mosaic image of the Opelika-Stormwater Research Center Facility.

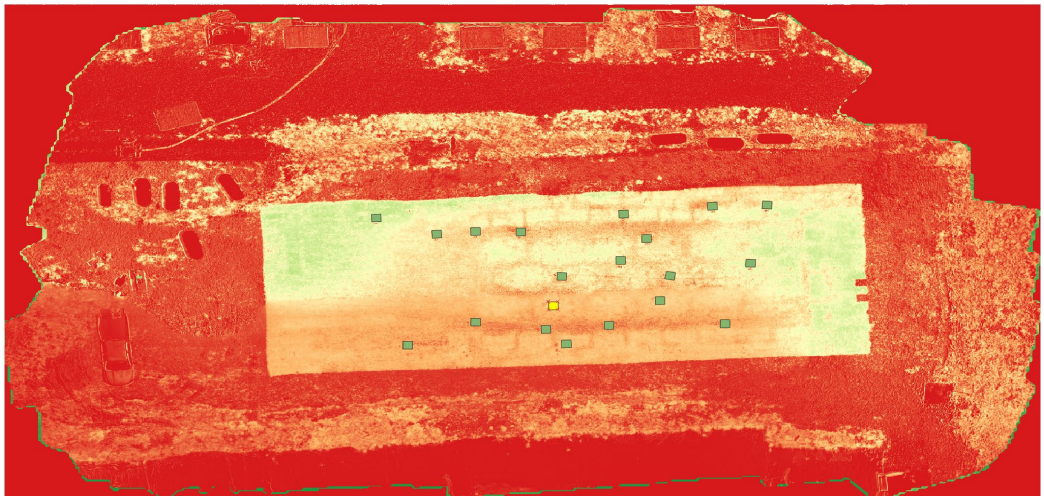

Figure 3-32: The SAVI ortho mosaic image of the Opelika-Stormwater Research Center Facility.

A total of 20 frames were laid at the Opelika-Stormwater Research Center Facility in Opelika, AL, and the vegetation cover within these patches was determined. The 'Zonal Statistics' feature in QGIS was used to extract the following metrics for the segmented frames: 'Count', representing the total number of pixel values in each frame; 'Vegetation', indicating the count of pixels corresponding to healthy vegetation; and 'Percentage Cover', which reflects the proportion of healthy vegetation pixels within each frame. The values obtained through the zonal statistics feature in QGIS are presented in Table 3-5.

Table 3-5: Zonal statistics on selected patches at Stormwater Research Center Facility.

Frame id	Actual vegetation cover	Predicted vegetation cover: Deep Learning	Predicted vegetation cover: NDVI – 0.5	Predicted vegetation cover: NDRE – 0.25	Predicted vegetation cover: SAVI – 0.40
1	0.686	0.691 *(Testing)*	0.289	0.027	0.266
2	0.854	0.854 (Training)	0.923	0.978	0.912
3	0.754	0.757 (Training)	0.372	0.925	0.424
4	0.693	0.691 (Training)	0.223	0.760	0.145
5	0.500	0.495 (Training)	0.041	0.204	0.003
6	0.715	0.714 *(Testing)*	0.504	0.825	0.447
7	0.638	0.638 (Training)	0.200	0.744	0.254
8	0.608	0.609 (Training)	0.431	0.830	0.404
9	0.661	0.660 (Training)	0.291	0.574	0.255
10	0.803	0.799 *(Testing)*	0.477	0.891	0.414
11	0.814	0.816 (Training)	0.840	0.969	0.807
12	0.723	0.726 (Training)	0.564	0.139	0.467
13	0.872	0.873 (Training)	0.905	0.869	0.885
14	0.730	0.733 (Training)	0.567	0.759	0.606
15	0.723	0.725 (Training)	0.425	0.871	0.428
16	0.563	0.560 *(Testing)*	0.145	0.000	0.065
17	0.876	0.875 (Training)	0.890	0.732	0.888
18	0.679	0.682 (Training)	0.423	0.006	0.328
19	0.843	0.845 (Training)	0.885	0.873	0.888
20	0.626	0.631 *(Testing)*	0.461	0.005	0.286

To identify optimal thresholds for VI's that best matched actual vegetation cover at the construction site, various ranges were tested. For NDVI (0.25–0.60), a threshold of 0.50 yielded the highest R^2 and lowest *MAE,RMSE*. NDRE performed best at 0.25 (range: 0.20–0.45), while SAVI achieved optimal results at 0.40 (range: 0.20–0.55), all providing accurate vegetation representation.

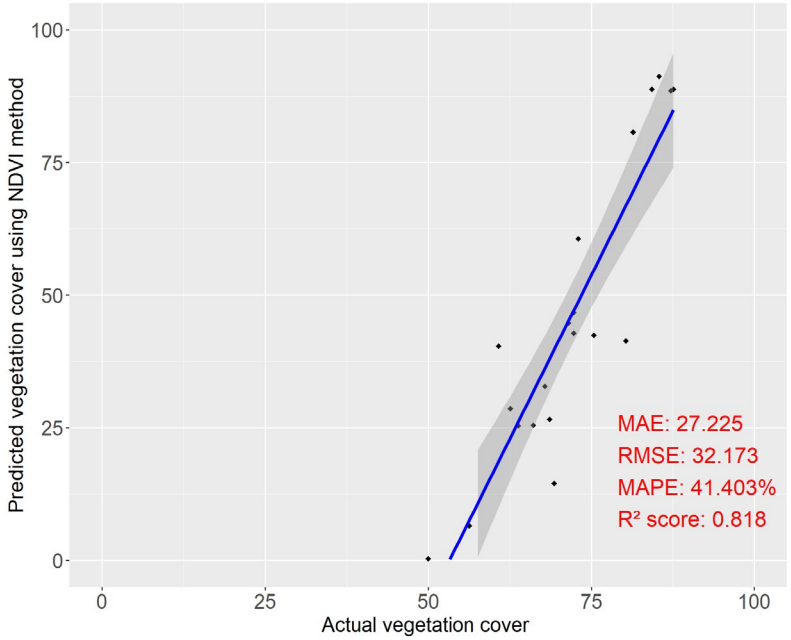

Figure 3-33: Scatterplot for NDVI-based VI method to predict the vegetation cover at construction sites.

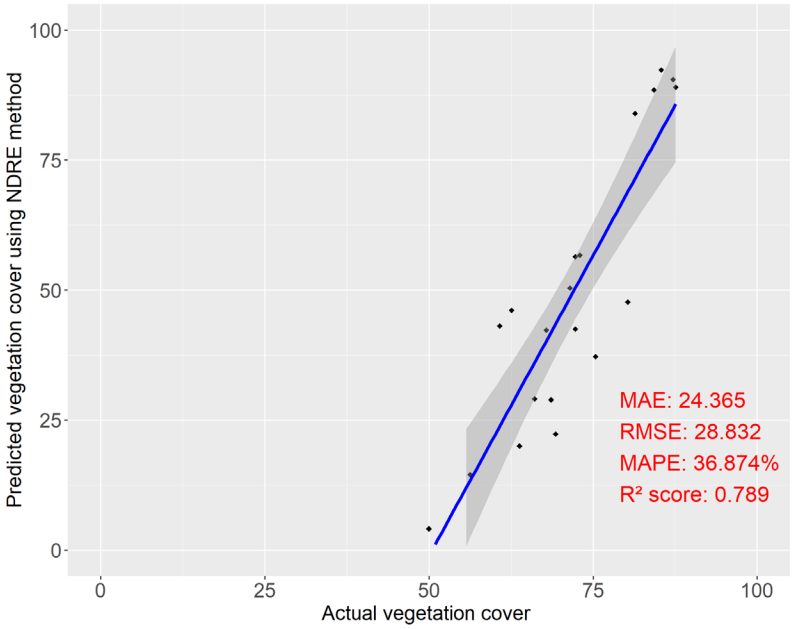

Figure 3-34: Scatterplot for NDRE-based VI method to predict the vegetation cover at construction sites.

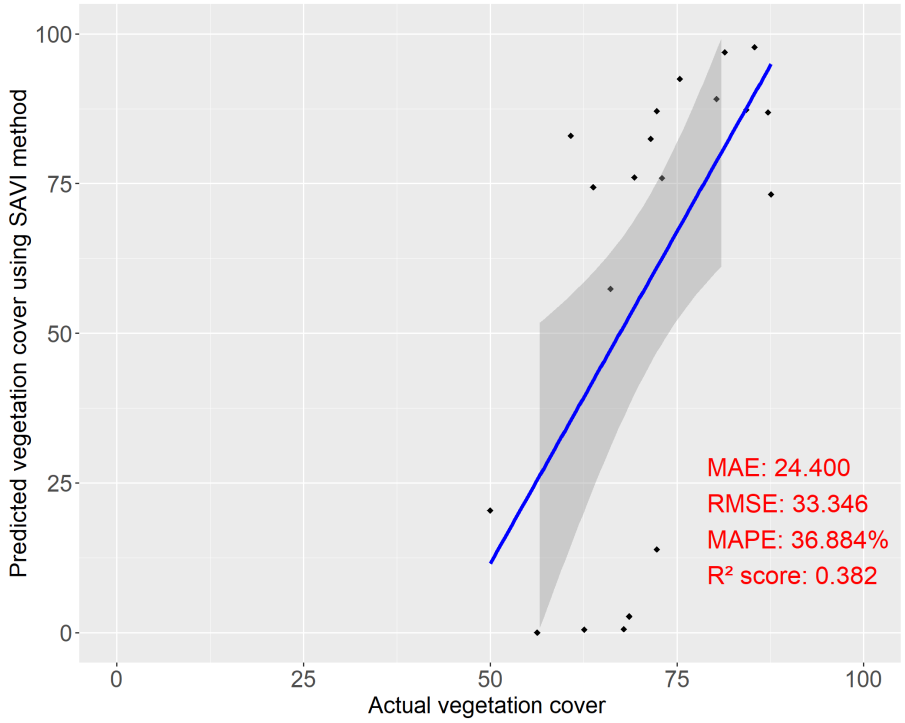

Figure 3-35: Scatterplot for SAVI-based VI method to predict the vegetation cover at construction sites.

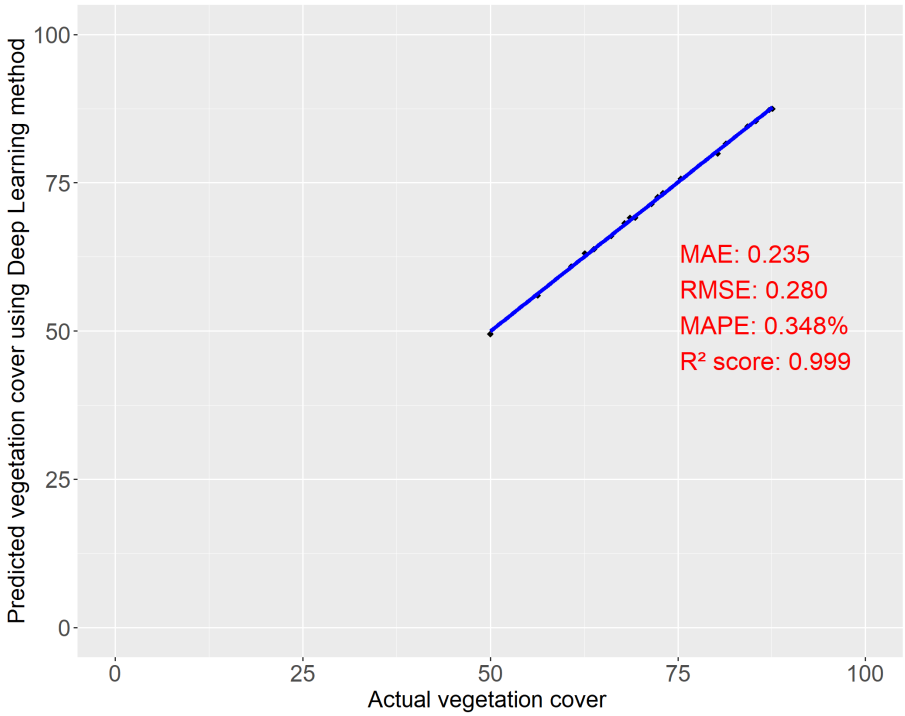

Figure 3-36: Scatterplot for Deep Learning model to predict the vegetation cover at construction sites.

The DL model outperformed the vegetation index-based methods in predicting the ground truth vegetation cover, achieving an acceptable R^2 score *MAE* and *RMSE*. This indicates that the DL model provided the most accurate and reliable representation of vegetation cover compared to NDVI, NDRE, and SAVI methods.

The DL model used for vegetation cover prediction on all the frames collection across Prattville, Linden, Tuscaloosa, and Opelika Stormwater Research Facility.

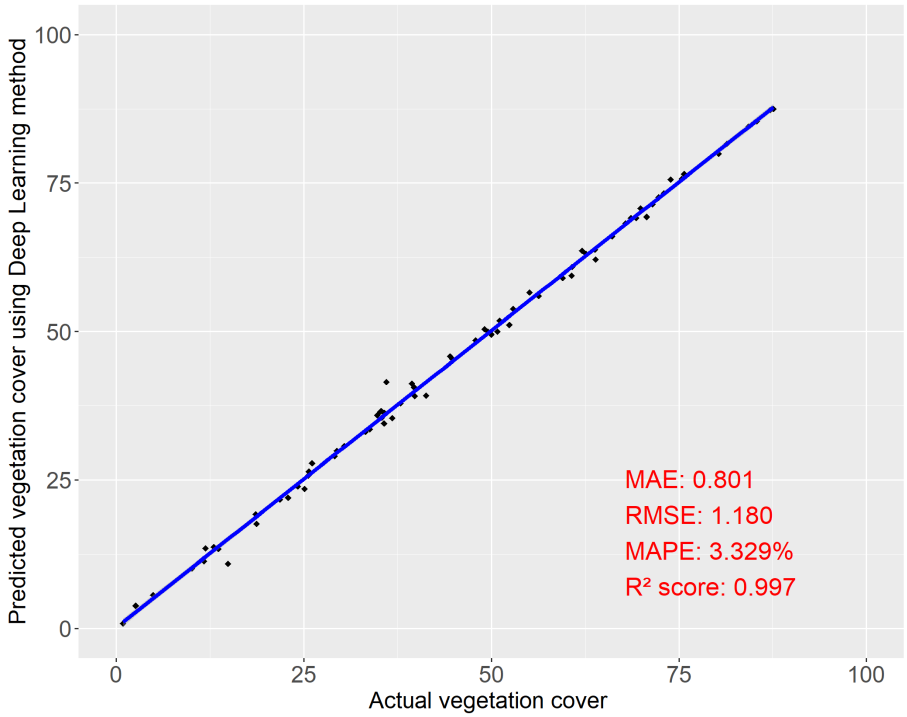

Figure 3-37: Scatterplot for predicted vs actual vegetation cover using best performing DL model.

3.2.5 Determining optimal thresholds for vegetation detection using vegetation indices methods

The NDVI values were standardized with a range of 0 to 1 for consistent interpretation across all study sites. In order to analyze the vegetation coverage, multiple thresh-old-based analyses were performed on the NDVI maps, exploring values between 25% and 60%. This multi-threshold approach was essential as different NDVI values correspond to varying levels of vegetation health and density. The primary objective of exploring multiple thresholds was to identify an optimal threshold value that would yield vegetation predictions closely matching the actual vegetation cover observed in the original frame annotations at the construction sites. The optimal threshold of 50% yielded a higher R^2 score of 0.193, *MAE* value of 28.020, *RMSE* of 32.153, and *MAPE* score of 73.567% demonstrating improved prediction accuracy for NDVI. A scatterplot

illustrating the performance of this threshold in predicting vegetation cover versus actual vegetation cover is shown in Figure 3-38.

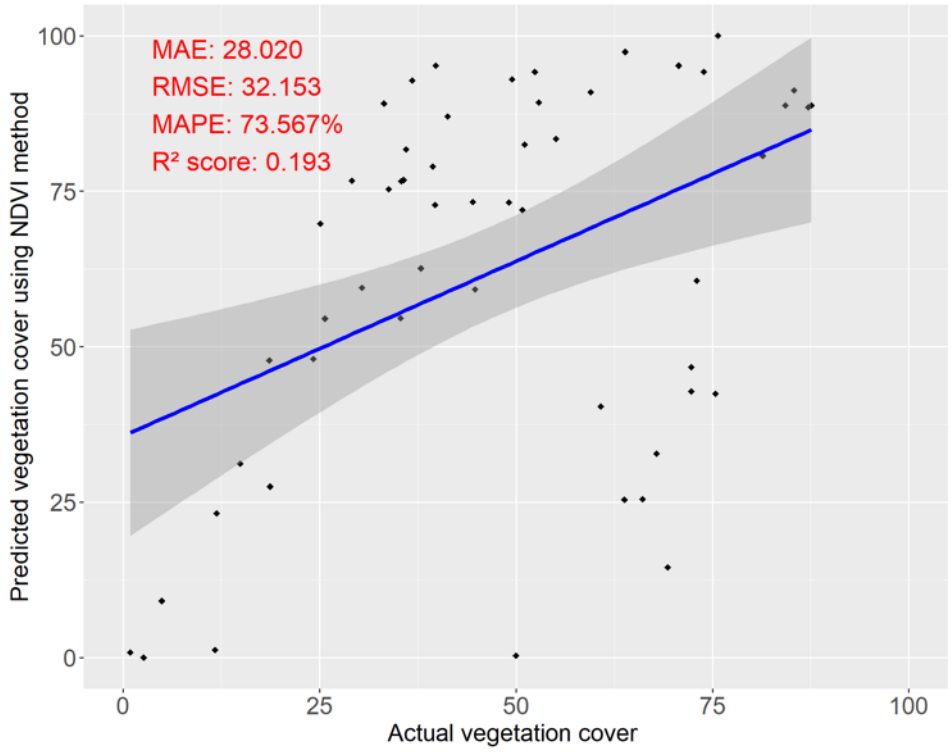

Figure 3-38: Scatterplot for predicted vs actual vegetation cover using best performing NDVI threshold of 50%.

NDRE maps were generated using QGIS software. The NDRE index, which utilizes the red-edge and NIR bands, was computed to provide additional insights into vegetation characteristics, particularly concerning chlorophyll content and plant stress. Multiple threshold values were explored for NDRE maps, ranging from 20% to 50%. This narrower range was observed due to the generally lower pixel values in NDRE compared to other VI, with fewer pixels exceeding values above 0.5 or 50% during analysis. An optimal threshold of 25% for NDRE achieved an improved R^2 score of 0.224, *MAE* of 26.906, *RMSE* of 30.722, and *MAPE* score of 87.012%. Figure 3-39. presents a scatterplot showing the performance of this threshold in predicting vegetation cover versus actual vegetation cover.

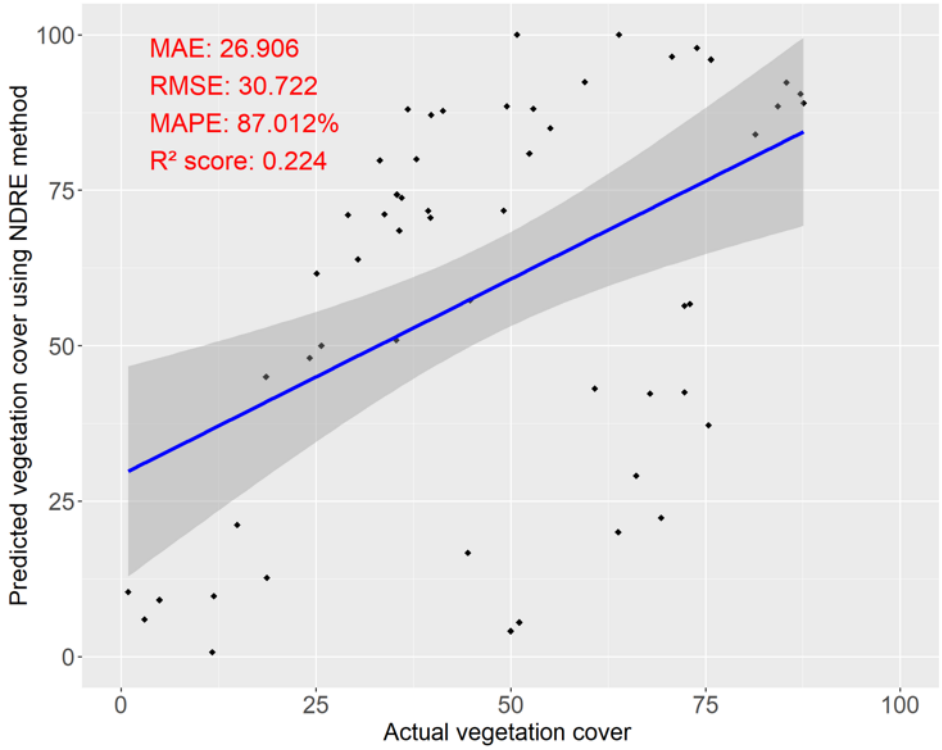

Figure 3-39: Scatterplot for predicted vs actual vegetation cover using best performing NDRE threshold of 25%.

Similarly, the SAVI was calculated to account for soil brightness influences in areas with partial vegetation cover. The SAVI maps were generated in QGIS, and threshold values between 25% and 60% were investigated to identify the most accurate representation of vegetation coverage. An optimal threshold of 40% for SAVI achieved an improved R^2 score of 0.239, *MAE* score of 24.263, *RMSE* of 29.003, and *MAPE* score of 62.787%, indicating enhanced prediction accuracy. Figure 3-40. presents a scatterplot showing the performance of this threshold in predicting vegetation cover versus actual vegetation cover.

Among all VI methods and their respective thresholds, the SAVI method at 40% threshold demonstrated best performance in predicting vegetation cover at construction sites. The performance of this optimal SAVI threshold configuration was subsequently compared with the best-performing DL model, MAnet, through comprehensive statistical analysis, which is presented in the following section.

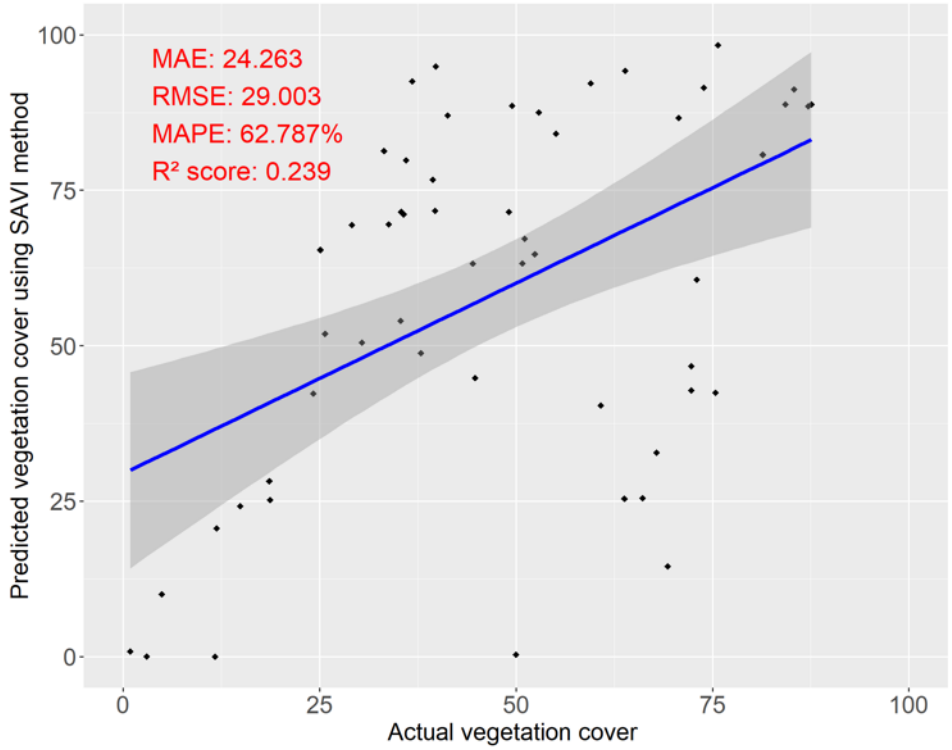

Figure 3-40: Scatterplot for predicted vs actual vegetation cover using best performing SAVI threshold of 40%.

3.3 Performance Assessment: Comparison of Vegetation Detection Using Vegetation Indices and Deep Learning Approaches

A comparative analysis was conducted to assess the performance of the VI-based and DL models in estimating vegetation cover. The best-performing VI method, SAVI with a 40% threshold, was used to estimate vegetation cover on randomly chosen frames across the construction sites which were not used for training the DL models in order to check how well the trained DL model generalized on unseen dataset.

The B-A plot for the VI-based approach revealed a mean difference of 5.220 with a standard deviation of 23.480, and LoA extending from -40.800 to 51.240. The slope of 0.476 with a p-value < 0.05 indicated a presence of significant bias, which is visible from the considerable spread in predictions pointed to variability in estimation accuracy. This was further supported by the scatter plot, which showed an R^2 of 0.491, along with a high *MAE* of 20.830, *RMSE* of 23.473, and a *MAPE* of 59.057%, reflecting moderate alignment with the actual vegetation cover measurements (Figure 3-41).

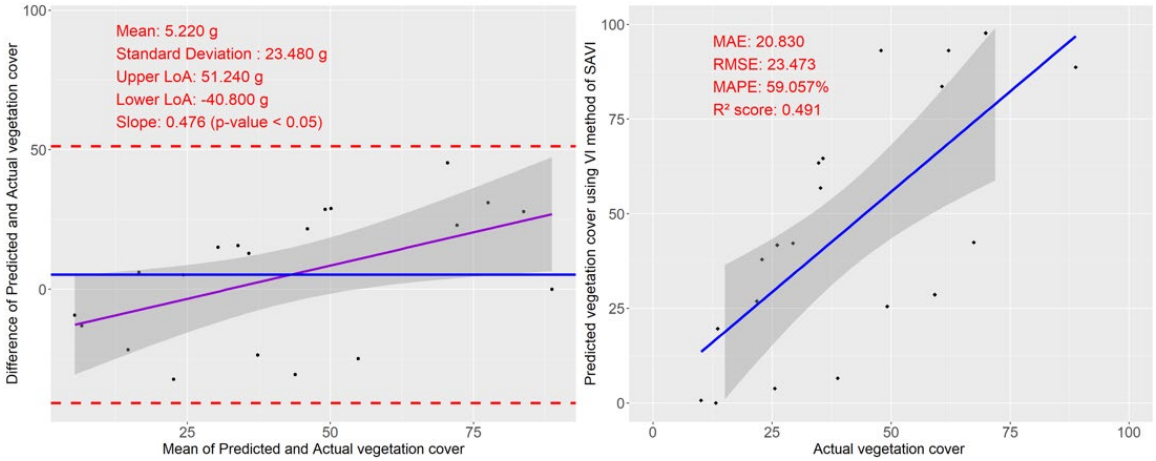

Figure 3-41: (Left) B-A analysis on predicted vegetation cover using best performing VI method of SAVI against actual vegetation cover and (Right) scatterplot for predicted vegetation cover using best performing VI method vs actual vegetation cover.

In contrast, the DL model performed significantly better than the VI-based approach (Figure 3-42). The B-A plot for the DL model revealed a mean difference of only 1.125, with a significantly lower standard deviation of 1.390 and LoA ranging from -1.599 to 3.849. The scatter plot for the DL model indicated a near-perfect fit, with an R^2 of 0.996, an *MAE* of 1.225, *RMSE* of 1.761, and a *MAPE* of 3.003%. These results indicate that the DL model provided an accurate and consistent vegetation cover estimate with minimal prediction errors. The comparison strongly suggests that the DL model outperforms the VI-based approach in estimating vegetation cover, offering a more reliable tool for applications in environmental monitoring and vegetation management.

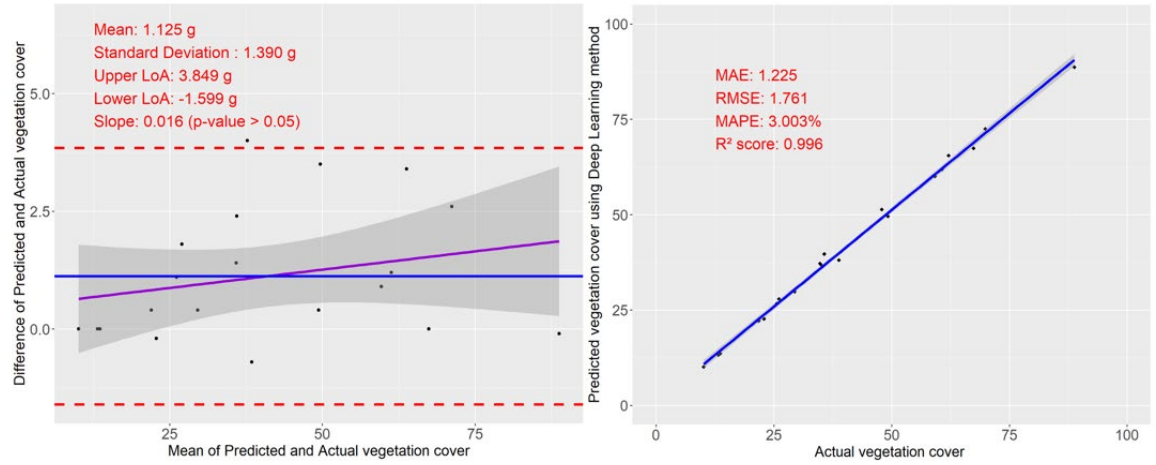

Figure 3-42: (Left) B-A analysis on predicted vegetation cover using best performing DL model against actual vegetation cover and (Right) scatterplot for predicted vegetation cover using best performing VI method vs actual vegetation cover.

Overall, the DL model significantly outperformed the VI-based approach in estimating vegetation cover. The DL model's ability to capture complex patterns and relation-ships within the

data led to more accurate and consistent predictions. These findings suggest that DL models hold great potential for advancing vegetation monitoring and management practices.

3.4 SUMMARY: KEY TAKEAWAYS

3.4.1 Deep Learning Model Performance

- MAnet with mit_b4 backbone achieved the best performance with validation metrics of precision (0.901), recall (0.906), and IoU score (0.869).
- Transformer-based backbones (mit_b4 and mit_b5) demonstrated superior performance compared to ResNet backbones.
- The MAnet model showed excellent generalization capability with a mean IoU of 0.900 on the test dataset, effectively discriminating between different vegetation species.
- The model exhibited some limitations in distinguishing between morphologically similar grass species (Johnson grass, Crabgrass, and Browntop millet), while performing better with visually distinctive species.

3.4.2 Vegetation Indices Analysis

Multiple threshold values were tested to optimize vegetation detection for each index. The optimal thresholds were: NDVI (50%), NDRE (25%), and SAVI (40%). SAVI at 40% threshold was the best-performing vegetation index method with R^2 of 0.239, RMSE of 29.003, and MAPE of 62.787%.

3.4.3 Comparative Performance Assessment

The DL approach significantly outperformed vegetation indices methods:

1. DL model: R^2 of 0.996, MAE of 1.225, RMSE of 1.761, and MAPE of 3.003%.
2. Best VI method (SAVI): R^2 of 0.491, MAE of 20.830, RMSE of 23.473, and MAPE of 59.057%.
3. Bland-Altman analysis showed the DL model had minimal bias (mean difference of 1.125) and narrow limits of agreement (-1.599 to 3.849), indicating high consistency and reliability.
4. VI-based methods showed considerable bias (mean difference of 5.220) and wide limits of agreement (-40.800 to 51.240), indicating greater variability in estimation accuracy.

Importance: The findings demonstrate the superior capability of DL approaches over traditional VI-based methosa for vegetation composition assessment tasks. The performance of the MAnet model, suggests a significant advancement in automated vegetation monitoring

techniques. The comparative analysis provides clear evidence that AI-driven methods can achieve near-perfect vegetation cover estimates, offering substantial improvements in accuracy, consistency, and reliability for environmental monitoring applications. These findings are particularly relevant for transportation infrastructure management, construction site stabilization assessment, and environmental compliance monitoring tasks.

Chapter 4
DISCUSSION

Gaining insights into the composition of roadside vegetation is essential for under-standing species distribution and ecological roles, enabling timely management interventions to control growth and protect native biodiversity. This knowledge is vital for making informed decisions in sustainable land use and environmental planning. Remote sensing technologies, combined with DL models, offer powerful tools to efficiently monitor, analyze, and map vegetation composition over large areas effectively. SS-based DL algorithms perform detailed pixel-level classification, allowing for more accurate and nuanced analysis of vegetation species and distributions. The DL models developed in this study, especially MAnet with a transformer-based backbone, showed excellent accuracy, achieving an R^2 score of 0.996 for vegetation cover prediction, along with a mean IoU score of 0.90, indicating strong generalization for composition assessment tasks. This pixel-level classification capability supports its practical utility in real-world applications like vegetation monitoring on construction sites and biodiversity conservation in similar environments. While the model demonstrated robust performance in distinguishing most vegetation species, it exhibited some limitations in differentiating between morphologically similar grass species. In particular, instances of misclassification were observed among visually similar species such as Johnson grass, Crabgrass, and Browntop millet due to their com-parable physical characteristics. These findings align with similar challenges reported by [5], where comparable misclassification patterns were observed when using XGBoost models on UAV-captured RGB imagery at 70 meters altitude for grass species detection. This consistent pattern across different methodologies suggests that the challenge of distinguishing between visually similar grass species remains a fundamental limitation in remote sensing-based vegetation classification. Our findings align with those of [41], who used UAV imagery and semantic segmentation models, including ResNet, to detect invasive grassland species, achieving a mean IoU of 85%. While comparable in accuracy, our MAnet model outperformed in generalization, attaining a higher IoU score of 0.90. Both studies underscore the effectiveness of DL models in detailed vegetation mapping and monitoring, highlighting the potential use in environmental management and conservation applications. Nevertheless, our model’s overall strong performance in detailed vegetation mapping, especially amongst a higher number of grass species with distinct features, underscores its potential as a valuable tool for vegetation monitoring and management applications.

VIs such as NDVI, NDRE, and SAVI are widely used for assessing vegetation health, the DL models in this study significantly outperformed these methods, achieving re-markable accuracy with an R^2 score of 0.996 and a *MAPE* of just 3.003% in vegetation detection tasks. The DL model's superior performance, demonstrated by higher R^2 and lower *RMSE* and *MAPE*

scores, underscores its effectiveness in capturing the complexity of vegetation patterns, where traditional VI methods may lack precision due to limitations in spatial or spectral resolution. Notably, these exceptional results were achieved using proximal RGB imagery compared to multispectral imagery, suggesting that even higher accuracy could be attained by employing higher spectral quality and resolution cameras at similar heights for vegetation composition analysis tasks. Our results present a notable contrast to [27] research, where they employed support vector machine classifiers on data collected at 120 meters altitude and concluded that multispectral imagery yielded superior vegetation classification results compared to RGB imagery. In our study, the DL model's performance on RGB imagery (R^2 = 0.996, *RMSE* of 1.761, *MAPE* = 3.003%) significantly surpassed the results obtained from multispectral imagery-based methods (R^2 = 0.490, *MAPE* = 59.060%). These findings not only align with previous studies highlighting the enhanced capability of DL models in robust vegetation assessment tasks [1, 26] but also suggest that the combination of high-resolution imagery and advanced DL techniques may offer a more effective approach for detailed vegetation analysis. This study supports the growing use of high-resolution RGB imagery and ML techniques for vegetation monitoring, as seen in [20], who used over 90,000 drone tiles and satellite data with a random forest model to estimate grassland canopy cover (R^2 = 0.89) in a binary classification setup. In contrast, our DL-based SS approach using MAnet achieved a higher R^2 and a lower *MAPE* value, enabling detailed classification across eight grass species. Similarly, compared to [17], who assessed 30 UAV-based methods for turfgrass cover estimation—achieving up to R^2 = 0.960 with RGB-based GPI and SVM, our DL model provided superior accuracy and species-level segmentation, highlighting its greater potential for applications like invasive species control and biodiversity monitoring. This multi-class, pixel-level capability offers enhanced ecological insights for roadside and construction zone management.

[22] used RGB segmentation and climate features for binary clover-grass analysis, our DL approach enables accurate multi-species classification and cover estimation without manual feature engineering. While their method achieved a frequency-weighted IOU score of 0.39, our MAnet model achieved a mean IoU score of 0.90, demonstrating enhanced precision and scalability of semantic segmentation for detailed roadside vegetation composition analysis. While [42] used multi-source satellite and DEM data with a FCN-ResNet model to classify four mountain vegetation types (85.8% accuracy), our RGB-only UAV-based approach achieved higher accuracy (mIoU = 0.90), proving more efficient for dynamic environments like construction zones. Similarly, [28] found an R^2 of 0.82 between drone and field vegetation estimates but noted reduced accuracy in diverse, low-cover areas. In contrast, our DL model achieved R^2 = 0.996 with reliable multi-species classification, offering a more robust solution for variable roadside vegetation analysis. [43] used Canopeo for binary green cover estimation with good correlation (r = 0.91) with traditional image analysis in untreated turf. However, their method was limited to

green cover estimation and was affected by colorant treatments. In contrast, our DL-based approach achieves species-level classification and cover quantification with higher accuracy scores, providing a more robust and scalable solution for dynamic roadside environments. [8] evaluated thirty SS models using synthetic and real RGB images for estimating clover, grass, and weed ratios, with a top mIoU of 62.3%. In comparison, our MAnet model, trained on real pixel-annotated RGB data, achieved a higher mIoU and enabled species-level roadside vegetation classification, demonstrating better performance. Similarly, [32] fused single-class SegNet models with UAV RGB imagery and texture features to classify karst wetland vegetation, achieving up to 0.97 F1-score. Our study achieves com-parable accuracy (mIoU = 0.90) using a MAnet model without auxiliary data, offering a more streamlined and scalable approach. While their evaluation focused on Precision, Recall, and F1-score, they did not report mean IoU metric score—a key metric for SS that our study includes to provide deeper insight into DL model performance.

4.1 LIMITATIONS

Although this study highlights the potential of DL for precise vegetation mapping, several limitations must be addressed to further enhance the framework's effectiveness and applicability. The current dataset, while substantial, lacks the diversity needed for the model to generalize across a wider range of vegetation species, soil types across diverse environmental conditions. Expanding the dataset to include more varied plant communities, geographic regions, and ecological contexts would improve model robustness, enabling it to provide more consistent and comprehensive vegetation assessments for applications in agriculture, forestry, and ecological restoration. Another important area for future development is the implementation of a real-time monitoring system. Integrating UAVs for automated data collection with immediate, on-site analysis could support rapid, data-informed decisions on vegetation health and coverage, especially in rapidly changing environments. By addressing these limitations and pursuing these future directions, the framework's versatility, accuracy, and practical utility could be significantly strengthened, ultimately supporting more data-driven decision-making for sustainable land use, biodiversity conservation, and ecological restoration across diverse ecosystems.

4.2 FUTURE WORK

A promising avenue for future work is the development of a smartphone application and a user-friendly website that deploy the trained DL models for vegetation detection and analysis tasks. These platforms would enable end-users to directly leverage the advanced capabilities of the research models, bridging the gap between academic study and practical application. A mobile application could allow users to capture images of specific areas and receive instant predictions on vegetation type, health, and coverage. This would be particularly valuable for users in the

fields of roadside vegetation monitoring , agriculture, and land management, who could benefit from real-time, in-situ vegetation assessment. Similarly, a web-based platform could support larger-scale analysis by enabling users to upload data or access existing imagery for detailed, comprehensive vegetation composition analysis across broader regions. By providing accessible, user-friendly tools, these platforms would make advanced vegetation detection and analysis techniques more widely available and actionable. This would facilitate more efficient, data-driven decision-making in areas such as sustainable land use, biodiversity conservation, and precision agriculture. Ultimately, the development of these applied platforms would extend the impact of the research, empowering a diverse range of stakeholders to actively monitor and manage vegetation dynamics in their respective domains.

4.3 Technological Advancements Required for Effective Vegetation Identification by ALDOT

The performance outcomes detailed in Chapter 3 highlight significant implications for ALDOT's approach to vegetation inspections and construction site stabilization management. The enhanced accuracy and reliability provided by the DL framework—especially in measuring vegetative cover density—present a paradigm shift in erosion and sediment control processes. By addressing persistent challenges associated with visual evaluations and index-based estimates, this system offers pixel-level precision and scalability for both vegetation density analysis and species identification. This capability allows field teams to accurately verify coverage thresholds and pinpoint areas needing re-seeding, monitoring for invasive species, or correcting uneven vegetation establishment—tasks that are often prone to error when using traditional methods.

Beyond accuracy improvements, the DL-based approach also offers practical benefits. It minimizes subjectivity during inspections, shortens the time required for on-site evaluations, and facilitates quick data processing. To effectively implement this system, ALDOT will need to invest strategically. This may include providing inspection crews with UAVs equipped with high-resolution RGB cameras and access to cloud-based processing for real-time inference, along with user-friendly interfaces for overlay visualization of vegetative coverage. Additionally, to maintain long-term efficiency, periodic updates to the model will be necessary, incorporating seasonal data and expanding to recognize new or invasive plant species. Implementing this technology could also enable trend monitoring over project timelines, delivering predictive insights into vegetation establishment and supporting proactive site management. This would transform the system from a compliance tool to an integral component of sustainable construction practices.

Figure 4-1 demonstrates the end-to-end process for vegetation assessment tasks using the DL approach. The sequence begins with UAV-captured aerial imagery (top-left) that provides an overall view of the site. Field technicians can define specific sampling zones using physical quadrats (visible as white square frames labeled with "8" in the top-right panel). The high-

resolution imagery collected by UAV-mounted cameras ensures sufficient detail for accurate analysis, as evidenced in the sampling area. After processing these defined regions through the trained DL model, the system generates detailed classification outputs (bottom-right panel) that use color-coded visualization to represent different vegetation types and their coverage density, respectively. This integrated workflow allows ALDOT inspectors to conduct quantitative, reproducible assessments without subjective interpretation, significantly enhancing field evaluation efficiency.

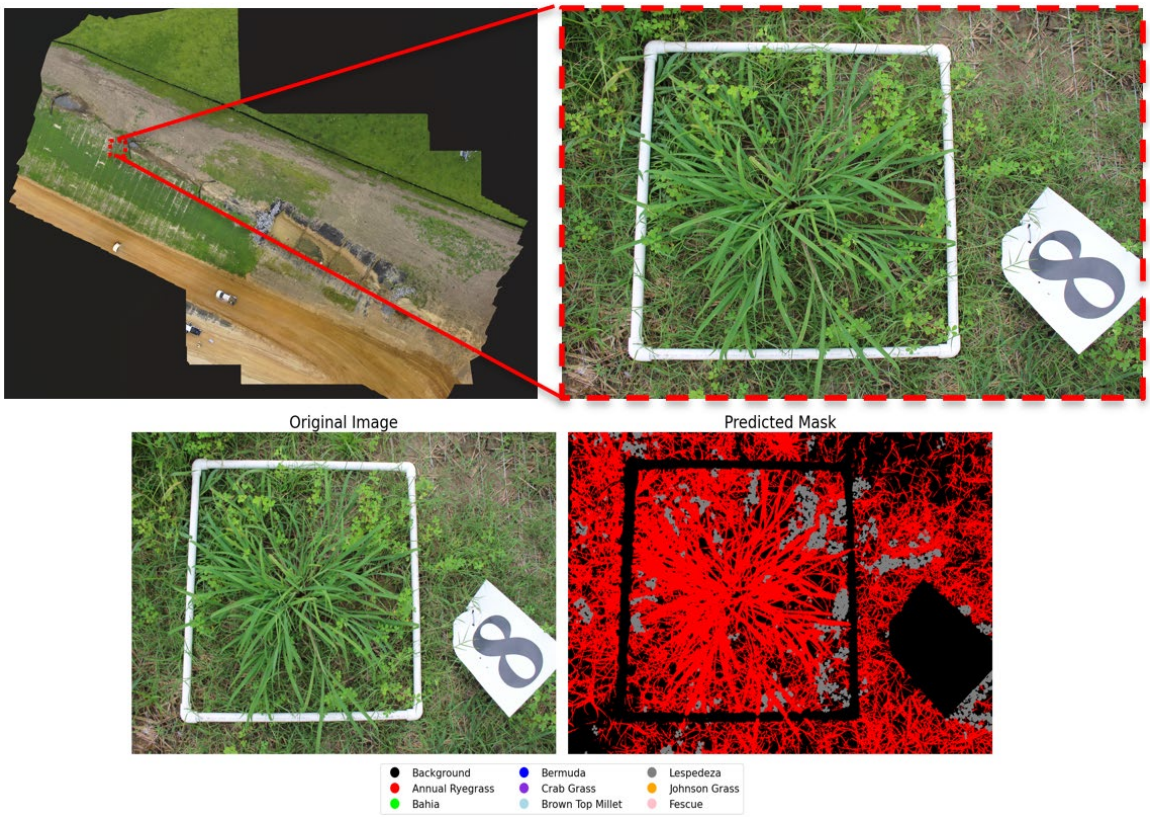

Figure 4-1: (Top-Left) Aerial imagery captured at Linden construction site, (Top-Right and Bottom-Left) High resolution proximal imagery of quadrats 8 laid at the site during data collection, (Bottom-Right) Classification result generated by DL model on the RGB imagery.

Chapter 5
CONCLUSION

Vegetation composition assessment at roadside construction sites is an important task as it provides essential insights in maintaining ecological stability, controlling invasive species, and ensuring compliance with environmental regulations. Our research demonstrates an approach for detailed vegetation analysis, with a specific focus on predicting vegetation cover and assessing species composition at construction sites. This study conducts a comparative evaluation of vegetation composition analysis using DL techniques against conventional VIs derived from multispectral imagery, highlighting the enhanced accuracy and robustness offered by DL-based methods. High-resolution proximal RGB imagery was employed to train and evaluate several DL models for classifying vegetation cover and species composition among various grass types. Among the tested models, MAnet integrated with the mit_b4 backbone delivered exceptional results, achieving high IoU scores. This underscores its strong capability in accurately differentiating vegetation species and generalizing effectively to new, unseen datasets. Its success is attributed to the incorporation of attention mechanisms and advanced feature extraction, which proved particularly effective in managing complex roadside vegetation environments, including the separation of visually similar species. While conventional VIs like NDVI, NDRE, and SAVI provided valuable insights into vegetation health and density, they exhibited greater variability in performing the tasks of predicting area under vegetation cover in comparison to the DL models. This was evident in the B-A and scatter plot analyses, which revealed a significant spread in the VI-based predictions and a moderate correlation with ground truth data. Overall, this research concludes and discusses the advantages of DL-based SS over traditional VI methods. The findings underscore the practicality of integrating DL models in real-world applications, such as monitoring vegetation on construction sites, managing invasive species, and supporting ecological conservation efforts. This study provides a valuable tool for sustainable land management, demonstrating that modern computational approaches involving SS-based DL techniques can offer more accurate and actionable insights into vegetation dynamics, ultimately aiding in responsible environmental management.

REFERENCES

1. Ayhan, B., Kwan, C., Budavari, B., Kwan, L., Lu, Y., Perez, D., Li, J., Skarlatos, D., & Vlachos, M. (2020). Vegetation detection using deep learning and conventional methods. Remote Sensing, 12(15). https://doi.org/10.3390/RS12152502
2. Lynch, T. M., Barth, S., Dix, P. J., Grogan, D., Grant, J., & Grant, O. M. (2015). Ground cover assessment of perennial ryegrass using digital imaging. Agronomy Journal, 107(6), 2347-2352. https://doi.org/10.2134/agronj15.0185
3. Rentch, J. S., Fortney, R. H., Stephenson, S. L., Adams, H. S., Grafton, W. N., & Anderson, J. T. (2005). Vegetation–site rela-tionships of roadside plant communities in West Virginia, USA. Journal of Applied Ecology, 42(1), 129-138. https://doi.org/10.1111/j.1365-2664.2004.00993.x
4. Jakobsson, S., Bernes, C., Bullock, J. M., Verheyen, K., & Lindborg, R. (2018). How does roadside vegetation management affect the diversity of vascular plants and invertebrates? A systematic review. Environmental Evidence, 7, 1-14. https://doi.org/10.1186/s13750-018-0129-z
5. Sandino, J., Gonzalez, F., Mengersen, K., & Gaston, K. J. (2018). UAVs and machine learni evolutionizinging invasive grass and vegetation surveys in remote arid lands. Sensors, 18(2), 605. https://doi.org/10.3390/s18020605
6. Weidlich, E. W., Flórido, F. G., Sorrini, T. B., & Brancalion, P. H. (2020). Controlling invasive plant species in ecological res-toration: A global review. Journal of Applied Ecology, 57(9), 1806-1817. https://doi.org/10.1111/1365-2664.136567.
7. Milton, S. J., Dean, W. R. J., Sielecki, L. E., & van der Ree, R. (2015). The function and management of roadside vegetation. Handbook of road ecology, 373-381. https://doi.org/10.1002/9781118568170.ch46
8. Kartal, S. (2021). Comparison of semantic segmentation algorithms for the estimation of botanical composition of clover-grass pastures from RGB images. Ecological Informatics, 66, 101467. https://doi.org/10.1016/j.ecoinf.2021.101467
9. Pettorelli, N., Schulte to Bühne, H., Tulloch, A., Dubois, G., Macinnis-Ng, C., Queirós, A. M., ... & Nicholson, E. (2018). Satellite remote sensing of ecosystem functions: opportunities, challenges and way forward. Remote Sensing in Ecology and Conservation, 4(2), 71-93. https://doi.org/10.1002/rse2.59
10. Perez, M. A., Zech, W. C., & Donald, W. N. (2015). Using unmanned aerial vehicles to conduct site inspections of erosion and sediment control practices and track project progression. Transportation Research Record, 2528(1), 38-48. https://doi.org/10.3141/2528-051
11. Xie, Y., Sha, Z., & Yu, M. (2008). Remote sensing imagery in vegetation mapping: a review. Journal of plant ecology, 1(1), 9-23. https://doi.org/10.1093/jpe/rtm005
12. Getzin, S., Wiegand, K., & Schöning, I. (2012). Assessing biodiversity in forests using very high-resolution images and un-manned aerial vehicles. Methods in ecology and evolution, 3(2), 397-404. https://doi.org/10.1111/j.2041-210X.2011.00158.x
13. Zhu, Z., Qiu, S., & Ye, S. (2022). Remote sensing of land change: A multifaceted perspective. Remote Sensing of Environment, 282, 113266. https://doi.org/10.1016/j.rse.2022.113266
14. Xue, J., & Su, B. (2017). Significant remote sensing vegetation indices: A review of developments and applications. Journal of sensors, 2017(1), 1353691. https://doi.org/10.1155/2017/1353691

15. Al-Ali, Z. M., Abdullah, M. M., Asadalla, N. B., & Gholoum, M. (2020). A comparative study of remote sensing classification methods for monitoring and assessing desert vegetation using a UAV-based multispectral sensor. Environmental monitoring and assessment, 192(6), 389. https://doi.org/10.1007/s10661-020-08330-1
16. Lee, G., Hwang, J., & Cho, S. (2021). A novel index to detect vegetation in urban areas using UAV-based multispectral images. Applied sciences, 11(8), 3472. https://doi.org/10.3390/app11083472
17. Wang, T., Chandra, A., Jung, J., & Chang, A. (2022). UAV remote sensing-based estimation of green cover during turfgrass establishment. Computers and Electronics in Agriculture, 194, 106721. https://doi.org/10.1016/j.compag.2022.106721
18. Kim, J., Kang, S., Seo, B., Narantsetseg, A., & Han, Y. (2020). Estimating fractional green vegetation cover of Mongolian grasslands using digital camera images and MODIS satellite vegetation indices. GIScience & Remote Sensing, 57(1), 49-59. https://doi.org/10.1080/15481603.2019.1662166
19. Zhu, X. X., Tuia, D., Mou, L., Xia, G. S., Zhang, L., Xu, F., & Fraundorfer, F. (2017). Deep learning in remote sensing: A com-prehensive review and list of resources. IEEE geoscience and remote sensing magazine, 5(4), 8-36. https://doi.org/10.1109/MGRS.2017.2762307
20. Hu, T., Cao, M., Zhao, X., Liu, X., Liu, Z., Liu, L., … & Su, Y. (2024). High-resolution mapping of grassland canopy cover in China through the integration of extensive drone imagery and satellite data. ISPRS Journal of Photogrammetry and Remote Sensing, 218, 69-83. https://doi.org/10.1016/j.isprsjprs.2024.09.004
21. Dong, S., Wang, P., & Abbas, K. (2021). A survey on deep learning and its applications. Computer Science Review, 40, 100379. https://doi.org/10.1016/j.cosrev.2021.100379
22. Mortensen, A. K., Karstoft, H., Søegaard, K., Gislum, R., & Jørgensen, R. N. (2017). Preliminary results of clover and grass coverage and total dry matter estimation in clover-grass crops using image analysis. Journal of Imaging, 3(4), 59. https://doi.org/10.3390/jimaging3040059
23. Kamilaris, A., & Prenafeta-Boldú, F. X. (2018). Deep learning in agriculture: A survey. Computers and electronics in agri-culture, 147, 70-90. https://doi.org/10.1016/j.compag.2018.02.016
24. Jin, X., Bagavathiannan, M., McCullough, P. E., Chen, Y., & Yu, J. (2022). A deep learning-based method for classification, detection, and localization of weeds in turfgrass. Pest Management Science, 78(11), 4809-4821. https://doi.org/10.1002/ps.7102
25. Luo, Z., Yang, W., Yuan, Y., Gou, R., & Li, X. (2023). Semantic segmentation of agricultural images: A survey. Information Processing in Agriculture. https://doi.org/10.1016/j.inpa.2023.02.001
26. Behera, T. K., Bakshi, S., & Sa, P. K. (2022). Vegetation extraction from UAV-based aerial images through deep learning. Computers and Electronics in Agriculture, 198, 107094. https://doi.org/10.1016/j.compag.2022.107094
27. Furukawa, F., Laneng, L. A., Ando, H., Yoshimura, N., Kaneko, M., & Morimoto, J. (2021). Comparison of RGB and multi-spectral unmanned aerial vehicle for monitoring vegetation coverage changes on a landslide area. Drones, 5(3), 97. https://doi.org/10.3390/drones5030097
28. Pérez-Luque, A. J., Ramos-Font, M. E., Tognetti Barbieri, M. J., Tarragona Pérez, C., Calvo Renta, G., & Robles Cruz, A. B. (2022). Vegetation cover estimation in semi-arid shrublands after prescribed burning: field-ground and drone image comparison. Drones, 6(11), 370. https://doi.org/10.3390/drones6110370

29. Himstedt, M., Fricke, T., & Wachendorf, M. (2012). The benefit of color information in digital image analysis for the estimation of legume contribution in legume–grass mixtures. Crop Science, 52(2), 943-950. https://doi.org/10.2135/cropsci2011.04.0189
30. Singh, P. (2022) Semantic Segmentation based deep learning approaches for weed detection. Master's Thesis, University of Nebraska-Lincoln, Lincoln, NE, USA, 16 December 2022. https://digitalcommons.unl.edu/biosysengdiss/137/
31. Yu, J., Schumann, A. W., Cao, Z., Sharpe, S. M., & Boyd, N. S. (2019). Weed detection in perennial ryegrass with deep learning convolutional neural network. Frontiers in plant science, 10, 1422. https://doi.org/10.3389/fpls.2019.01422
32. Deng, T., Fu, B., Liu, M., He, H., Fan, D., Lil., … & Gao, E. (2022). Comparison of multi-class and fusion of multiple single-class SegNet model for mapping karst wetland vegetation using UAV images. Scientific reports, 12(1), 13270. https://doi.org/10.1038/s41598-022-17620-2
33. Brooks, J., 2019. COCO Annotator. Retrieved from https://github.com/jsbroks/coco-annotator (accessed on 16 April 2025)
34. Bradski, G. (2000). The opencv library. Dr' Dobb's Journal: Software Tools for the Professional Programmer, 25(11), 120-123.
35. Z. Zhou, M. M. R. Siddiquee, N. Tajbakhsh and J. Liang, "UNet++: Redesigning Skip Connections to Exploit Multiscale Features in Image Segmentation," in IEEE Transactions on Medical Imaging, vol. 39, no. 6, pp. 1856-1867, June 2020, https://doi.org/10.1109/TMI.2019.2959609
36. Zhao, H., Shi, J., Qi, X., Wang, X., & Jia, J. (2017). Pyramid scene parsing network. Proceedings of the IEEE Conference on Computer Vision and Pattern Recognition, 2881-2890. https://doi.org/10.48550/arXiv.1612.01105
37. Li, R., Zheng, S., Zhang, C., Duan, C., Su, J., Wang, L., & Atkinson, P. M. (2021). Multiattention network for semantic seg-mentation of fine-resolution remote sensing images. IEEE Transactions on Geoscience and Remote Sensing, 60, 1-13. https://doi.org/10.1109/TGRS.2021.3093977
38. Chen, L. C., Zhu, Y., Papandreou, G., Schroff, F., & Adam, H. (2018). Encoder-decoder with atrous separable convolution for semantic image segmentation. Proceedings of the E10. https://doi.org/10.48550/arXiv.1802.02611
39. Lin, T. Y., Goyal, P., Girshick, R., He, K., & Dollár, P. (2017). Focal loss for dense object detection. Proceedings of the IEEE international conference on computer vision, 2980-2988. https://doi.org/10.48550/arXiv.1708.02002
40. Giavarina, D. (2015). Understanding bland altman analysis. Biochemia medica, 25(2), 141-151. https://doi.org/10.11613/BM.2015.015
41. Wang, L., Zhou, Y., Hu, Q., Tang, Z., Ge, Y., Smith, A., ... & Shi, Y. (2021). Early detection of encroaching woody juniperus virginiana and its classification in multi-species forest using UAS imagery and semantic segmentation algorithms. Remote Sensing, 13(10), 1975. https://doi.org/10.3390/rs13101975
42. Wang, B., & Yao, Y. (2024). Mountain vegetation classification method based on multi-channel semantic segmentation model. Remote Sensing, 16(2), 256. https://doi.org/10.3390/rs16020256
43. Chhetri, M., & Fontanier, C. (2021). Use of canopeo for estimating green coverage of bermudagrass during postdormancy regrowth. HortTechnology, 31(6), 817-819. https://doi.org/10.21273/HORTTECH04938-21

APPENDIX

ABBREVIATIONS

The following abbreviations are used in this report:

SS	Semantic Segmentation
VIs	Vegetation Indices
DL	Deep Learning
ML	Machine Learning
UAV	Unmanned Aerial Vehicles
NIR	Near Infra-Red
B-A	Bland Altman
AGL	Above Ground Level
GSD	Ground Sampling Distance
IoU	Intersection over Union
NDVI	Normalized Difference Vegetation Index
NDRE	Normalized Difference Red Edge
SAVI	Soil Adjusted Vegetation Index
MAE	Mean Absolute Error
RMSE	Root Mean Squared Error
MAPE	Mean Absolute Percentage Error
B-A	Bland Altman
R^2	Coefficient of Determination
LoA	Limit of Agreement
MiT	Mix Vision Transformer

A.1 FINE TUNING ANNOTATIONS

Figure A-1. illustrates the pixel percentage distribution for different grass species in the fine-tuned annotations dataset. As noted earlier, the annotations were refined to im-prove accuracy, which resulted in a noticeable shift in the pixel percentage shares of various species. In the original masks, the background accounted for 34% of the pixels, while other vegetation classes like Johnson grass, Browntop millet, Lespedeza, and Crabgrass each contributed significant portions. However, after fine-tuning, the back-ground percentage increased to 59%, indicating that many pixels previously misclassified as vegetation were re-labeled as background. This refinement

process reduced the pro-portion of pixels labeled as certain vegetation types, such as Johnson grass, Browntop millet, Lespedeza, and Annual ryegrass, reflecting a more accurate representation of the true vegetation cover. The reduction in vegetation class percentages, as seen in the fi-ne-tuned annotations, suggests that the revised annotations now more precisely capture only the true areas of vegetation within the frames, minimizing the inclusion of back-ground pixels. This fine-tuning is expected to improve the performance of the DL models by providing cleaner, more accurate data for training.

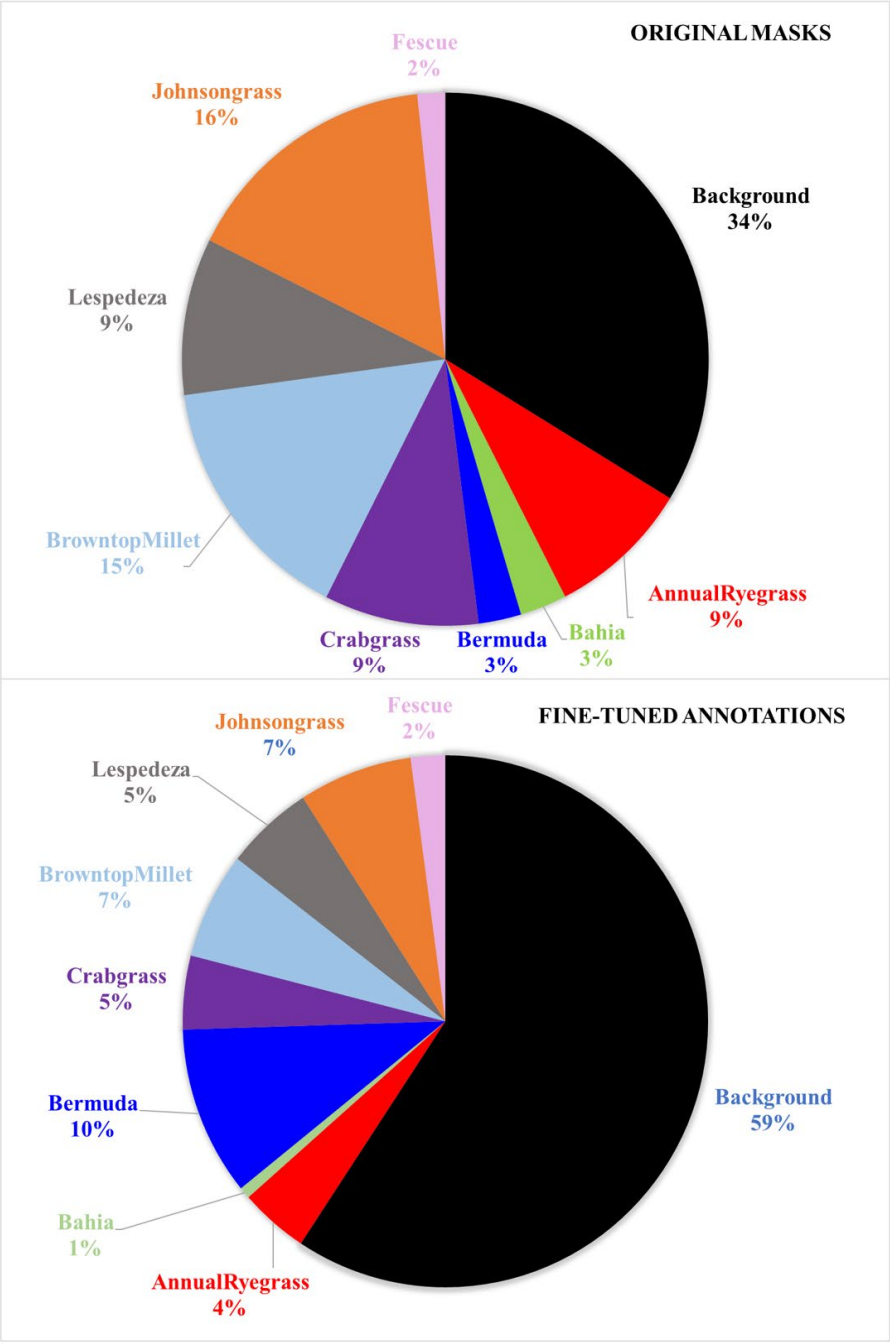

Figure A-1: Pixel percentage share of different grass before (Top) and after (Bottom) fi-ne-tuning the annotation masks.

A.2 CONFUSION MATRICES FOR DEEP LEARNING MODELS

The confusion matrix for the UNet++ model (Figure A-2) with ResNet50 backbone shows its pixel-wise performance across different vegetation classes with a mean IoU score of 0.771. High true positive rates are observed for classes like Crabgrass (0.83) and Lespedeza (0.80), indicating effective classification in these categories. The background class also has a high accuracy of 0.89, highlighting the model's ability to differentiate vegetation from non-vegetation areas. However, lower true positive rates in classes like Browntop millet (0.70) suggest areas where the model struggles, possibly due to visual similarities with other classes.

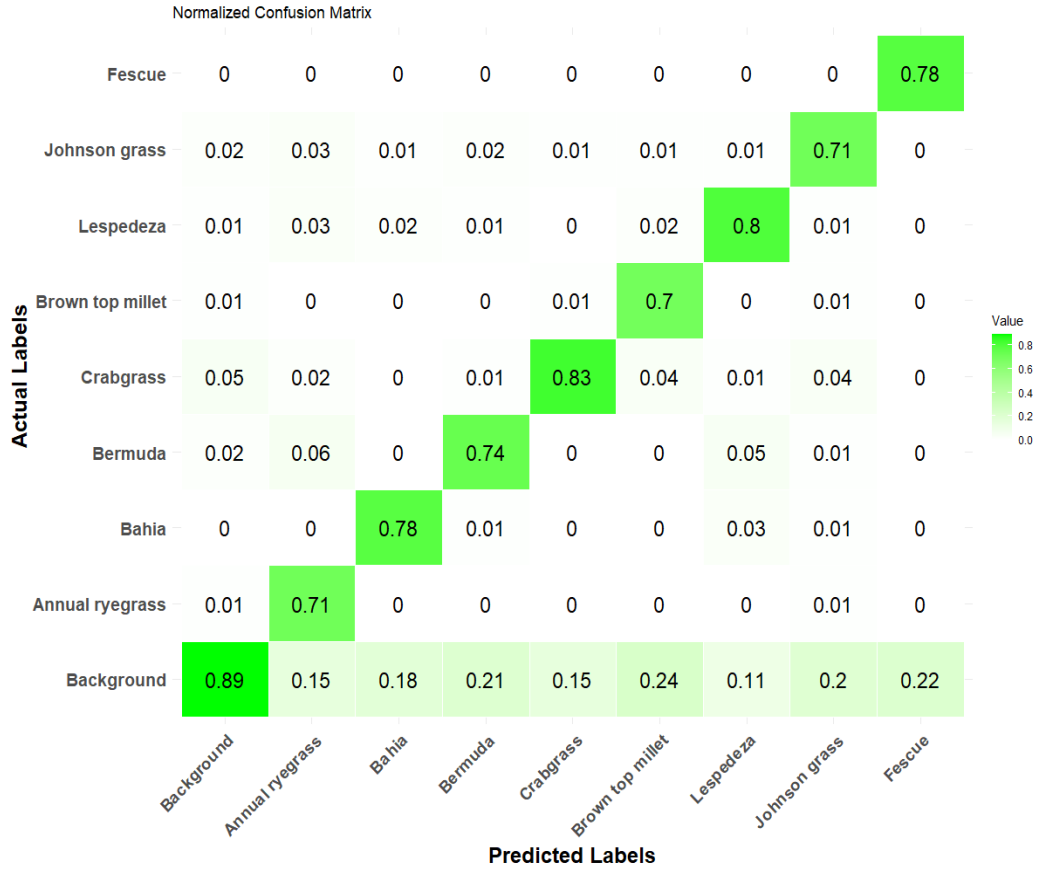

Figure A-2. Confusion matrix for UNet++ model with ResNet50 architecture backbone.

The confusion matrix for the PSPNet model (Figure A-3) with the mit_b5 backbone demonstrates its performance in pixel-wise classification for various vegetation types achieving a mean IoU score of 0.878. High true positive rates are noted for classes such as Bermuda (0.96) and Annual ryegrass (0.93), indicating strong accuracy in detecting these vegetation types. The background class also shows high accuracy (0.95), which is crucial for accurately distinguishing

vegetation areas from non-vegetation. However, the model struggles more with classes like Lespedeza (0.85) and Crabgrass (0.75), suggesting some misclassification in these categories.

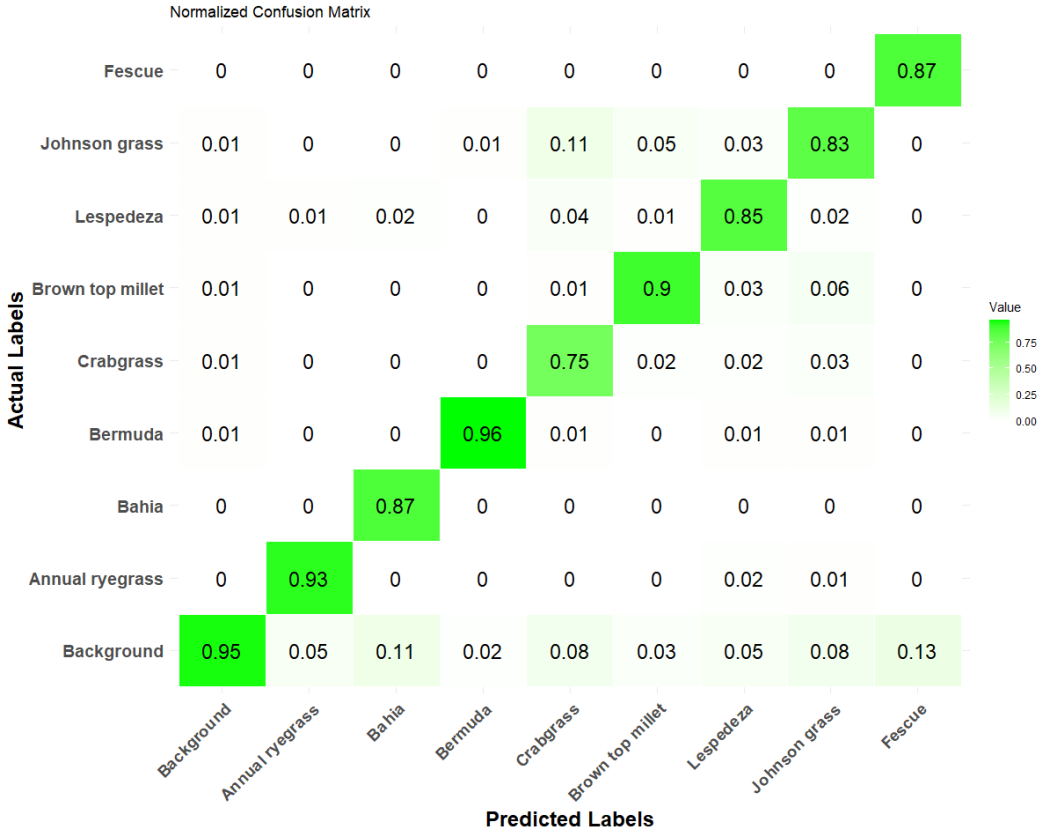

Figure A-3: Confusion matrix for PSPNet model with mit_b5 architecture backbone.

The confusion matrix for the DeepLabV3+ model (Figure A-4) with the ResNet101 backbone shows strong performance in pixel-wise classification across various vegetation types with a mean IoU score of 0.894. High true positive rates are observed for classes like Bermuda (0.96) and Bahia (0.94), indicating effective identification of these vegetation categories. The background class also achieves a high accuracy of 0.95, crucial for separating vegetation from non-vegetation areas. However, classes like Crabgrass (0.75) and Johnson grass (0.87) show slightly lower accuracy, suggesting areas where the model may have some misclassifications. Overall, the diagonal values demonstrate the model's ability to accurately detect most classes, reflecting good generalization on the testing dataset.

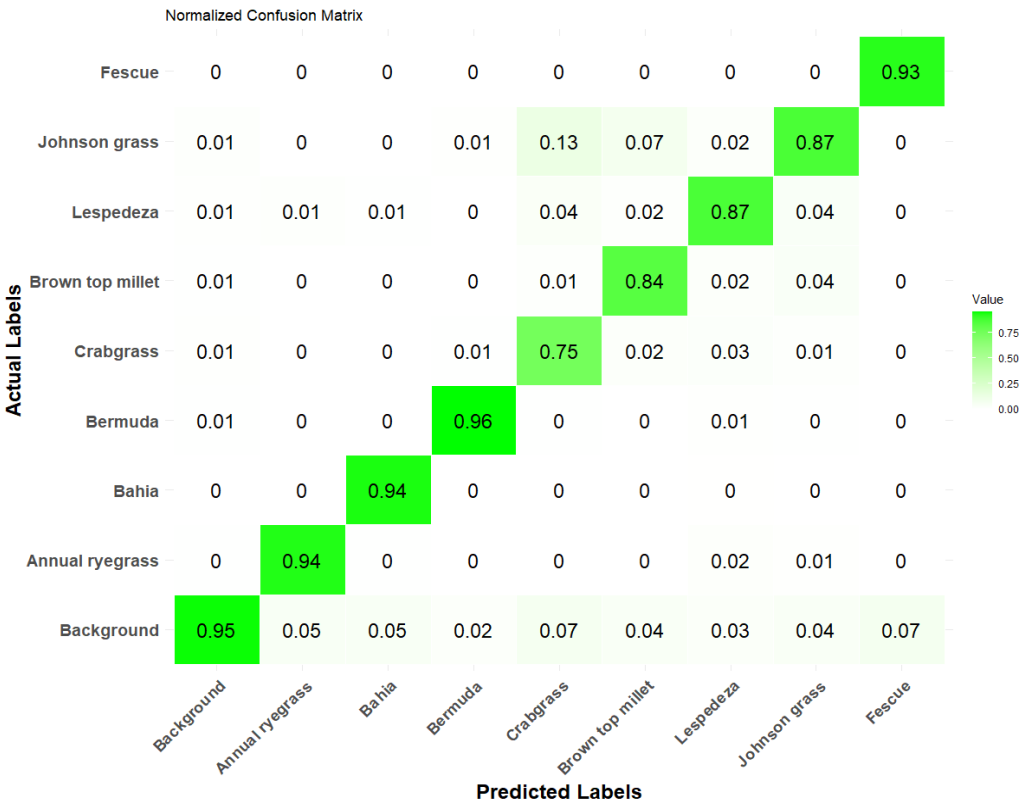

Figure A-4. Confusion matrix for DeepLabV3+ model with ResNet101 architecture backbone.

A.3 PERFORMANCE OF BEST-PERFORMING MANET DL MODEL

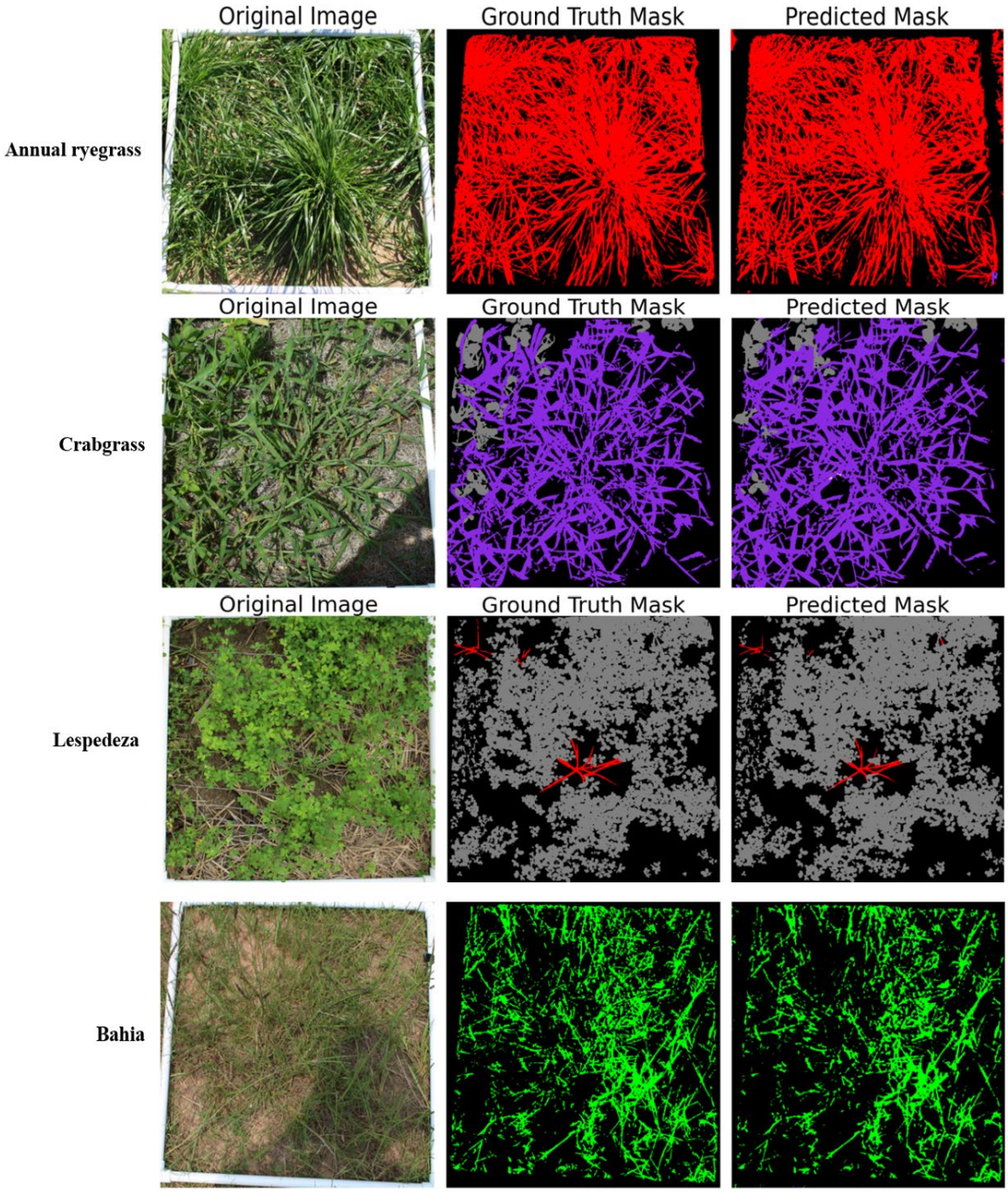

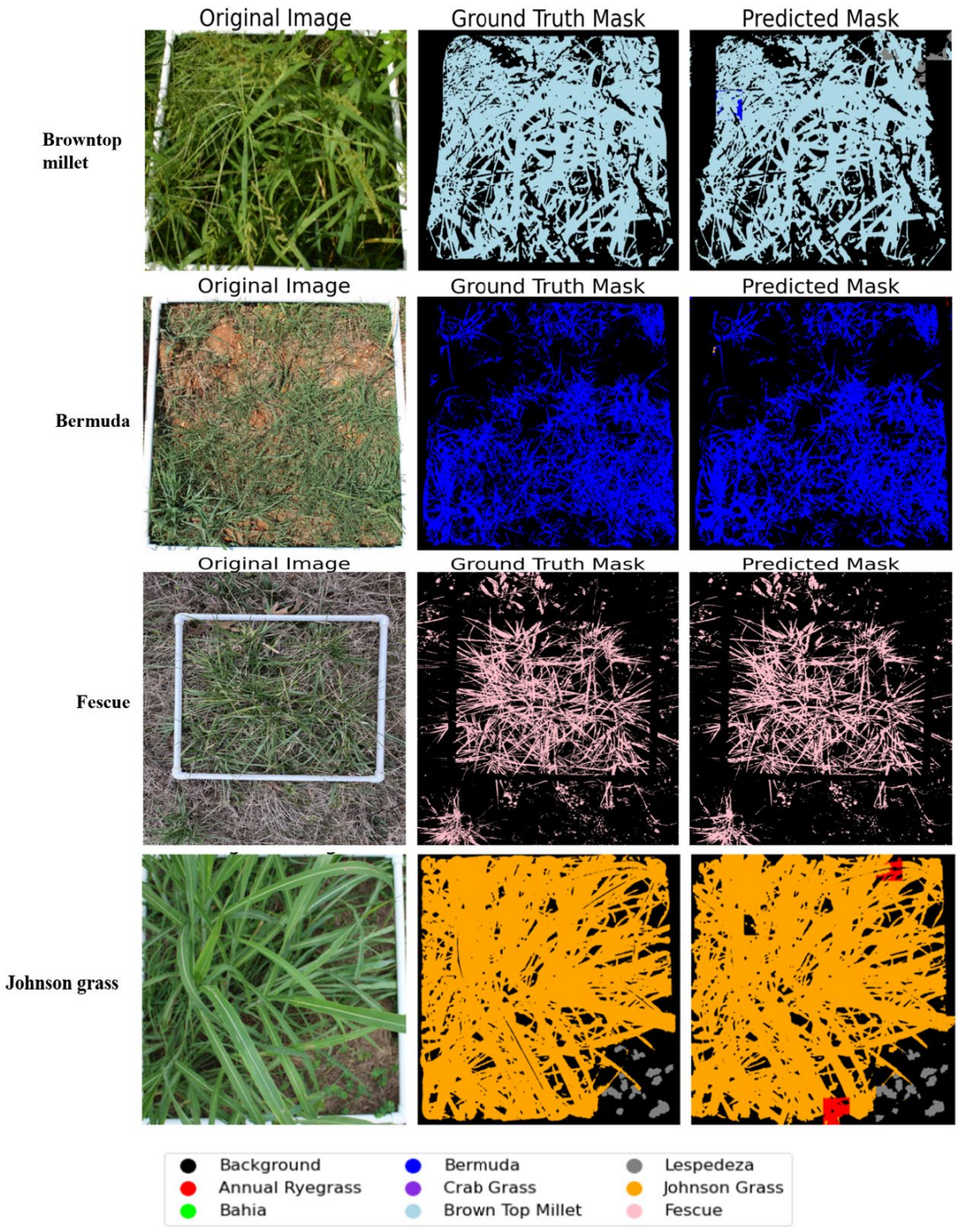

Figure A-5: Visualization of the deep learning model's performance in detecting various vegetation species along with legend showing colors used to display different vegetation species.

Additionally, the DL model encounters challenges in accurately detecting vegetation species in certain cases, particularly when there is a high similarity between different grass

species. The visualization results below illustrate instances where the model's performance is limited, highlighting areas of confusion between similar vegetation types.

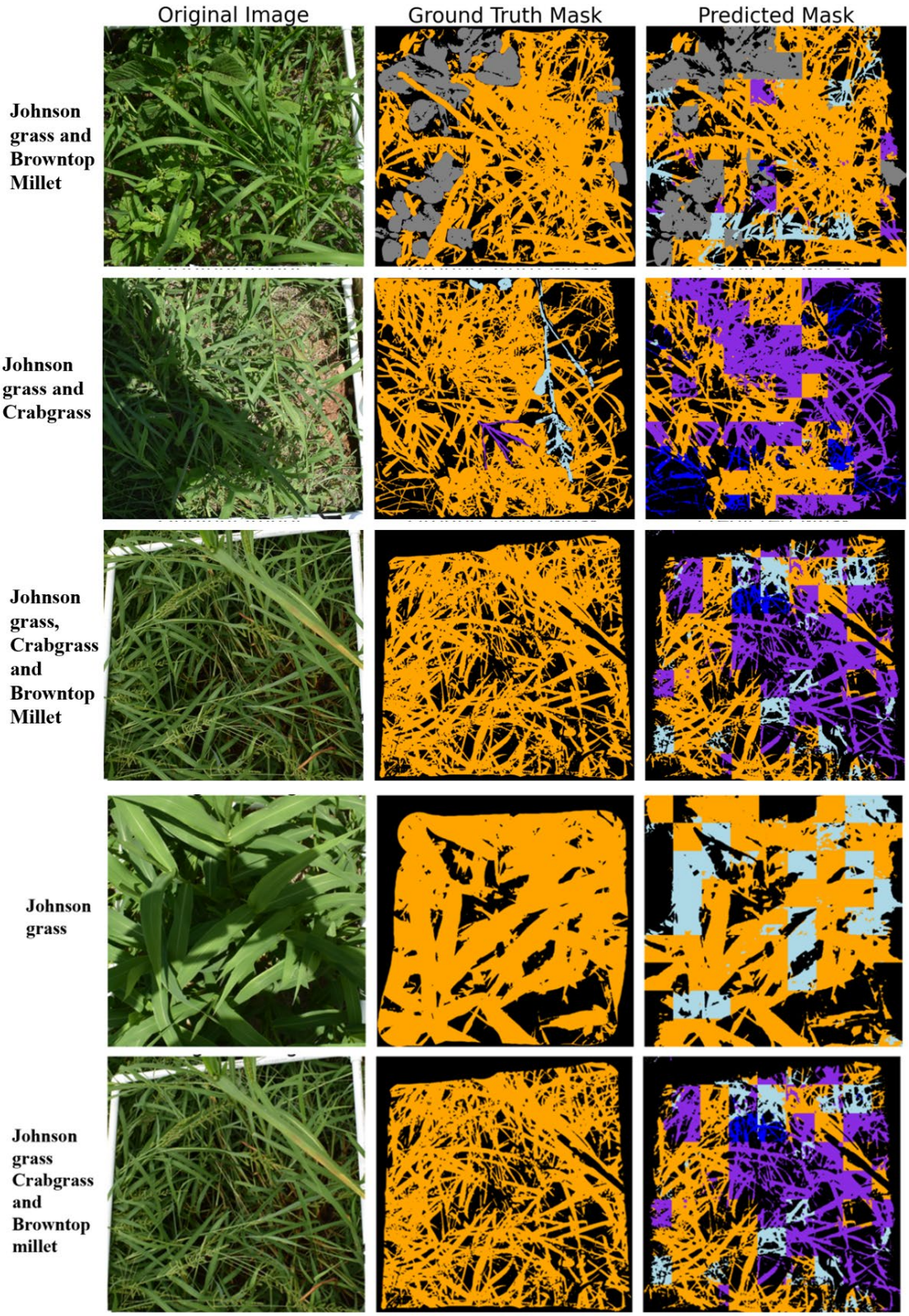

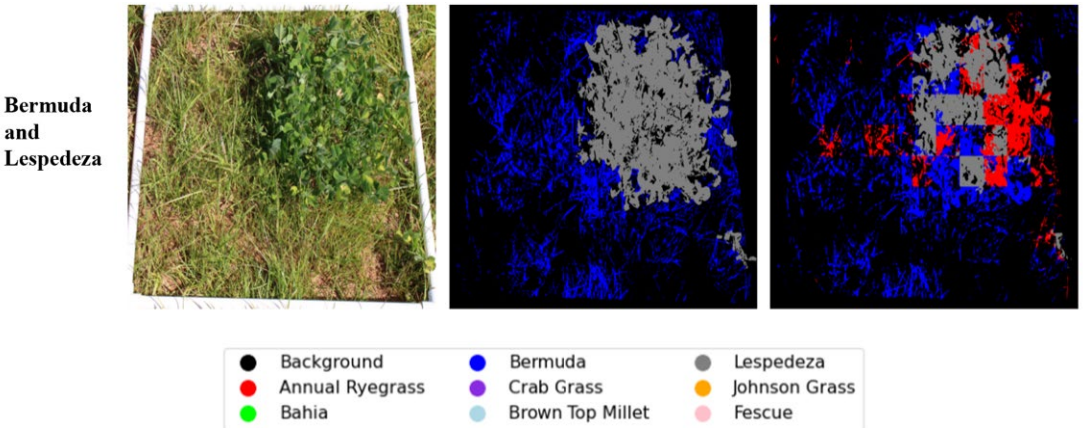

Figure A-6: Visualization of the deep learning model's performance in detecting various vegetation species along with legend showing colors used to display different vegetation species.

Figure A-7. outlines a workflow for analyzing vegetation at a construction site using multispectral remote sensing data collected by drones. The process begins with drone-mounted multispectral sensors capturing NIR, RedEdge, and Red images at the construction sites. These orthomosaic images were imported in the QGIS software to generate VI maps such as NDVI, NDRE, and SAVI. The resulting VI maps are further processed to create threshold maps that highlight areas with varying vegetation cover levels. This approach provides detailed spatial insights into vegetation characteristics, supporting effective monitoring and management of land clearing and site preparation during construction.

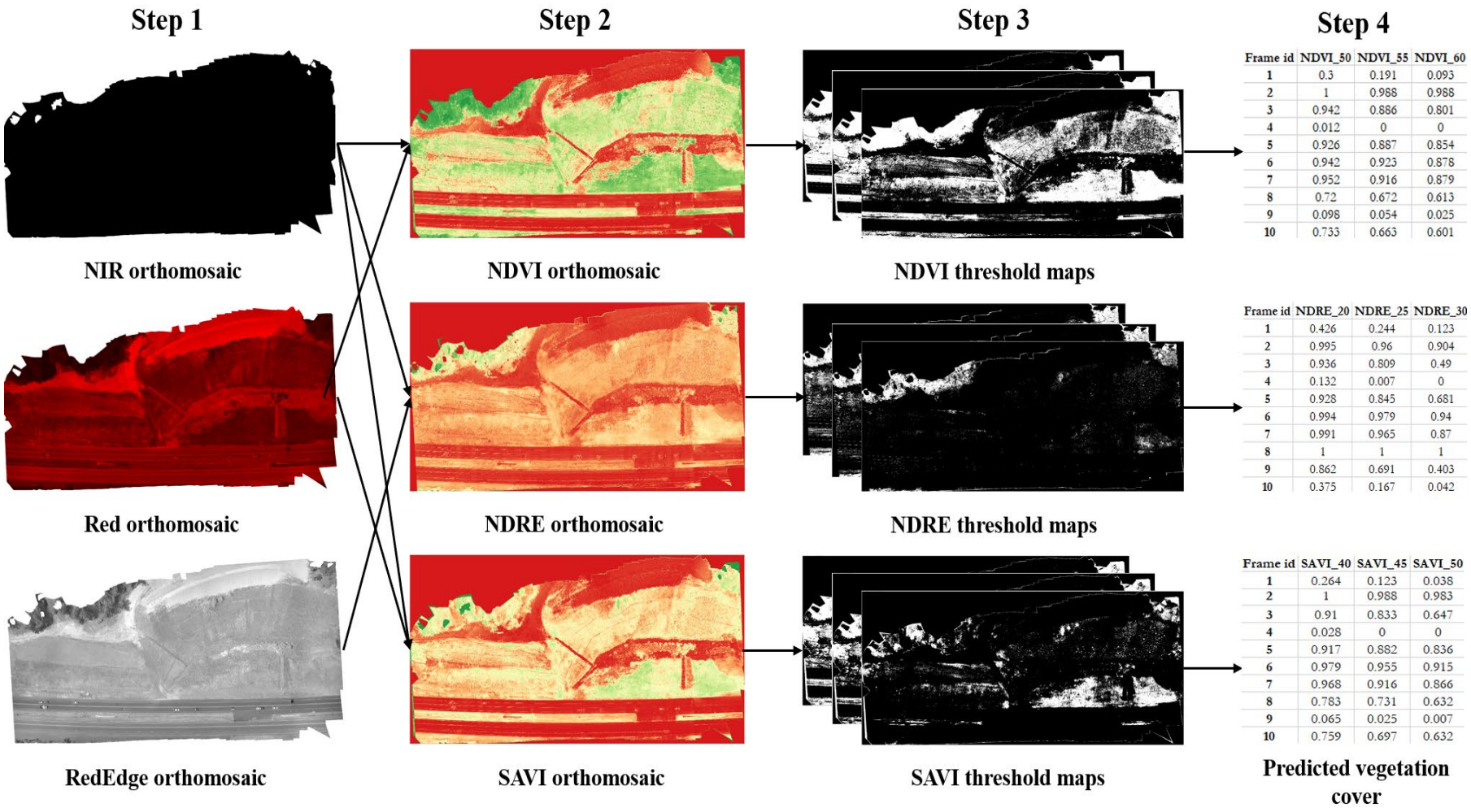

Frame id	NDVI_50	NDVI_55	NDVI_60
1	0.3	0.191	0.093
2	1	0.988	0.988
3	0.942	0.886	0.801
4	0.012	0	0
5	0.926	0.887	0.854
6	0.942	0.923	0.878
7	0.952	0.916	0.879
8	0.72	0.672	0.613
9	0.098	0.054	0.025
10	0.733	0.663	0.601

Frame id	NDRE_20	NDRE_25	NDRE_30
1	0.426	0.244	0.123
2	0.995	0.96	0.904
3	0.936	0.809	0.49
4	0.132	0.007	0
5	0.928	0.845	0.681
6	0.994	0.979	0.94
7	0.991	0.965	0.87
8	1	1	1
9	0.862	0.691	0.403
10	0.375	0.167	0.042

Frame id	SAVI_40	SAVI_45	SAVI_50
1	0.264	0.123	0.038
2	1	0.988	0.983
3	0.91	0.833	0.647
4	0.028	0	0
5	0.917	0.882	0.836
6	0.979	0.955	0.915
7	0.968	0.916	0.866
8	0.783	0.731	0.632
9	0.065	0.025	0.007
10	0.759	0.697	0.632

Figure A-7: Methods to process and generate Vegetation indices-based threshold maps in QGIS.